Density Functional Theory Studies of Solid Density Plasmas

Patrick Hollebon
Trinity College, Oxford
Supervised by Dr. Sam M Vinko & Prof. Justin S Wark

A thesis submitted for the degree of
Doctor of Philosophy

Trinity Term 2019

Abstract

In warm dense matter (WDM) and dense plasma physics, Density Functional Theory (DFT) has become a standard approach over the past many years for simulating transport properties, equations of state, interpreting experimental measurements and many other applications. The main chapters, two to four, of this thesis cover original work by the author on three topics: excited state pseudopotentials, time-dependent DFT (TDDFT) and many-body theory.

For an excited state pseudopotential, a specific excited ion core configuration is generated by externally imposing a set of occupation numbers in the same way as can be rigorously done for a non-interacting electron system. In chapter 2 results and a physical argument are presented seeking to justify this process when generating excited configurations of bound electron systems.

Those electrons that might be considered as 'free' within a plasma exhibit not only single-particle excitations, as one might label with a set of single-particle occupation numbers, but also significant collective behaviour i.e. plasmons. TDDFT linear-response theory is applied in chapter 3 as a rigorous means of modelling the general dynamic and wavelength-dependent response properties, and fluctuations, for quantum plasma systems. With help from the Langreth rules a fluctuation-dissipation relation for the electron dynamic structure factor is derived. Finally, the dynamic structure factor is computed for compressed Beryllium and CH plasma, with favourable comparison to experimental data and simulations by previous authors.

In chapter four the free-free opacity of solid density Al plasma is considered. Both the tensor nature of the dielectric function, in the form of local field corrections, and an accurate description of bound-state properties, in the form of correct binding energies, are required to reproduce experimental room temperature measurements. Commonly used exchange-correlation functionals are insufficient for predicting the energy gap between bound states and the continuum in a linear response theory context. To this end, the author has implemented and demonstrated finite-temperature many-body quasi-particle calculations in the Abinit code. These many-body calculations are expensive however they are a potential future source of accurate theoretical predictions, covering a wide range of plasma conditions to which other, perhaps simpler models might be benchmarked.

To my parents,

who taught me to never stop learning

Acknowledgements

Dans ses écrits, un sage Italien
Dit que le mieux est l'ennemi du bien.

– Voltaire, *La Bégueule*

Since starting this thesis I had hoped to have produced a suitably witty introduction worthy of the immense debt I owe to so many people for making this possible. Alas, after what I assure you has been a not-insignificant time frame, I feel somewhat humbled to be able to offer only my sincerest gratitude for all of the support that I have received from friends, family, colleagues, and teachers over these many years.

To start with I would like to thank my supervisors Justin Wark and Sam Vinko, without there teaching and guidance I would not have a fraction of the knowledge or understanding I have now. But perhaps more importantly, I am indebted to their enthusiasm and drive for the subject matter of this thesis, to which I inevitably owe more than a fair share of my own passion. Furthermore I am forever grateful to everyone in the Simon room, many of whom (well, mainly Ollie) have had to endure punishingly long periods of me talking about my own work over coffee.[1] Special thanks go to Thomas Preston, Orlando Ciricosta, Thomas White, Peter Norreys, David Lloyd, David McGonegle, Alex Savin, Gabriel Callejo, Quincy van den Berg and Alan Miscampbell for many long and fruitful conversations. Outside of Oxford, I am indebted to Mike Desjarlais for his expert advice on PAW potentials and time-dependent DFT, as well as informative discussions with Massimo Altarelli, Beata Ziaja, and the plasma physics group at the University of Rostock.

Legend has it that I also sometimes don't do physics. I owe a great deal to Robert Smith, Thomas Robertson, Ellie Farrell, VC, as well as everyone in the Trinity Tea group and all of my friends from Richard Huish College. So much of who I am today is the result of my wonderful parents, brother, and sister, without whom I am sure none of this would have been possible.

Finally, I would like to thank my fiancée Maura Valenti, whose generous and unwavering support at each step along the road has been truly the greatest gift.

[1] In retrospect, I think I'm glad I never really paid attention to how much coffee I've drunk over the years.

The author would like to thank the U.K. EPSRC for support under grant number EP/P015794/1. The author is also grateful to Trinity College, Oxford for additional financial support during the writing up stages of his DPhil.

Contents

1

Introduction

The content of this thesis represents a modest contribution to the study and simulation of dense plasmas for which quantum mechanical effects cannot be neglected. Specifically, this thesis focuses on the use of Density Functional Theory (DFT) as a means to solve the many-body Shrödinger equation in an *ab initio* manner within a consistent and clear set of approximations. DFT has been and continues to be, widely applied to the study of warm dense matter (WDM) and dense plasma physics. Within this thesis, I hope to have informed on what are perhaps some of the less well-known applications of DFT in this field, such as excited core pseudopotentials, time-dependent DFT (TDDFT) perturbation theory, and many-body theory quasi-particle calculations. Whilst each of these is accompanied by a rich and detailed body of literature, in this thesis, I hope to have provided some specific insight into their use and implementation in WDM and dense plasma conditions.

1.1 Warm dense matter and dense plasmas

Dense plasmas and WDM lie at the intersection of condensed matter and plasma physics, both of which bring with them their own approaches and

techniques for describing physical systems. Approaching solid density ($\sim$ 1 g cm^{-3}) several factors come into play that might otherwise be considered negligible in ideal plasma conditions. Fermionic exchange symmetry leads to Pauli repulsion between electrons, preventing matter from collapsing and providing the bulk spatial extent of the matter we experience every day [1]. Following on from the associated exchange symmetries of identical particles, thermodynamic quantities require either Fermi-Dirac or Bose-Einstein statistics, with the deviation of both from the classical canonical ensemble becoming more significant with increasing particle density and lower temperature.

Fundamentally we are dealing with a many-body problem of charged particles interacting via the Coulomb force. In plasma physics, we typically quantify the strength of these interactions in terms of the coupling parameter, defined as the ratio of potential to kinetic energy, for electron-electron, ion-electron, and ion-ion interactions. The exact value of particle-particle coupling is a complex function of density and temperature: reducing inter-particle separation increases the associated Coulomb interaction and collision rates, which must, in turn, compete with the ability of the plasma to screen charged particles. The eventual formation of correlated, bound, and quasi-bound groups of particles also reveal the quantised nature of energy eigenstates, such as the emergence of the familiar atomic shell structure, as well as phonons and bound-electron hole states in the condensed matter limit

At what point then that classical physics fails as a sufficient description of a plasma is a pertinent question, but one that is also best answered by considering instead the classical limit of the more accurate quantum theory. In the high-temperature limit, we expect particles to become asymptotically free, such that the discreet 'quanta' separating successive energy eigenvalues should become negligible. Furthermore, we might hope in the high-temperature limit that thermal statistical uncertainty vastly outweighs the uncertainty associ-

ated with a wavefunction - provided of course we have enough particles to make a thermal ensemble valid.

Density also plays a crucial role and it is in the low-density limit that classical, ideal plasma models are most often used. Of course, the reason this is acceptable is that we are able to 'renormalise' strong electron-nuclei correlations into quasi-particles - ions - with the remaining electron-electron and electron-ion coupling weak enough to warrant a classical treatment. With increased density, free electrons spend greater time in the vicinity of, or even within, the ion core such that a structureless, point-particle description of the latter becomes insufficient. The lifetime and energy of bound states within the ion are significantly affected by the presence of free electrons [2, 3], such that both free and bound states ought to be modelled in a self-consistent manner, complete with their dynamic interactions and a proper account of global exchange symmetry owing to *all* electrons in the plasma being indistinguishable.

What complicates dense plasmas and WDM compared to the high-density, condensed matter limit is the general need to deal with multiply excited states including both equilibrium (temperatures of up to tens of eV for WDM) and non-equilibrium conditions. We are thus left in the awkward position that we cannot rely entirely on the approximations of classical mechanics and weak coupling as might befit ideal plasmas, but neither can we limit ourselves to the study of the ground state and low lying excited states as encountered in condensed matter. Despite, or possibly because of, this challenge multiple theoretical techniques and approaches have of been developed and deployed to modelling this regime [4]. Together with increasing our understanding of WDM and dense plasma conditions, DFT calculations are valuable tools for informing approaches to higher temperature Hot Dense Matter (HDM) conditions in which one might hope there will some transition towards classical physics and/or other approximations associated with the decreasing coupling strength.

DFT is particularly advantageous in that it can be applied all the way down to the ground-state condensed matter level (for which it was initially derived [5,6]) and may, therefore, aid in providing a consistent understanding of matter from the ground state right through to HDM conditions.

With regards to their physical realisation on earth, the dense conditions studied in this thesis are most commonly encountered in high powered laser-plasma experiments. The latter being a central component of, to name just a few applications, the development of inertial confinement fusion (ICF) as a practical energy source [7–10]; the study of materials under extreme conditions [10–12]; and even replicating here on earth the astrophysical conditions encountered within stars and giant planets [13–17]. X-ray Free Electron Lasers (XFEL's) compliment high powered, optical laser systems, as a platform with which to study electronic processes in dense plasmas over femtosecond timescales such that solid density targets may be irradiated and probed isochorically before the target has time to expand [18–22]. The precision to which narrowband XFEL radiation may be tuned, together with spectroscopic measurements of line radiation, allow for a precise determination of ionisation energies, collision rates, absorption coefficients and charge state distributions under accurately known conditions of [solid] density. As such, they serve as an excellent tool for validating the fundamental predictions of quantum mechanical plasma models, such as those of DFT, under well characterised experimental conditions. Optical laser systems are often better suited for specific applications of dense plasmas [23–26]; however XFEL generated, isochorically heated, plasmas free of significant density or temperature gradients are essential for testing and constructing models before they are used to interpret data measured under conditions that are not a-prior known, or otherwise independently well constrained.

1.2 Density Functional Theory.

As stated earlier, from a fundamental - if slightly crass - point of view WDM and solid density plasmas are 'just' many-body Coulomb systems. With a little more attention to detail, we are specifically dealing with moderate to high coupling strength, though crucially this can vary significantly across distance scales and particle species, from the tightly bound electrons in the ion-core to the long distance ion-ion correlations in liquid metals and eventually phonons in the cold limit. Such systems are routinely dealt with in a quantum mechanical manner within condensed matter physics, albeit generally at much lower temperatures, and so it is natural to look in that direction for a quantum treatment of dense plasmas. DFT [5,6] is one of the most powerful and widely used techniques to solve the quantum mechanical many-body problem. As such, from its original formulation as a ground state theory DFT has developed into an important tool for providing numerical simulations of WDM and solid density plasma, both in terms of finite-temperature equilibrium properties [27] and excited states [28].

The central aim of DFT is to map the 3N dimensional problem of the quantum mechanical N-body system, to a functional minimisation problem in terms of the position dependent electron density. The Hohenberg-Kohn theorems [5], together with Mermin's finite temperature extension [27], establish the free-energy Ω, total energy E, kinetic energy T, electron interaction energy V_{ee}, and entropy S to all be universal functionals of the equilibrium density ρ alone.

$$\begin{aligned} \Omega\left[\rho(r)\right] &= E\left[\rho(r)\right] - \mathrm{T}S[\rho] \\ \Omega\left[\rho(r)\right] &= T[\rho] + V_{ee}[\rho] + \int d^3\mathbf{r}\ V_{ext}(\mathbf{r})\rho(\mathbf{r}) - \mathrm{T}S[\rho] \end{aligned} \tag{1.1}$$

Where an external potential V_{ext} couples to the electron density and the

temperature of the system is T (not to be confused with the kinetic energy $T[\rho]$). The equilibrium expectation value for the electron density $\rho(\mathbf{r})$ is then that which minimises the free-energy functional Ω. In turn, the external potential can be determined by knowledge of the temperature, density ρ, and universal functional forms. If we know the form of the bare electron-electron Coulomb interaction, this means the entire Hamiltonian, along with all properties of the system, can be expressed as a functional of ρ and the temperature T.

Having access to physically accurate expressions for the universal functionals would then effectively render the N-body problem moot, as minimising a functional subject to a 3-dimensional scalar field ρ is a computationally relatively straightforward problem. The search for ever more accurate expressions for these functionals continues [29–33], but for now, DFT calculations have been primarily performed using functionals derived from the properties of uniform, or almost so, electron systems. Meanwhile, whilst the calculation of general system properties can in principle be formulated in terms of the density, current-density and temperature [28], practical calculation of excited state properties using DFT is not without its own challenges, as will be explored in later chapters.

An alternative approach to directly minimising equation 1.1 is provided by the Kohn-Sham equations. First equation 1.1 is rearranged slightly to formulate the free energy in terms of the equivalent functionals for the non-interacting system, denoted by the subscript s :

$$\Omega\left[\rho(r)\right] = T_s[\rho] + V_{Hartree}[\rho] + \int d^3\mathbf{r}\ V_{ext}(\mathbf{r})\rho(\mathbf{r}) - \mathrm{T}S_s[\rho] + E_{xc}[\rho] \qquad (1.2)$$

Where the so called exchange-correlation term E_{xc} is simply defined as

the difference between the actual free-energy functional Ω and the functional corresponding to a system subject only to the mean-field, Hartree approximation to the Coulomb interaction. Expressing the electron density in terms of a set of wavefunctions ψ_n^{KS} and occupation numbers f_n, the Euler-Lagrange equations associated with minimising 1.2 become the Kohn-Sham equations:

$$\begin{gathered}\left[\frac{-\hbar^2}{2m_e}\nabla^2 + v_{eff}\right]\left|\psi_n^{KS}\right\rangle = \epsilon_n^{KS}\left|\psi_n^{KS}\right\rangle \\ \rho(\mathbf{r}) = \sum_n f_n(\epsilon_n - \mu)|\psi_n(\mathbf{r})|^2, \quad v_{eff} = v_{Hartree} + v_{ext} + \frac{\delta E_{xc}[\rho]}{\delta\rho(\mathbf{r})}\end{gathered} \tag{1.3}$$

Where f is the Fermi-Dirac distribution and μ is the chemical potential of the system. The exchange-correlation term now plays the role of an effective external potential determined by the equilibrium electron density ρ. The primary advantage of the Kohn-Sham approach is that the non-interacting components of the kinetic energy, T_s, and entropy S_s are treated exactly. We now need only find an approximate functional E_{xc} for the *difference* between the true free energy functional and that for a system within the Hartree approximation. The trade-off for the improved accuracy of the Kohn-Sham method is its increased computational time compared to directly minimising equation 1.1 using explicit functionals of the density - what is referred to as orbital-free DFT. The increased computational cost becomes ever apparent at higher temperatures with more and more orbitals being partly occupied by the tail of the Fermi-Dirac distribution. Orbital-free methods, therefore, remain of great use when studying very high temperature, or very large, systems [32, 34–38]. The DFT calculations performed and presented by the author in this thesis are all of the Kohn-Sham forms, thereby benefiting from the associated increase in accuracy yet keeping within practical time-frames through the use of parallelised code and application of high-performance supercomputing clusters.

It should be stressed that unlike the equilibrium density ρ and total free-energy Ω, the Kohn-Shan states ψ^{KS} and energies E^{KS} do not have a reliable physical interpretation beyond satisfying equations 1.3. DFT is, therefore, most readily applied to calculating properties with known expression in terms of the two former quantities, rather than those typically written in terms of the wavefunction itself of the system. Thermodynamic electronic properties such as pressure, heat capacity, and the forces on an ion within the Born-Oppenheimer approximation fall nicely within this category, whilst quantities such as electronic conductivity may require more careful treatment. Despite their questionable physical relevance, the Kohn-Sham orbitals do however provide a convenient basis set with which to calculate response functions - including the conductivity - as will be seen in later chapters.

1.3 The exchange-correlation term.

Ultimately any DFT calculation is limited by the available approximations to the free-energy functional. Within the Kohn-Sham method applied throughout this thesis, this amounts to finding expressions for the exchange-correlation term E_{xc}. Unfortunately, DFT itself does not provide any such expressions for E_{xc} and we must look to other methods, such as many-body theory, to guide us. Starting with the exchange interaction, which is without classical analogue, consider an electron at a point $\mathbf{r}$. We know that an electron does not experience a Coulomb interaction with itself, that is to say that even if there is an amplitude for the electron to be at some other point $\mathbf{r}'$ the there is no Coulomb interaction between points $\mathbf{r}$ and $\mathbf{r}'$. However, such a term is present in the Hartree interaction and must be subtracted off. Furthermore, for a system containing multiple electrons the requirement of anti-symmetry for the wavefunction leads to a Pauli repulsion 'force' between the electron at $\mathbf{r}$

and the remaining electrons in the system, essentially reducing the probability for another electron to be within a given distance from **r** and resulting in an exchange hole 'kicking out' the other electrons. The positions of the electrons are now correlated with each other. Note that whilst these correlations affect the Coulomb energy, they are not caused by the Coulomb interaction itself but are strictly a consequence of exchange symmetry.

In addition to exchange, the Coulomb interaction itself results in correlations between particles in much the same way as it does in classical mechanics. Whereas the Hartree term considers interactions only in terms of the mean electron density, clearly the repulsive force between two negative charges will affect the joint probability for two electrons to be separated by a given distance and thus affecting the overall Coulomb energy. The effect of correlations induced by the Coulomb interaction itself is, perhaps a little confusingly, referred to as the correlation energy contribution to the total energy.

Arguably the two most widely used approximations for the exchange-correlation term are the Local Density Approximation (LDA) [39] and the class of Generalised Gradient Approximations (GGA) [40]. The former is the result of applying point-wise in space an expression for the exchange-correlation energy of a uniform electron gas as a function of the local density. The class of GGA functionals are then calculated as corrections for small inhomogeneities and gradients in electron density. Whilst there exists an exact analytic expression for the exchange-energy of a uniform electron gas [41], the correlation energy contribution is typically taken from analytic fits to path integral Monte Carlo simulations or analytic expression for known limiting cases. Recent developments have been made towards generating and implementing temperature dependent exchange-correlation functionals to supplement the more commonly used zero temperature forms [32, 42–46]. However, the zero temperature exchange-correlation functionals have proven to be both

useful and accurate in predicting the properties of WDM and dense plasmas within the wider community. The exchange-correlation functionals used within this thesis will be in their zero temperature forms. However, in chapter four an alternative approach to treating exchange-correlation effects will be investigated which is both temperature dependent, as well as allows us to sidestep some of the wider difficulties with available exchange-correlation functionals.

1.4 Structure of the thesis

The remainder of this thesis is split into three main chapters. The following chapter will consist of relatively standard equilibrium DFT calculations, but with the additional feature that we will be using so-called excited state pseudopotentials. Whilst the Kohn-Sham equations 1.3 are without a doubt easier to solve than the Schrödinger equation itself, sophisticated numerical techniques are required for accurate and efficient computational schemes. Pseudopotentials are a key tool in this regard and in this thesis, we will investigate their ability to represent the interaction between an ion in an excited state and the surrounding plasma. The next chapter will also familiarise the reader with the general procedure for performing a DFT calculation.

In the third chapter, we will examine time-dependent DFT as a means to calculate electronic response properties in dense plasma environments. Linear response theory is used to calculate key plasma properties, such as the dielectric function, as well as time-dependent correlation functions for the unperturbed system via the fluctuation-dissipation theorem. The latter quantities are routinely measured in the course of X-ray Thomson scattering, a widespread experimental technique for diagnosing plasma conditions within WDM physics. The results of chapter three are compared to experimental data published by other groups obtained at the Linear accelerator Coherent

Light Source (LCLS) X-Fel and the National Ignition Facility (NIF), both in California.

A consequence of the method utilised in chapter three is the need to calculate all elements of the dielectric tensor - or rather up to given plane wave basis cutoff determined by the accuracy required. The majority of these elements are not directly measured via spectroscopy or X-ray Thomson scattering experiments. The content of chapter three then leads naturally onto the subject of chapter four; how the entire dielectric tensor can be used to generate predictions of response properties whilst correcting for the present limitations of time-dependent DFT using many-body theory. The chapter culminates by bringing together equilibrium DFT, time-dependent DFT, and many-body theory to calculate the opacity in solid density Aluminium from room temperature to WDM conditions.

The final chapter provides an overall summary of the work presented here and possible future research directions. The content of this thesis relative to current developments and research directions in the wider community of WDM and plasma physics is also discussed.

1.5 Contributions and publications of the author

The author is responsible for all DFT simulations presented in this thesis unless indicated otherwise, for which the author used the Abinit code [47]. Furthermore, the Projector Augmented Wave pseudopotentials used throughout this thesis during DFT simulations have all been custom generated by the author using the Atompaw package [48].

Selected results from chapter 4 have been converted into a paper and ac-

cepted for publication in Physical Review E, there is also a shortened pre-print currently uploaded to Arxiv. All changes to the Abinit source code necessary to perform the finite-temperature, many-body calculations of chapter 4 are the result of the author's own work. A more user-friendly version of this code is in the midst of preparation and may be submitted for proposed inclusion within the overall Abinit project in the near future. The contents of chapter 2 have also been written up by the author and submitted to Physical Review E, though it was rejected on the basis of insufficient impact. A modified version of that manuscript is currently being drafted for re-submission to a different journal.

In addition to the theoretical results presented in this thesis, the author was also responsible for calculations required to determine spectrometer alignment as well as general data collection duties during an LCLS experiment in April 2014. Results from this experiment have been published twice in Physical Review Letters [22, 49], both of for which the author of this thesis is listed as a co-author. Unpublished experimental work by the author includes opacity measurements taken at both the DESY FLASH facility located in Hamburg, Germany during March of 2014 as well as measurements taken using the Elettra-Sincrotrone Trieste FERMI laser facility near Trieste, Italy during May of 2015. In both cases, the author was involved in the experimental setup, alignment, and data collection, along with the additional responsibility of programming of motorised stages for use within the FLASH vacuum chamber.

Finally, the content of this thesis has been variously presented by the author in both posters and slide formats at numerous conferences and seminars. These include the American Physical Society (APS) Plasma Physics Meeting as well as at user meetings for the Central Laser Facility, National Ignition Facility and European X-FEL facility. Additionally, the author presented select results

from chapter 4 in seminars taking place at the University of Rostock, Germany and at the Center for Free-Electron Science located in Hamburg, Germany.

2

Excited Core Pseudopotentials

2.1 Introduction

DFT offers a powerful, and in principle exact, means of solving the quantum-mechanical many-body problem in the presence of an external potential. For atoms, molecules, condensed matter, and plasma this external potential will inevitably include those of charged nuclei and/or ions. It is a physically intuitive and computationally helpful picture if we can separate the motion of electrons bound to ions from those that make up the surrounding electron gas that permeates both plasmas and metal, and if within at least some approximation we might reduce the impact of their mutual interaction to that of static external potentials when dealing separately with the two systems. The natural question is then: under what circumstances, and with what means, can we make these approximations?

For this thesis, the first approximation we will take is to model the nuclei as classical particles with well-defined position and momentum.[1] On the other

[1]This, I distinguish from the Born-Oppenheimer approximation in which electrons are assumed to equilibrate, and correlations in electron density fluctuations to decay, over timescales much shorter than the ionic motion. A complete description of the dynamic motion of ions in a heated electron system does require modelling beyond the Born-Oppenheimer approximation such that correlations in electron density fluctuations might persist during the motion of, and therefore may do work upon, nuclei/ions such that the

hand quantum mechanics will be essential in describing the interaction between the combined electron + nucleus system that is an ion, and the surrounding medium. For example, Pauli repulsion prohibits surrounding electrons (valence) from occupying the same Hilbert space as bound electrons incorporated into the ion potential (core electrons), a strictly quantum effect that cannot be exactly replicated with any local potential. In addition, bound electrons, in general, respond to changes in physical surroundings, and so an accurate modelling of the quantised nature of atomic orbitals is needed if we are to justify any single ion pseudopotential as one that is accurate across multiple chemical environments.

Calculations without pseudopotentials are generally more computationally costly than those with them [52]. For one, incorporating tightly bound electrons into the pseudopotential core removes them from simulations of bulk systems containing multiple ions, thus reducing the number of states that need to be calculated. Furthermore, well-constructed pseudopotentials ought to reduce the computational cost for codes using plane-wave basis sets to represent Kohn-Sham wavefunctions in the vicinity of the ion core. In the latter region, single-electron wavefunctions exhibit short-wavelength spatial oscillations, known as Friedel oscillations, arising from the requirements of wavefunction orthogonality in the presence of a high density of localised bound states, and as a result require a higher number of plane waves to represent. To deal

latter are heated up. Conversely, energy exchange in the opposite direction requires electrons to evolve non-adiabatically under a time-dependent potential arising from moving ions. The consequences for nuclei and ion motion beyond the Born-Oppenheimer approximation has been studied phenomenologically via Langevin DFT-MD simulations [50], whilst the associated time evolution of an evolving electron system might in principle be examined using real-time TDDFT [51] in conjunction with Ehrenfest molecular dynamics. For the majority of this thesis, the Born-Oppenheimer approximation will be taken as we will be only interested in obtaining the static, equilibrium, nuclei/ion configurations rather than studying the dynamic coupling between electrons and nuclei. An exception to this will be during chapter 3 where I draw attention to the power of TDDFT linear response theory to calculate the full tensor response properties of a plasma, and how this might in future be applied to understanding dynamic electron-nuclei coupling.

with this computational hurdle, pseudopotentials are typically constructed to produce artificial, 'soft' (i.e. requiring fewer plane waves to represent) valence wavefunctions close to the nuclei, whilst still reproducing the scattering properties of the true ion system at large distances. Such potentials do not reproduce exactly the results of a true all-electron calculation and instead rely on the properties of interest being primarily sensitive to valence electron behaviour outside the core region where, for example, chemical bonds are formed.

With the content of this section in mind, the accuracy of a given pseudopotential can be queried on two fronts:

(1) How well does the pseudopotential reproduce the combined effects of wavefunction orthogonality plus Coulomb interaction between core and valence electrons in the isolated atom?

(2) To what extent can we assume the core electrons, and thus the pseudopotential, to be unaffected by changes in the physical and chemical environment?

This latter point is referred to as the frozen-core approximation and will be discussed at length in this chapter.

2.2 Projector Augmented Wave Potentials

The Projector Augmented Wave (PAW) pseudopotentials [53] used throughout this thesis have the unique advantage that, if constructed correctly, the correct scattering properties of valence electrons (in the sense of resembling those obtained using an all-electron, non-pseudopotential calculation) can be recovered at any distance from the nucleus. Rather than replacing the true interaction with a 'soft' scattering pseudopotential, PAW potentials instead map

the Kohn-Sham wavefunctions onto smooth pseudised functions $|\tilde{\Phi}\rangle_n$ with a transformation of basis T:

$$\begin{aligned} |\Phi_n\rangle &= T \left|\tilde{\Phi}_n\right\rangle \\ &= \left[1 + \sum_R \hat{T}_R\right] \left|\tilde{\Phi}_n\right\rangle . \end{aligned}$$

This transformation differs from the identity only within a PAW sphere of radius r_c centred on each ion position R. The ion-centred transformations $\hat{T}_R$ are expressed in terms of; a smooth basis set within the PAW sphere $\tilde{\phi}_i$, projector functions $\tilde{p}_i$, and the target atomic wavefunctions ϕ_i that we wish to soften or 'pseudise':

$$|\Phi_n\rangle = \left|\tilde{\Phi}_n\right\rangle + \sum_R \sum_i (\phi_i^R - \tilde{\phi}_i^R) \left\langle \tilde{p}_i^R \middle| \tilde{\Phi}_n \right\rangle \tag{2.1}$$

Provided both $\tilde{\phi}_i$ and ϕ_i individually form complete sets, this basis transformation can then be inverted to reveal the true, rapidly varying Friedel oscillations of the Kohn-Sham states close to the core. A PAW potential achieves its computational gain primarily through this basis transformation, as such one can in principle avoid the frozen core approximation altogether and create all-valence PAW potentials not present in other pseudopotential schemes. The effect of pseudisation on the 3s wavefunction in ground-state Al is shown as an example in Fig. 2.1 together with the corresponding projector function. Observe that the pseudised function contains one less turning point than the true atomic state.

The main DFT calculation, or bulk simulation, then acts to solve the Kohn-Sham equation in this new basis:

$$T^\dagger H_{KS} T \left|\tilde{\Phi}_n\right\rangle = E_{KS} T^\dagger T \left|\tilde{\Phi}_n\right\rangle \tag{2.2}$$

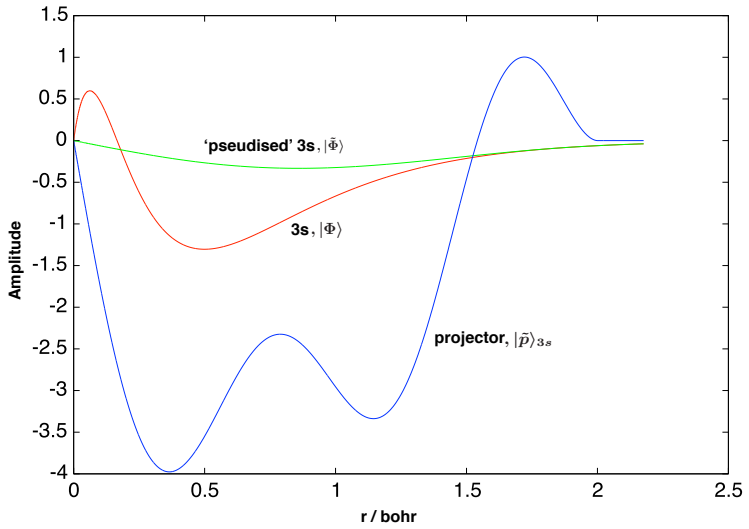

Figure 2.1: Comparison of 3s state and its pseudised equivalent for a ground-state Al atom. Note that for numerical stability it is best to keep both wavefunctions and projector functions to the same order of magnitude.

Note that the operator T is not required to be unitary. With a suitable T, the resulting pseudised wavefunctions in the bulk calculation should require fewer plane-waves to represent. In order to accelerate the convergence in representing $\tilde{\Phi}_n$ with a finite size basis set (as is unavoidable in any real computation), the target wavefunctions ϕ_i are typically bound and scattering eigenstates of the isolated atomic system, though other choices of targets are of course permitted. The standard choice stems from the zeroth order prediction that the bulk Kohn-Sham states Φ_n can, at least for the tightly bound states, be approximated by superimposing the atomic wavefunctions about each ion in the bulk. However, when designing a new PAW potential the number and nature of the target wavefunctions used should be converged and validated respectively through reproducing key bulk properties such as crystal structures and lattice spacing.

Testing the completeness of a PAW transformation and its impact on electron behaviour outside of the transformation sphere can be quickly done at the isolated atom/ion stage through examining the logarithmic derivatives of

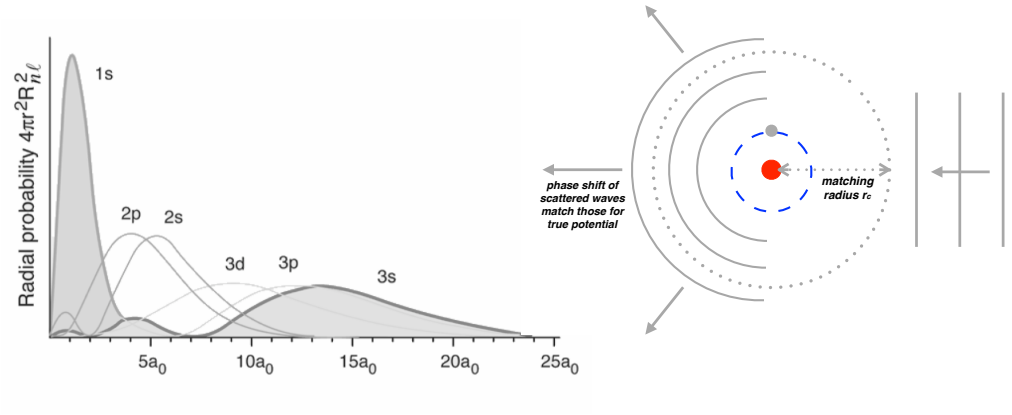

Figure 2.2: Atomic bound states such as those of Hydrogen (left) exhibit rapid spatial oscillations known as Friedel oscillations in the vicinity of the potential minimum centred at the nucleus. Pseudopotentials produce smoother wavefunctions within a certain radius r_c. A standard check that $r > r_c$ is essentially unchanged is to compare scattering phase shifts at $r = r_c$ for incoming and outgoing states (right), thus determining the boundary conditions for the $r > r_c$ space.

bound and scattering states. Consider plane waves of wavevector k incident on an isolated atom as shown in Fig. 2.2. Taking advantage of the spherical symmetry of the scattering potential we can reduce the isolated ion/atom problem to solving the radial Kohn-Sham Shrödinger equation:

$$\frac{d^2 R_l}{dr^2} + \frac{2}{r}\frac{R_l}{r} + \left[k^2 - V_{KS}(r) - \frac{l(l+1)}{r^2}\right] R_l = 0. \tag{2.3}$$

Where the Kohn-Sham solutions are then expressible in terms of the spherical harmonics:

$$\psi_{KS}(r, \theta, \phi) = R_l(r) Y_{lm}(\theta, \phi). \tag{2.4}$$

Following from the fact that the PAW transformation T differs from the identity only within the PAW spheres surrounding each nuclei, the scattered wavefunction of both the actual Kohn-Sham atom system and its PAW transformed

equivalent ought to be identical for $r > r_C$ as illustrated in Fig. 2.2. To check this we can perform a partial wave analysis of the outgoing states in Fig. 2.2, decomposing them into their angular momentum components and comparing the radial solutions R_l obtained from both Eqn. 2.3 and the equivalent PAW transformed Hamiltonian, Eqn. 2.2. By construction the Kohn-Sham potential is left unchanged for $r > r_C$, we therefore need only check for identical boundary conditions at $r = r_C$ (the boundary conditions at infinity remain identical) through comparison of the logarithmic derivatives:

$$\left.\frac{d\,\ln R_l}{dr}\right|_{r_C} = \left.\frac{1}{R_l}\frac{dR_l}{dr}\right|_{r_C}. \tag{2.5}$$

Plots of the logarithmic derivatives as a function of the incoming plane wave kinetic energy $E = \frac{k^2}{2m}$ are shown in Fig. 2.3 for different angular momentum l. A failure of logarithmic derivatives to match is generally indicative that the PAW transformation is incomplete, or possibly numerically unstable. On the other hand, an agreement does not on its own guarantee the potential is accurate.

To enforce core-valence orthogonality we need only remove the core wavefunctions from the space spanned by the PAW transformation T, removing them from the space of solutions to the bulk Hamiltonian of Eqn. 2.2. Together with our use of a Fermi-Dirac occupation distribution, this allows for an accurate treatment of Pauli repulsion effects responsible for preventing electrons from crashing into the nuclei and, ultimately, the spatial extent and structure of matter. That said, this in no way guarantees we have a complete description of the effects of many-body exchange-symmetry, much of which has been moved into the exchange-correlation functional. During the bulk calculation, exchange-correlation should in principle be a functional of the combined core-plus-valence electron density. The associated core charge con-

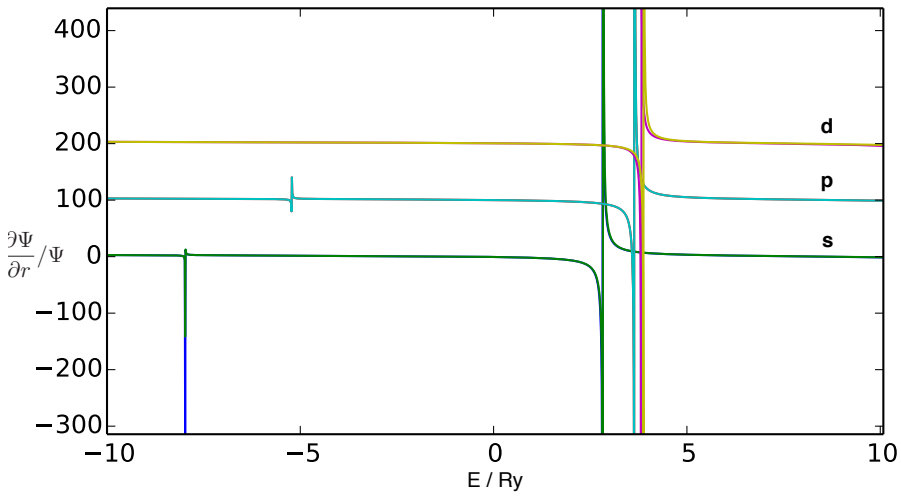

Figure 2.3: Example comparison of the radial logarithmic derivatives (see Eqn. 2.5) for a ground state Al atom. Scattering from the all-electron potential and PAW transformed equivalent are superimposed for incoming/outgoing Bessel functions of angular momentum $l = 0, 1, 2$, note that the two are essentially indistinguishable. The x-axis indicates the energy in atomic units of each Bessel function in the limit of $r \to \infty$ (negative energies indicate asymptotically bound Bessel functions).

tribution to the non-linear exchange-correlation functional is, however, often neglected and did not have a significant effect on the results presented in this thesis. Orthogonality, for the most part, kicks out the valence electrons from the tightly bound core, restricting the role of local and semi-local expressions for the exchange-correlation functional in that region. Of greater influence, after the accurate and stable numerical generation of the PAW transformation, is the extent to which the frozen core approximation holds and can be relied on in differing chemical environments.

2.3 Excited core potentials

The core of an ion may be placed into an excited configuration state by enforcing a vacancy for one of the core state occupation numbers and either removing the electron from the system entirely or placing it in an outer valence state to

preserve the overall charge. Pseudopotentials that describe the interaction of excited cores with their surroundings are particularly useful for performing so-called delta self-consistent field (Δscf) calculations of an ion embedded within an infinite periodic system. The Δscf approach requires two DFT calculations, one in which some number of the Kohn-Sham orbitals have been forced to be unoccupied, and another under equilibrium conditions. The difference in total energy between the two is then taken as an approximation for the ionisation, or excitation energy, of the equilibrium system. The nature of the Kohn-Sham orbitals leaves imposing arbitrary, non-thermal occupation numbers as without a clear physical meaning. Nonetheless, for finite size systems at least, the Δscf approach has proven to be useful in predicting the excitation spectra of molecules, clusters and mesoscopic systems. A discussion of the reasons why it works under these conditions is provided by Onida [54], with emphasis placed on the similarity between Kohn-Sham states and more 'physical' single particle wavefunctions as might be obtained from a quasiparticle calculation (see Chapter 4). Furthermore, Onida argues that the response to the sudden presence of an electron-hole in a finite system can, for the most part, be described by the Hartree term alone. The questionable use of what is almost always an equilibrium exchange-correlation functional during the excited configuration DFT calculation is thus of relatively small consequence.

Unlike a finite system, our ions will be embedded within and interacting with, an extended effectively infinite plasma environment. Nonetheless, for deeply bound core electrons we might reasonably expect a physically meaningful set of single-particle wavefunctions to be well localised and forming a finite size system. Unfortunately Kohn-Sham states in a periodic system will always form extended Bloch states as the Kohn-Sham potential, by virtue of it being a density functional, will exhibit the same symmetries as the density

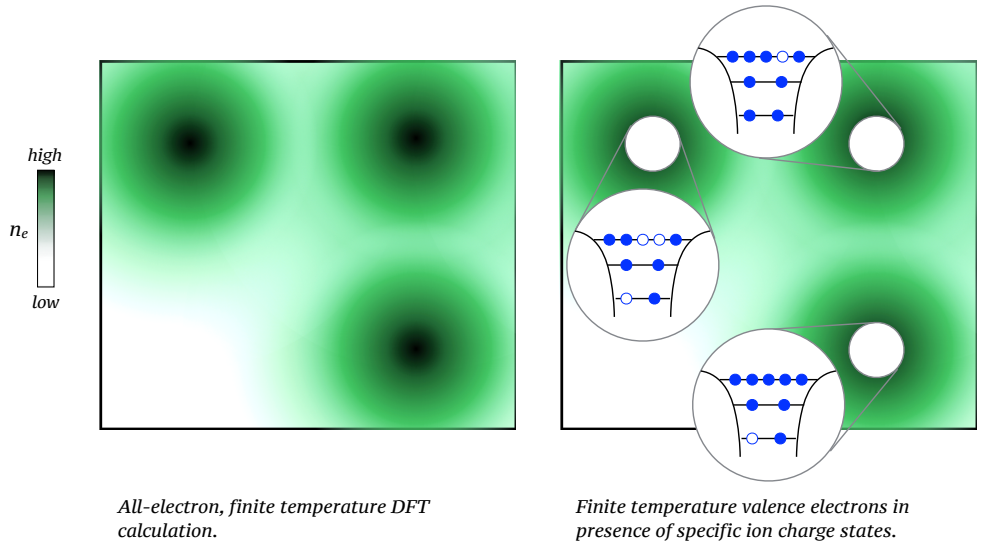

Figure 2.4: Cartoon of the equilibrium electron density from a DFT calculation for 3 nuclei (left). In reality, the physical system is in one of the many possible electronic configurations that compose the thermal ensemble. Excited core pseudopotentials allow for individual ion charge configurations to be considered, whilst the valence electron density remains a thermal average quantity (right).

itself.[2] The Kohn-Sham alone, therefore, do not demonstrate the transition to localised single electron orbitals as featured in a Mott-Hubbard transition. In the interest of describing realistic excited state densities, it is then arguably more meaningful to replace low lying core electron states in an all-electron DFT calculation with ion centred, frozen core wavefunctions from an isolated atom calculation. In this manner, one can impose separate, excited state configurations for each individual ions, for example, to model the ionisation process within the Δscf approximation as a process that involves a single ion rather than the partial ionisation of all ions in the plasma.

It is not readily apparent whether a physically meaningful pseudopoten-

[2]This may sound a little strange seeing as the Hohenberg-Kohn theorems demonstrate that the density determines the external potentials which, together with knowledge of the bare electron-electron interaction term, determines all properties of the system including single-particle wavefunctions. The rationale is that any physical measurement described using correlation functions must still be gauge invariant following a shift of spatial coordinates by a lattice vector. Therefore the Hohenberg-Kohn [Mermin] functional, along with its functional derivatives, remains sufficient for describing any physical measurement

tial can actually be constructed to describe the interaction between the surrounding plasma and a *specific* ion charge configuration. All-electron DFT calculations provide a thermal, mean electron density (Fig. 2.4, left), for what is in actuality a thermal ensemble including a number of different ion charge states (Fig. 2.4, right). Both the Δscf calculations and the study of plasma properties beyond mean ionisation models require calculations of the type shown on the right in Fig. 2.4. What would then be convenient, and also in line with the frequent neglect of non-linear exchange-correlation corrections, would be to show that the interaction between core and valence electrons can be adequately described by the Hartree interaction (plus the requirement of wavefunction orthogonality) alone. If this is the case, it lends credibility to modelling a plasma in the presence of arbitrary ion charge states using excited core potentials without having to worry about the complicated problem of modelling exchange and correlation contributions to the interaction between a finite temperature, equilibrium sea of valence electrons and the individual, non-thermal average charge state ions.

From a many-body theory perspective (discussed more in chapter 4) we can qualitatively, if not quantitatively, consider the importance of beyond Hartree mean-field corrections to the interaction between core and valence electrons. We can characterise density fluctuations and response times of the core electrons using the Bohr frequencies corresponding to inner shell transitions, and use the plasma frequency to characterise the response of the surrounding plasma. For tightly bound electrons, we might expect any oscillations between core states that results in significant polarisation to occur within timescales much shorter than the time taken for the surrounding plasma to respond. Bound states, on the other hand, will respond quickly, becoming polarised by the motion of free electrons. For low lying states in the continuum the single-electron wavelength extends across multiple unit cells, and on such length

scales bound state polarisation is screened out by free electrons collectively responding at the plasma frequency. Thus, the impact of the bound state response on the behaviour of free electrons at low energy or momentum k might be expected to be small on time timescales greater than a plasma oscillation $\frac{1}{\omega_p(k)}$. The above suggests there is a tentative physical argument to be made, under the appropriate conditions, for neglecting the response of free electrons to the motion of bound electrons and vice versa, allowing us to deal with their interaction at the mean field Hartree level alone. Such an approximation might be valid but is extremely difficult to justify without directly evaluating the many-body interaction between core and valence electrons. Unlike the Coulomb correlation energy contribution, the bound-free exchange energy is dependent only on the spatial overlap between bound and free states. Given the effect of core-valence orthogonality to effectively expel free electron states from the ion core, i.e. the Pauli exclusion principle, one might reasonably expect that in some limit of there being a clear distinction between 'bound' and 'free' electrons the core-valence exchange contribution should also vanish.

2.4 Testing and validating an excited core PAW potential

Putting aside the exact physical interpretation of excited core pseudopotentials for now, a key question to ask ourselves is what calculations or tests are available to convince ourselves we have generated one correctly and is it satisfying the two questions presented in the introduction to this chapter? The remainder of this chapter will be focused on addressing this, as demonstrated for the example case of core-excited Na in solid density conditions. We choose Na due to its low Z number permitting computationally cheap, all-electron

DFT calculations (to follow) whilst still possessing tightly bound core K and L shells at solid density.

The choice of the PAW potential scheme formally addresses the first question provided that the basis set ϕ_i^R is complete, other than the usual exclusion of core wavefunctions. Practically speaking a sufficient size of basis set required depends on the physical quantity of interest, e.g. *GW* calculations require typically at least 2 basis functions per angular momentum in addition to the occupied valence states. The frozen-core assumption, however, requires additional consideration for excited core pseudopotentials compared to the those for the ground state. Specifically, the latter possess a certain advantage that becomes apparent when we consider the surrounding plasma as a perturbation acting on the isolated atom core states: perturbations that mix two different states of equal occupation number do not actually change the total electron density. This cancellation of the effects of the surroundings does, however, not hold for general, excited state configurations. Compared to the ground state, relaxing the core in excited configurations may have a greater effect on valence behaviour as not only are the core wavefunctions altered but any mixing between states of unequal occupation will affect the core density too and in turn, the Coulomb potential experienced by valence states.

Standard PAW potential construction procedures in the generation of excited core potentials; checking scattering properties via logarithmic derivatives, and ensuring both wavefunction and projector functions are numerically sensible. Atompaw [48] is used here and throughout this thesis to generate PAW potentials, the first step for which is to perform an all-electron DFT calculation of the isolated Na atom. The Kohn-Sham wavefunctions of the ground-state isolated, atom are plotted in Fig. 2.5 together with those from a Hartree-Fock calculation using R.D. Cowan's code [55]. Their mutual similarity and recognisably atomic features reflect the previously mentioned point that the

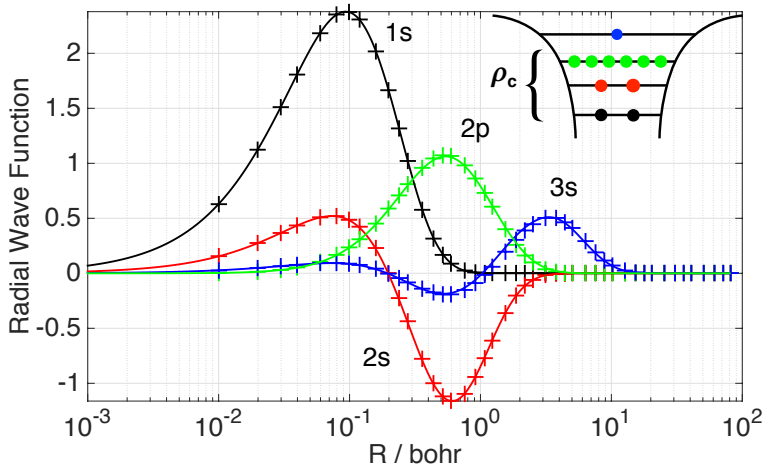

Figure 2.5: Comparison of Kohn-Sham wavefunctions (crosses, +) and Hartree-Fock equivalents (solid line, -) for an isolated ground state Na atom. Whilst it is difficult to assign a clear physical meaning to the Kohn-Sham states in many cases; such as for this finite size, isolated-atom system; they do closely resemble individual particle wavefunctions obtained from other techniques such as Hartree-Fock.

Kohn-Sham orbitals closely resemble single particle wavefunctions found using other approaches, such as Hartree-Fock, in which they hold a clear physical meaning.

The all-electron PAW potential is then used to compute the electronic structure for bcc, solid density Na at electron temperatures corresponding to an integer number of electrons thermally ionised out of the L-shell. Fig. 2.6 shows the corresponding temperatures and number of L-shell holes up to a total ionisation degree of +5 (recall that solid density, bcc Na has a ground state ionisation of +1).

Excited state frozen core PAW potentials are then generated in a near identical manner to the ground state, but with the additional imposition of excited state (i.e., partially filled) occupation numbers in the L-shell. Charge neutrality is preserved by placing an appropriate amount of electrons in the higher

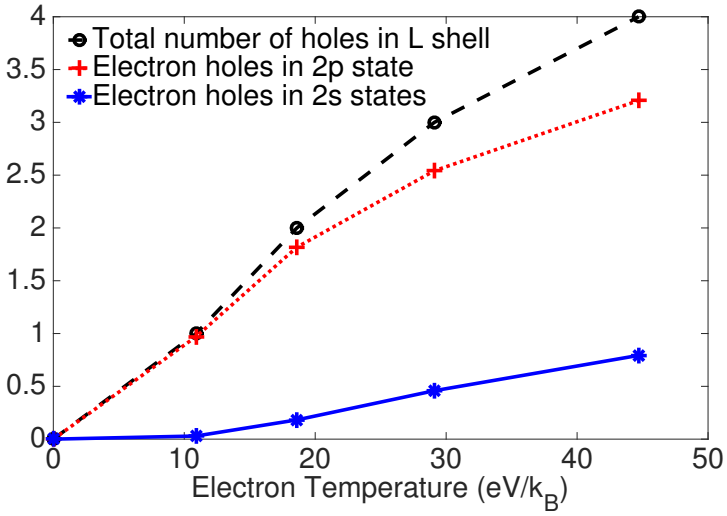

Figure 2.6: Plot of electron temperature versus number of L-shell holes for the all-electron calculation, used to determine the number of core holes to be imposed in the frozen-core calculation.

Kohn-Sham orbitals, the occupation numbers of which are free to vary to obtain the lowest ground state energy given the excited core configuration. Fig. 2.7 shows the isolated-atom single-particle states from both Kohn-Sham and Hartree-Fock calculations for the highest excited state of Na considered. Both approaches show near identical radial contraction of the atomic wavefunctions.

Once the excited state, frozen core potentials have been generated, bulk bcc Na calculations are performed and the resulting density of states compared with the equivalent all-electron calculation. Both frozen-core and all-electron calculations are performed at consistent electron temperatures. Fig. 2.8 illustrates the near identical frozen-core and all-electron calculations in the ground state. The excellent agreement remains as higher temperatures and ionisation states are considered in Fig. 2.9.

Angular momentum decomposition +3 and +4 core ionised Sodium is provided in Fig. 2.10 and 2.10 respectively. The tetrahedron method used to generate these produces noticeably more spikes in the density of states. Nonetheless one can clearly see how states with angular momentum quantum numbers

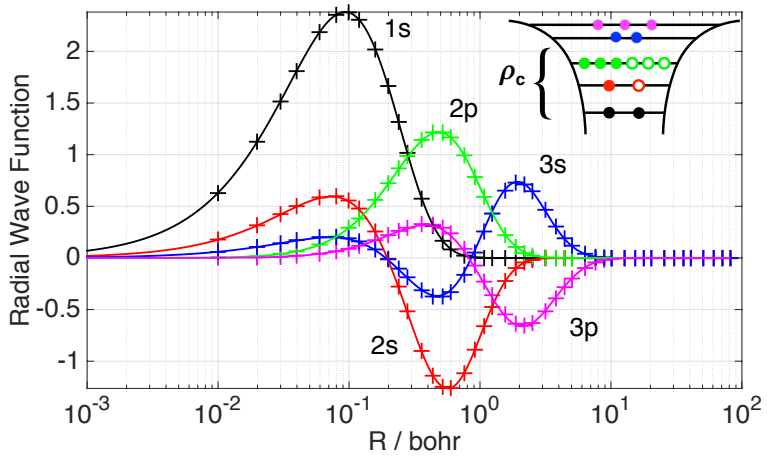

Figure 2.7: Same as Fig. 2.5 but for an excited configuration (shown in the inset). The radial contraction compared to Fig. 2.5 is reproduced by both Kohn-Sham (crosses, +) and Hartree-Fock states (solid lines, -).

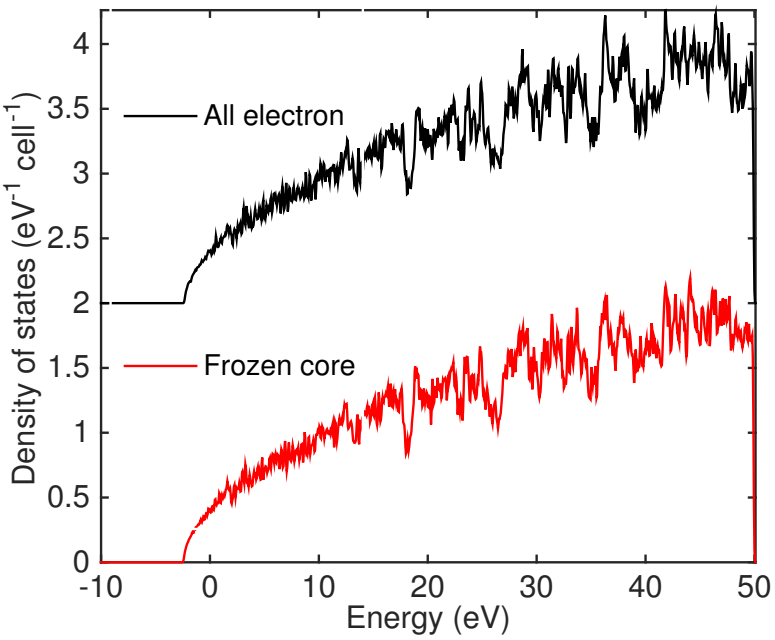

Figure 2.8: Ground state density of states calculation for bulk bcc Na. Both all-electron and frozen-core pseudopotentials produce almost identical results.

L=0, 1 and 2 form separate, broad atomic like peaks. Thus supporting the consistency of frozen core PAW potentials with all-electron calculations in

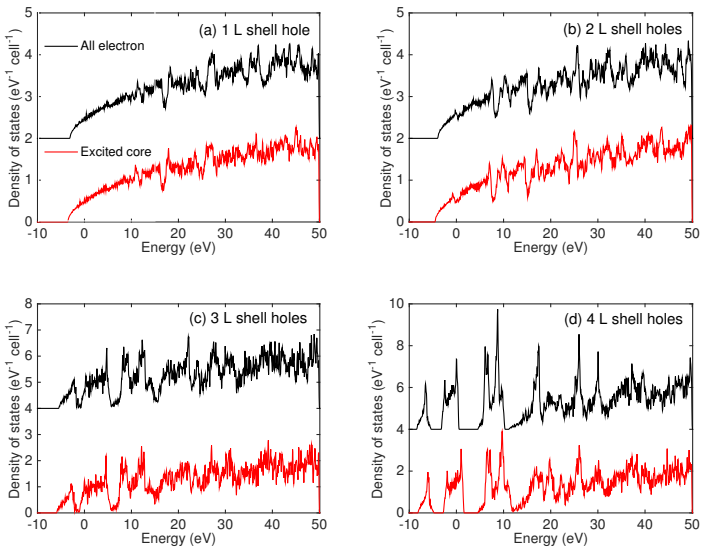

Figure 2.9: Density of states for a finite-temperature, ionised bcc Na crystal. The temperature chosen corresponds to integer numbers of electrons thermally ionised from the 5 lowest lying Kohn-Sham orbitals that compose the K and L shells in the all-electron calculation. Both frozen-core and all-electron pseudopotentials continue to give consistent density of states predictions.

predicting these structures, previously seen in DFT calculations using excited frozen core Aluminium PAW potentials [56].

DFT calculations in the bulk Na lattice were performed using the Abinit code [57], with the PBE generalised gradient expansion for the exchange-correlation energy [40]. An accurate sampling of the bcc Brillouin zone is achieved using shifted 32x32x32 Monkhorst pack grids [58] for charge states up to +2 electrons ionised out of the core K and L shells. 16x16x16 grids were used for +3 and +4 core ionised potentials due to the otherwise impractical amount of RAM needed to represent the increasing number of occupied bands. All density-of states results have been converged with respect to the number of electron bands and auxiliary state plane wave basis set. A continuous density of states was generated by using a Gaussian smearing function of full width half maximum 0.1 eV for each k point, except for the angular momentum projected density of states, for which the tetrahedron method is used. Note

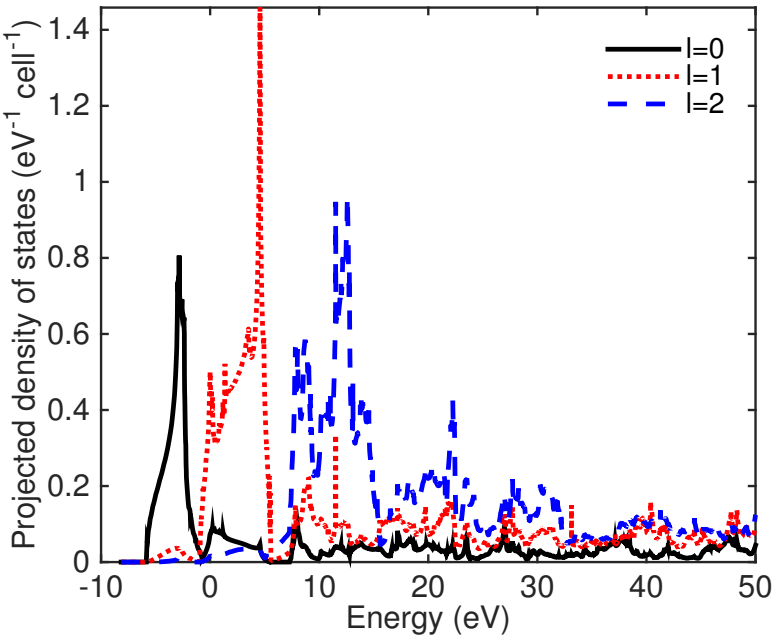

Figure 2.10: Angular momentum decomposed density of states for l=0, 1, 2 at $T_e = 29.1$ eV, corresponding to 3 L-shell holes. The broad peaks reproduced by both all-electron and frozen-core potentials in Fig. 2.9 c) resemble rebinding s, p, and d states, consistent with the beginning of M-shell rebinding as has previous been observed using excited core Al pseudopotentials [56].

that in order to achieve convergence in the total energy of 0.5 eV all-electron potentials required a plane wave basis cut off energy over 6 times higher than that for frozen core potentials (15 Hartree compared to 100 Hartree), resulting in much longer calculation times for the all-electron approach.

2.5 Summary

Within this chapter a means of testing the consistency of excited core pseudopotentials with finite temperature, all-electron results has been proposed and performed for Na pseudopotentials. Both approaches predict the same general valence structure supporting the freezing of excited core states occupations as a sound approximation. This agreement has been explicitly demonstrated for pseudo potentials designed to reproduce thermally excited cores,

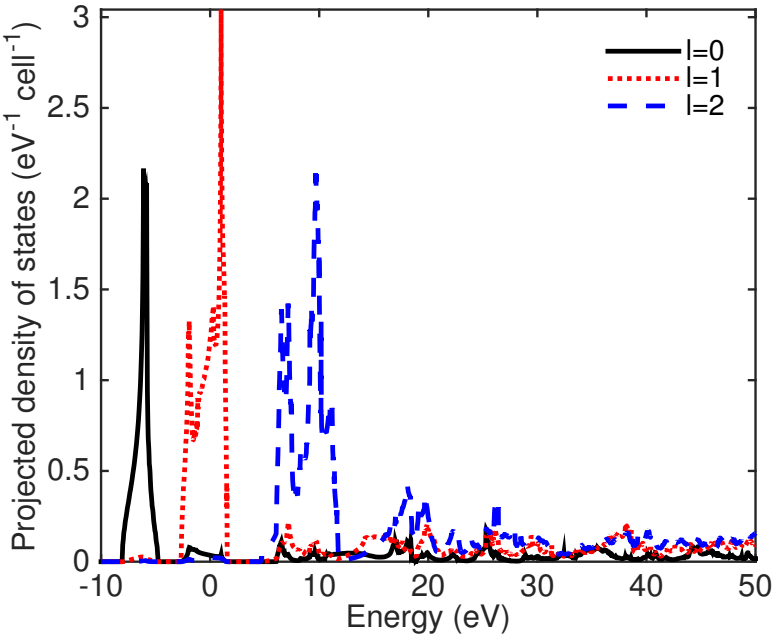

Figure 2.11: Similar to Fig. 2.10 but for $T_e = 44.7$ eV, corresponding to 4 L-shell holes. Compared to Fig. 2.10 the M shell like peaks are now almost entirely of a single angular momentum quantum number l.

however, the fact that the response of excited core states to being placed in a bulk plasma environment does not appear to influence valence behaviour has consequences beyond this. Pseudopotentials for general, excited core configurations also rely on the freezing of core states to be a valid assumption. As previously mentioned in this chapter, it is the application of excited state pseudopotentials to generic excited core configurations that hold the most potential in terms of modelling the properties of dense plasmas - allowing for explicit excited states to be considered rather than just ensemble average quantities and for the treatment of plasmas out of thermal equilibrium.

An example of where excited core pseudopotentials have been applied to dense plasmas is in the modelling of ionisation energies measured in solid density, XFEL heated Al [56]. An isochorically heated Al sample was produced at solid density for which the ion charge state distribution was well constrained via spectroscopic measurements. Producing and probing such systems in this

manner, over femtosecond timescales and in well-characterised plasmas conditions, are particularly advantageous to experimentally investigate the influence of a distribution of ion charge states, and the capability of excited core potentials to model them.

Furthermore, it is worth noting that appropriate, excited potentials have been constructed by directly enforcing the desired core state occupancies during the isolated atom stage of PAW potential construction. The isolated atom DFT calculation does not make use of finite temperature DFT. Instead, excited occupations are directly enforced on core states only, allowing the remaining valence states to achieve their lowest energy occupation (subject to overall charge neutrality). As a result, the number of isolated atom Kohn-Sham orbitals to be computed remains low, and the PAW potential construction process is quick. The ultimate aim is to generate pseudopotentials for general core occupations and will involve directly enforcing excited occupation numbers on core atomic Kohn-Sham orbitals (even if the atomic valence states were thermally occupied). Therefore the fact that we've demonstrated this less than rigorous means of creating excited core states to be consistent with a more rigorous all-electron, finite temperature results is reassuring. Note that the exact value of the imposed core occupation numbers on the isolated atom during the pseudopotential generation process does not significantly affect agreement with all-electron results. What matters is an overall ionisation consistent equal to the thermal expectation value of the all-electron calculation. This is to be expected for small overlap between valence electrons and spherically symmetric core charge by virtue of simple electrostatics.

3

Ab initio calculation of linear response properties

3.1 Introduction

A complete description of a plasma, or any statistical system, requires more than just the thermodynamic mean values for the density, temperature, ionisation or any other state variable. Of both practical and conceptual importance is the manner in which these quantities respond to perturbations, as is - related in quite a beautiful manner [59] - the fluctuation and the distribution of these variables in time and space [60–63]. We might be interested, for example, in how the plasma responds to high power laser beams, X-ray pulses, compression, etc. We might also ask how one physical quantity 'responds to', or more generally can be considered correlated with, the statistical variation of another - for example the correlation between the local instantaneous electron current and electric field strength.

In the previous chapter, excited core pseudopotentials were discussed as a means to both explicitly model ion charge distributions and to calculate properties of their response (specifically the threshold ionisation energy) to

X-rays. The physical accuracy of this picture, though not completely accounting for all many-body exchange and correlation effects, was discussed, along with the delta self-consistent field method and its specific application to finite size systems. From there it was proposed that, for the purposes and conditions explored in this thesis, we can generate physically meaningful excited-ion states by enforcing occupation numbers on isolated-ion, single-particle (Kohn-Sham) wavefunctions, to which the remaining conduction electrons respond instantaneously. On the contrary, whilst a system of interacting, but otherwise free, electrons can be modelled as independent quasi-particles for some purposes [64], the behaviour of collective excitations i.e. plasmons cannot be described within a single-electron picture alone. Furthermore, free electrons can be expected to equilibrate on timescales much shorter than ion charge states and thus a fully dynamic treatment of excitations within a correlated electron system needs to be considered.

A simple, yet ubiquitous, model for describing electrons in a solid or dense plasma comes way of modelling them as a free-electron gas for which the Coulomb interaction amongst the electrons and with surrounding ions is in effect averaged out to produce a uniform positively charged background. This approximation, also known as a Random Phase Approximation (RPA), yields for the long-wavelength response a particularly simple dielectric function [65]:

$$\epsilon = 1 - \frac{\omega_p^2}{\omega^2} \tag{3.1}$$

Where $\omega_p^2 = \frac{4\pi n_e e^2}{m\epsilon_0}$, n_e is the density of electrons, m is their mass and all other quantities have their standard meaning. In order to describe real metals and plasmas we need to also consider scattering events that act to damp electronic current. In its simplest form we can model this process within the relaxation-time approximation leading to the familiar Drude dielectric function, where

$\Gamma = \frac{1}{\Delta t}$ and Δt is the typical time between collisions [65]:

$$\epsilon = 1 - \frac{\omega_p^2}{\omega(\omega + i\Gamma)} \tag{3.2}$$

Eqn. 3.2 does not need any quantum mechanics in its derivation and is reasonably accurate in describing the low-frequency response of metals if classical estimates for the collision frequency are used. Infamously, a naive semi-classical derivation of the relaxation-time parameter using both the Fermi velocity of free electrons and the typical distance between scattering objects (ions) in a typical metal leads to a scattering rate too large by an order of $\sim$100. On the other hand, a purely classical consideration of the motion of electrons is incompatible with the measured electronic specific heat of metals at low temperatures [65]. Consequently, in the condensed matter limit the calculation of the relaxation time parameter (and more generally speaking the collision operator within the Boltzmann equation [66]) requires a thorough, quantum mechanical treatment of the wavelike nature of electrons and their interaction with phonons in a solid such as that provided by the Bloch-Grüneisen equation [66]. In the high-temperature limit one might hope that classical models become more applicable, with the weakened coupling and reduced role of quantum degeneracy effects, however, this limit needs to be established starting from a quantum mechanical description. Practically speaking laser-produced plasmas start in a condensed matter phase before transitioning to WDM, and thus an accurate description of properties in the former phase is also of considerable use.

The description of response functions in the following section opens the way towards considering more general correlation functions of the equilibrium system. Thus far, correlation functions have not had a prominent role to play in this thesis and in many ways, DFT works to replace these quanti-

ties with the, what on first glance might seem somewhat physically opaque, exchange-correlation functional. They are however fundamental quantities in statistical theories of many-body systems, such as the Green's function methods described in the next chapter, as well as serving as useful tools (to the author anyway) for physically visualising the processes that occur in fluctuating and perturbed many-body systems. For these reasons, whilst one *can* simulate these processes from the Hohenberg-Kohn[-Mermin] theorems and their time-dependent generalisations alone, it may also be helpful to revisit some of this chapter with either the contents of chapter 4 in mind or to gain some initial familiarity with the basic concept of quasi-particles, interacting electron-hole pairs, and many-body correlation and exchange effects in both condensed matter and WDM systems [64, 67, 68]. Without this it can become difficult, both conceptually and mathematically rigorously, to understand the limitations of any given approximation to the exchange-correlation functional, and how this may translate to errors in both the calculated response function and the description of fluctuations.

The remainder of this chapter starts with a description of how time-dependent DFT can be used to predict linear response properties, focusing primarily on the dielectric function of a plasma. The fluctuation-dissipation theorem is then applied to describe density correlations in WDM systems, specifically compressed Beryllium and CH plasma. Such correlations are typically quantified in terms of the dynamic structure factor (DSF), a key theoretical quantity in many-body theories, but also directly related to X-Ray Thomson Scattering (XRTS) measurements widely used to determine experimental conditions when studying plasma and WDM in the lab. The results are compared with published experimental data and theoretical calculations, with good agreement. Specific attention is paid to the electronic contribution in order to support the (modified by the author) linear response component of Abinit code, whilst

the ion-ion spatial correlations are dealt with in a more approximate way. In the following chapter, the theory expounded upon here is applied to modelling the opacity of Al plasma across a wide frequency range, thereby incorporating in a consistent manner the response of both free electrons and the ion core, the latter in a slightly more rigorous manner than that used in the previous chapter.

3.2 Response function formalism

We start with the definition of the [inverse] dielectric function as the change in a potential field within a system δV_{int} when an external source of said potential δV_{ext} is applied:

$$\epsilon^{-1} = \frac{\delta V_{int}}{\delta V_{ext}} \tag{3.3}$$

Rather than dealing with the internal potential itself, it is convenient to describe the response in term of the density or current, both of which can be taken to couple linearly to the applied potential for small perturbations. If the unperturbed system satisfies a time-independent Hamiltonian, the response at time t to a perturbation applied at time t' can be written as a function of the time difference $t - t'$. Keeping the spatial dependence arbitrary, this means that the density response $\delta\rho$ to an applied potential can be written in the form [41]:

$$\delta\rho(r,t) = \int_V \int_{-\infty}^{t} \chi(r,r',t-t')\ \delta v_{ext}(r',t')\ dt\ d^3r'. \tag{3.4}$$

Fourier transforming with respect to r, r', and $t - t'$ we find:

$$\delta\rho(q,\omega) = \int_{V_q} \chi(q,q',\omega)\ \delta v_{ext}(q',\omega)\ d^3q'. \tag{3.5}$$

For the special case of periodic boundary conditions it is helpful to rewrite the previous equation in the form:

$$\delta\rho_G(q,\omega) = \sum_{G'} \chi_{GG'}(q,\omega)\ \delta v_{ext\ G'}(q,\omega). \tag{3.6}$$

Here, G and G' are reciprocal lattice vectors and q lies within the first Brillouin zone of the system. The density and current response functions form the basis for defining further key quantities such as the inverse dielectric function ϵ^{-1} [69]:

$$\begin{aligned} \epsilon^{-1}_{GG'}(q,\omega) &= 1 + V_C \chi^{\rho\rho}_{GG'}(q,\omega) \\ &= 1 + \frac{4\pi}{\omega^2}\chi^{jj}_{GG'}(q,\omega) \end{aligned} \tag{3.7}$$

Where $V_C = \frac{4\pi}{(G+q)^2}$ is the Coulomb interaction kernel, $\chi^{\rho\rho}$ indicates the density response to a perturbation coupling to the density, and χ^{jj} the current response to a perturbation coupling to the current.

Note that the Fourier transform from time to frequency space is defined with a small, positive, imaginary component $+i\eta$ for the frequency. Mathematically this is necessary to properly define the Fourier transform when the quantity responding to the perturbation does not converge with time. Physically speaking, this accounts for the fact that our measurement of the response covers a finite period of time after the perturbation was introduced. Of course, we hope that the exact value of η parameter does not drastically affect our predictions and so that the limit of $\eta \to 0$ may ultimately be taken.

The above has all been standard linear response theory covering a wide variety of systems. It is important however to note that for our purposes the limit of η needs to be handled with care, specifically in its value relative to the smallest energy gap between states of differing occupation $\Delta\epsilon$. In practice, all of the DFT calculations here will be performed for a finite number of states determined by the size of the simulation box and the finite number

of points sampling the Brillouin zone. As a result, the continuum limit is never reached and the gap between successive eigenvalues remains numerically finite. The technical limitations of a finite system size are only apparent over timescales comparable to $\sim \frac{1}{\Delta\epsilon}$. Therefore, in order for us to observe non-reversible dissipative behaviour, we need to cut off our measurement after a time $\frac{1}{\eta} << \frac{1}{\Delta\epsilon}$.

For real, macroscopic systems the $\frac{1}{\Delta\epsilon}$ timescale associated with ergodicity far outstrips any actual measurement time. If the measured system is simply one component coupled to a much larger system, let's call the environment, a finite measurement time satisfying these criteria manifests as irreversible dissipation into the environment, a.k.a. damping. A finite number for η is therefore sometimes used, and its exact value justified, on the basis that it accounts for this damping process. This can work at a phenomenological level by introducing a broadening in frequency space, however, the resulting relaxation time approximation for the dynamic response violates key sum rules for response functions. When damping is accounted for correctly within the theory this broadening arises regardless, and a finite value of η should only be interpreted as representing a finite measurement time. For example, the familiar Drude dielectric function including all of these contributions becomes:

$$\epsilon = 1 - \frac{\omega_p^2}{(\omega + i\eta)(\omega + i\eta + i\Gamma)} \tag{3.8}$$

Where $i\Gamma$ is distinguished from $i\eta$ as a physical damping term arising from scattering off of ions and electrons, rather than from the nature of the measurement process itself.

The above discussions of η apply not only to response properties but also to calculations of fluctuations within a finite timescale. The fluctuation-dissipation theorem (FD) for general systems was elegantly derived by Kubo

[59] for both classical and quantum systems. The dynamic structure factor is defined as the Fourier transform of the density fluctuations correlation function:

$$\begin{aligned} S_{GG'}(\mathbf{q},\omega) &= \int \langle \Delta\rho(\mathbf{r},t)\Delta\rho(\mathbf{r}',t')\rangle \, e^{i(\mathbf{q}+\mathbf{G}).\mathbf{r}} e^{i\mathbf{G}'.\mathbf{r}'} e^{i\omega(t-t')} \\ &\qquad \mathrm{d}^3r \; \mathrm{d}^3r' \mathrm{d}(t-t') \\ &= \langle \Delta\rho\Delta\rho\rangle^{>}_{GG'}(\mathbf{q},\omega) \end{aligned} \tag{3.9}$$

Kubo relates S to the retarded density-density response function describing the density response at $(\mathbf{r}',t')$ to a perturbation of the density (say due to coupling with an external field) at $(\mathbf{r},t)$:

$$\begin{aligned} \chi^R_{GG'}(\mathbf{q},\omega) &= \int \frac{i}{\hbar}\Theta(t-t') \, \langle \Delta\rho(\mathbf{r},t)\Delta\rho(\mathbf{r}',t')\rangle \, e^{i(\mathbf{q}+\mathbf{G}).\mathbf{r}} e^{i\mathbf{G}'.\mathbf{r}'} e^{i\omega(t-t')} \\ &\qquad \mathrm{d}^3r \; \mathrm{d}^3r' \mathrm{d}(t-t') \\ &= \langle \Delta\rho\Delta\rho\rangle^{R}_{GG'}(\mathbf{q},\omega) \end{aligned} \tag{3.10}$$

Where $\Theta(x)$ is the Heaviside function. Kubo finds:

$$\langle \Delta\rho\Delta\rho\rangle^{>}_{GG'}(\mathbf{q},\omega) = \left[\frac{\mathrm{Im}\chi^R_{GG'}(\omega)}{1-e^{-\beta\omega}}\right] \tag{3.11}$$

Conversely we can also define the advanced density response function by making the replacement $\Theta(x) \rightarrow \Theta(-x)$[1]. In which case η then needs to change sign to indicate that $\Delta\rho(\mathbf{r},t)$ occurs a finite, albeit long, time *before* $\Delta\rho(\mathbf{r}',t')$, with the result:

[1]There is also an additional density correlation function $\langle \Delta\rho\Delta\rho\rangle^{<}_{GG'}(\mathbf{q},\omega)$ in which the order of the operators $\Delta\rho(\mathbf{r},t)$ and $\Delta\rho(\mathbf{r}',t')$ is flipped. For systems in equilibrium the general correlation functions $\langle AB\rangle^{>}$ and $\langle AB\rangle^{<}$ are related by detailed balance and so there is no real need to complicate the discussion by introducing them here

$$\chi^{R/A}_{GG'}(\mathbf{q},\omega) = \chi_{GG'}(\mathbf{q},\omega \pm i\eta) \tag{3.12}$$

Unless otherwise indicated any response function from here on without a superscript, such as χ or ϵ, should be understood as the retarded quantity. Similar to Eqn. 3.11, we can also calculate the electric potential fluctuations:

$$\langle \Delta V \Delta V \rangle^{>}_{GG'}(\mathbf{q},\omega) = \left[\frac{\mathrm{Im}\epsilon^{-1}_{GG'}(\omega)}{1 - e^{-\beta\omega}} \right] \tag{3.13}$$

As with the linear response, the result for the frequency-resolved Fourier transform of $\Delta\rho$ in time is in part dictated by how long we choose to wait and whether the system can undergo a full ergodic cycle allowing for $\Delta\rho$ to repeat on itself. Whereas in Newtonian mechanics we are perhaps more used to treating the diffusive motion of a particle in empty space, the frequency/energy-resolved phase space means we must be careful when simultaneously taking the size of our system and the measurement time to infinity. The appearance of non-oscillating, diffusive ($\omega \to 0$) fluctuations is contingent on this correctly handling of this limit and any physical, collision driven, diffusive processes should be accounted for in the calculation of χ directly rather than via η.

Finally, note that Eqn. 3.11 and 3.13 are exact for an equilibrium system. It does not depend on the fluctuations $\Delta\rho(\mathbf{r},t)$ being small, and is limited only by the accuracy in obtaining χ. Higher order response functions are instead related to higher order correlations [70], describing the shape of the statistical distribution of $\Delta\rho(\mathbf{r},t)$ in addition to the variance described by Eqn. 3.11 and 3.13.

3.3 Time-dependent DFT

Far from being only a theory of ground state and equilibrium properties, time dependent DFT (TDDFT) rigorously extends the Hohenberg-Kohn theorems to systems under the influence of a time-dependent external potential, $\Delta v_{ext}(t)$ [71, 72]. The resulting time-dependent Kohn-Sham equation is then:

$$\left[\frac{-\hbar^2}{2m_e}\nabla^2 + v_{Hartree} + v_{xc}\left[n(\mathbf{r}, t' \leq t)\right] + \Delta v_{ext}(\mathbf{r}, t)\right]\left|\psi_n^{KS}\right\rangle = i\frac{\partial}{\partial t}\left|\psi_n^{KS}\right\rangle \tag{3.14}$$

Where the exchange-correlation term v_{xc} is a functional of the entire history of the electron density up to the present time t. Real-time TDDFT involves directly evolving Eqn. 3.14 in time whilst paying careful attention to the propagation of errors associated with numerical schemes and maintaining unitary evolution. An alternative approach not without its own limitations is available if, as is often the case, we are primarily interested in the linear response only. Consider first the simpler case of the linear response properties of a non-interacting system. Time-dependent perturbation theory then provides us with the density response to a perturbation coupling linearly to the density as [41]:

$$\chi^{0\ \rho\rho}_{GG'}(\omega, \mathbf{q}) = \sum_{n,m} \frac{\left[f(\epsilon_m^{KS}) - f(\epsilon_n^{KS}\right]\left\langle\psi_m^{KS}\middle|e^{i(\mathbf{G}+\mathbf{q}).\mathbf{r}}\middle|\psi_n^{KS}\right\rangle\left\langle\psi_n^{KS}\middle|e^{i(\mathbf{G}'+\mathbf{q}).\mathbf{r}}\middle|\psi_m^{KS}\right\rangle}{\omega + i\eta + \epsilon_n^{KS} - \epsilon_m^{KS}}. \tag{3.15}$$

From now on I will drop the superscripts $^{\rho\rho}$, and the response functions χ^0 and χ should be interpreted as those of the density-density variety unless otherwise stated. Whilst the Kohn-Sham reference system consists of non-interacting particles, the physical system itself is of course interacting and as such we cannot use Eqn. 3.15 on its own. Eqn. 3.14 indicates that we also need to account for changes to the Hartree and exchange-correlation potentials

that result from the perturbed electron density. The proper first-order density response function χ is then correctly expressed as:

$$\begin{aligned}\chi = \frac{\partial \rho}{\partial v_{ext}} &= \chi^0 \left[1 + \frac{\partial v_{KS}}{\partial \rho}\frac{\partial \rho}{\partial v_{ext}}\right] \\ &= \chi^0 \left[1 + K\chi\right] \\ &= \frac{\chi^0}{1 - K\chi^0}\end{aligned} \tag{3.16}$$

Where: $K = \frac{\partial}{\partial \rho}[v_{Hartree} + v_{xc}] = V_C + \frac{\partial v_{xc}}{\partial \rho}$. The frequency dependence and tensor nature of these quantities has been suppressed for brevity. Once we have access to the density response function we can easily calculate the dielectric function and corresponding optical properties in terms of the Coulomb interaction V_C using:

$$\begin{aligned}\epsilon^{-1} = \frac{\partial v_{int}}{\partial v_{ext}} &= 1 + V_C\chi \\ \Rightarrow \epsilon &= \frac{1}{1 + V_C\chi}\end{aligned} \tag{3.17}$$

As with time-independent DFT, the usefulness of Eqn. 3.16 and 3.17 relies upon accurate models for exchange-correlation effects, this time through the exchange-correlation kernel $\partial v_{xc}/\partial \rho$. Unlike in equilibrium DFT, the proper expression for the latter must be time-dependent in order to account for the systems dynamics and relaxation following a density perturbation $\delta\rho$. Much ongoing research is focused on the development and application of new time-dependent kernels. Static, adiabatic, kernels based on the LDA and GGA have seen application in warm dense matter and plasma physics, as has the widely used Random Phase Approximation (RPA) for which the term $\partial v_{xc}/\partial \rho$ is simply neglected, leading to the much simpler RPA expression for the dielectric function:

$$\epsilon = 1 - V_C \chi^0 \tag{3.18}$$

The RPA comes across as quite a severe approximation, neglecting the very exchange-correlation effects that time-independent DFT is supposed to make more manageable. Following multiple past calculations in the literature, the impact of any of the available (almost always static) approximations for the exchange-correlation kernel on predicted absorption coefficients and other such quantities related to the dielectric function has been the subject of considerable discussion. In some cases, including an LDA or GGA kernel resulted in worse predictions for the optical absorption when compared to the RPA, whilst calculations of electron stopping powers and dynamic structure factors appear to benefit inclusion of the exchange-correlation effects (see [54] and references therein).

To better illustrate the limitations of the RPA, and what accurate exchange-correlation kernels might help to describe in dense plasmas and WDM, it is helpful to expand the RPA density response in terms of the non-interacting response:

$$\chi = \chi^0 + \chi^0 V_C \chi^0 + \chi^0 V_C \chi^0 V_C \chi^0 + ... \tag{3.19}$$

From Eqn. 3.19 we see that the RPA does account for the Coulomb interaction up to infinite order in e^2. The crucial limitation, however, is that the electron density is treated as a structure-less charged fluid such that the mean equilibrated density is the source of interactions for each V_C. As a result, each of these Coulomb scattering events involves both the thermodynamic and quantum mechanical expectation value for the density, meaning that information regarding the exact electron configuration of the plasma is lost. For simplicity consider the excitations of particle-hole e-$\bar{e}$ pairs by an external electric po-

tential γ in a uniform electron gas. In terms of Feynman diagrams, the RPA density response is:

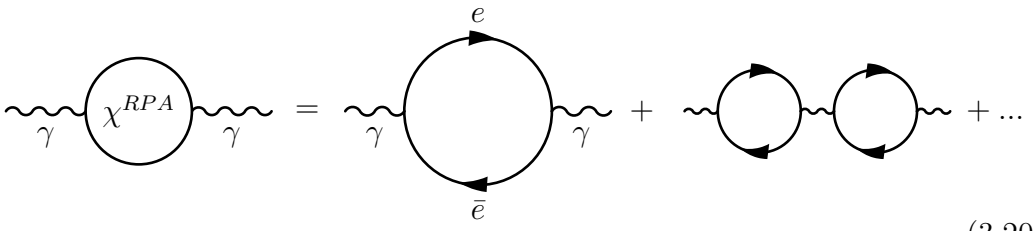

(3.20)

Following from the discussion in chapter 1, the Hartree potential (and by extension the RPA) does not describe the dynamic plasma response to particle motion referred to as the correlation term. The motion of electrons and holes in diagram 3.20, therefore, ought to include this response both individually and, because they are produced in pairs, to the creation of the other. The individual contribution will be considered in more depth in the next chapter. Electron-hole interactions meanwhile can be expected to become increasingly important at length scales over which the plasma is unable to screen.

In the context of DFT perturbation theory, and this thesis in general, the RPA will refer to, unless otherwise stated, the above approximations in which electron-electron scattering during the response function calculation is ignored. Note that in this approximation, the initial DFT calculation that provides the input wavefunctions and energies for Eqn. 3.15 still makes use of an exchange-correlation energy functional, within which electron-electron collisions are implicitly taken into account. This is a somewhat different meaning for the RPA than that used in other areas of plasma physics, where it denotes additional approximations regarding not only electron-electron collisions but also electron-ion collisions. Fortunately, the power of multi-centred DFT calculations is that including ion-electron scattering in the equilibrium calculation

is simply a matter of solving the Kohn-Sham equations for a given set of ion positions. When calculating response functions in multi-centred DFT calculation we must take care to account not only for the diagonal elements of a response tensor but also for any off-diagonal terms coupling perturbation and response at different wavevectors. Within the RPA approximation, the only source for these off-diagonal terms comes from the inhomogeneous ion distribution that introduces an explicit position dependence to our response functions, rather than being solely a function of the distance between applied perturbation and measured response.

Measurements for bulk properties of matter require averaging over the entire system, as a result, it is the diagonal elements of χ and other response functions that ultimately determine what is observed. Looking back at the expansion in Eqn. 3.19 we can see that the off-diagonal elements of χ^0 do in fact contribute to the diagonal elements of χ via scattering events to arbitrary order (more specifically, controlled by the number of elements computed in the tensor) resulting from the spatial distribution of ions. By contrast in other plasma physics literature, normally those that do not include TDDFT calculations, the RPA refers to the rather more severe approximation of completely neglecting all off-diagonal elements, both the electron-electron and electron-ion collisions contributions.

A final consequence for all calculations that use the DFT-RPA expression for the response kernel (see Eqn. 3.18), or indeed any kernel K that is not explicitly frequency-dependent, is that the poles of $\chi(\omega)$ are located at energies corresponding to the differences of Kohn-Sham eigenvalues. It is well known that the differences of Kohn-Sham eigenvalues, especially in bulk systems, are often a poor prediction for energy gaps resulting in the so-called 'band-gap' problem of DFT. This arises in large part because the Kohn-Sham equations, for an exchange-correlation potential that is an explicit functional of density

only, provides the same external potential for all states and is thus unable to correct for the self-interaction term by which an electron erroneously experiences its own Coulomb interaction via the Hartree term. As a result, we should not at this point expect the RPA opacity to accurately predict the threshold energies for bound-free or bound-bound absorption features.

This erroneous interaction would in principle be removed via the inclusion of the frequency-dependent, exact-exchange contribution to TDDFT kernel [73]. Alternatively once can use explicitly orbital-dependent exchange-correlation potentials, such as the HSE functional [74, 75], which include some fraction of exact exchange [76], thus expanding the dependence of the single-particle equations to include quantities other than the density alone. The latter marks a departure from the original non-interacting Kohn-Sham reference system by explicitly including within the Hamiltonian some fraction of the Coulomb interaction between individual single-particle states, in addition to an orbital independent potential provided by a chosen exchange-correlation density functional. The logical extension of this effort to correct single-particle energies, and that does not rely on any fraction of a prior chosen exchange-correlation potential, can be found in self-consistent many-body theory calculations for the single-particle wavefunctions. Fully self-consistent calculations are computationally extremely demanding, and in the next chapter, I will instead use the relatively cheap DFT-RPA calculation of the response function discussed in this chapter as a starting point to construct finite-temperature single-particle equations yielding experimentally accurate single-particle energies and associated band-gaps.

The latter calculations will be computationally expensive, but the extension of 'DFT + many-body corrections' to finite temperatures provides an important means to check and validate the cheaper, but a priori parameterised, treatments of exchange-correlation such as those used in hybrid-functionals

and advanced exchange-correlation kernels. In particular, by starting with a reasonably accurate calculation of the dielectric response using DFT-RPA, one can consider perhaps more exotic conditions not well captured by the usual parameterisation of exchange-correlation effects within functionals. The next chapter will also make clear the connection with the vast amount of work already done in many-body theory and provides a route to calculating other physical properties of interest such as particle lifetimes and spectral line widths. For now, however, the next section of this chapter will examine some intricacies and peculiarities that arise when using TDDFT linear response theory to extract the dielectric function ϵ of plasmas and metals.

3.4 Intricacies for plasmas and metals

An important limit when considering plasmas and metals is the long-wavelength, low-frequency response that characterises the dc conductivity of a system. More generally we will also interested in long-wavelength response at finite frequencies. In particular, with the typical length scale of inhomogeneities in solid density systems being of order < 0.1 nm, this limit covers radiation at frequencies up to at least the XUV range and below ($\lambda > 5$nm).[2] The conductivity and dielectric function are of course related by:

$$\begin{gathered} \epsilon(\omega) = 1 + \frac{i\sigma(\omega)}{\omega + i\eta} \\ \Downarrow \\ \sigma_{dc} = \lim_{\omega\to 0} \sigma_{mac}(\omega) = \lim_{\omega\to 0} \left[\epsilon_{mac}(\omega) - 1\right](\omega + i\eta) \end{gathered} \tag{3.21}$$

Where the macroscopic dielectric, $\epsilon_{mac}(\omega) = 1/[\epsilon^{-1}_{00}(q \to 0, \omega)]$, defines the ratio of applied field to internal field whilst the former is adjusted to keep

[2]High energy transitions involving bound states are also typically covered by this limit due to the highly localised nature of the core ion core.

the external field fixed. This encompasses, for example, the point to point conductivity response when a fixed potential difference is applied to the system. Note that it is the off-diagonal elements that couple the different Fourier components that is responsible for the difference between ϵ_{mac} and ϵ_{00} , these required to distinguish between the 'local-field' experienced by a charge in the plasma from that of the average. The 'corrections' to the macroscopic dielectric function that result from correcting accounting for its tensor nature are referred to as Local Field Corrections (LFC). Only in homogenous systems (which, for a given ion configuration, will not be the case for us) do the effects of LFC completely vanish. DFT calculations for the dynamic conductivity of plasmas and warm dense matter have long been performed by applying the Kubo-Greenwood formula for the long-wavelength conductivity [77]:

$$\begin{aligned}\sigma_{00}(\omega, \mathbf{q} \to 0) =& \frac{2\pi}{3V} \sum_{i,j=1} \sum_{\alpha=1}^{3} \frac{(f(\epsilon_{i,\mathbf{k}}^{KS}) - f(\epsilon_{j,\mathbf{k}}^{KS}))}{\epsilon_{i,\mathbf{k}}^{KS} - \epsilon_{j,\mathbf{k}}^{KS}} \\ & \frac{|\left\langle \psi_{j,\mathbf{k}}^{KS} \middle| \nabla_\alpha \middle| \psi_{i,\mathbf{k}}^{KS} \right\rangle|^2}{\omega + i\eta + \epsilon_n^{KS} - \epsilon_m^{KS}}\end{aligned} \tag{3.22}$$

The matrix elements featured in Eqn. 3.22 may be identified with the long-wavelength limit of those in Eqn. 3.15 by apply the so-called **k.p** perturbation theory:

$$\begin{aligned}\left\langle \psi_m^{KS} \middle| e^{\mathbf{q}.\mathbf{r}} \middle| \psi_n^{KS} \right\rangle &= \left\langle \psi_m^{KS} \middle| \left[1 + \mathbf{q}.\mathbf{r} + ...\right] \middle| \psi_n^{KS} \right\rangle \\ &= \mathbf{q}. \left\langle \psi_m^{KS} \middle| \mathbf{r} \middle| \psi_n^{KS} \right\rangle + O(q^2) \\ &= \mathbf{q}. \left\langle \psi_m^{KS} \middle| \frac{[\mathbf{H},\, \mathbf{r}]}{\epsilon_m - \epsilon_n} \middle| \psi_n^{KS} \right\rangle + O(q^2) \\ &= \mathbf{q}. \frac{\left\langle \psi_m^{KS} \middle| \nabla \middle| \psi_n^{KS} \right\rangle}{\epsilon_m - \epsilon_n} + O(q^2)\end{aligned} \tag{3.23}$$

Compare this with the expression for the long-wavelength limit conductivity obtained from 3.15 if LFC contributions are ignored:

$$\sigma_{mac}(\omega, \mathbf{q} \to 0) = \sum_{n,m} \frac{\omega + i\eta}{(\epsilon_m - \epsilon_n)} \frac{f(\epsilon_m^{KS}) - f(\epsilon_n^{KS})}{(\epsilon_m - \epsilon_n)} \frac{|\left\langle \psi_m^{KS} \middle| \nabla \middle| \psi_n^{KS} \right\rangle|^2}{\omega + i\eta + \epsilon_n^{KS} - \epsilon_m^{KS}} \quad (3.24)$$

Eqn. 3.22 and 3.24 are identical if either of the limits $\eta \to 0$ or $\Delta\epsilon \to 0$ is taken first, however Eqn. 3.24 becomes numerically unstable in the latter limit especially if the Lorentzian frequency dependence is replaced with more computationally preferable functions. Indeed, the Abinit code provides considerable speed advantages if the spectral function χ^s is first calculated by considering only the imaginary component of Eqn. 3.15 with the Lorentzian replaced by either Gaussian functions or finite triangle elements. From χ^s Abinit calculates the full response function via a Hilbert transformation:

$$\chi^0(\omega) = \int_{-\infty}^{\infty} \frac{\chi^S(\omega')}{\omega - \omega' + i\delta} d\omega' \ , \qquad \chi^S(\omega) = \mathrm{Im}(\chi^0)\ \mathrm{sign}(\omega) \quad (3.25)$$

This approach is suitable when the energy difference $\Delta\epsilon$ is finite, such as for insulators and finite wavelength transitions in metals. For our purposes of calculating the long-wavelength response in plasmas and metals, I have re-written the Abinit code to use Eqn. 3.22 to calculate the real part of the conductivity in the long-wavelength limit. The full complex value of $\epsilon_{00}(\omega, \mathbf{q} \to 0)$ is then recovered through the transformation:

$$\epsilon_{00}(\omega) = 1 + \frac{i}{\omega} \int_0^{\infty} \mathrm{Re}\ \sigma_{00}(\omega') \left[\frac{1}{\omega - \omega' - i\delta} - \frac{1}{\omega + \omega' + i\delta} \right] d\omega' \quad (3.26)$$

Note that the limit of $\delta \to 0$ is not subject to the same physical concerns as η discussed in the previous section, as the transformation serves only as a way

to regain the full complex response function of Eqn. 3.22. The replacement of the long-wavelength dielectric response by Eqn. 3.26 was seen to cure any instabilities arising from the vanishing energy gap in conducting systems. In particular whilst a finite value of η does follow physically speaking from the finite time of the measurement, the practical limitations of only being able to calculate a finite number of wavefunctions means that the value for η in any simulation must be considerably larger than that associated with the actual measurement time if we are to at least qualitatively replicate dissipative behaviour. The choice of exact value for η, or alternatively the 'smearing' width of a Gaussian used to replace any Lorentzian function, is a delicate issue for ab-initio DFT simulations. On the one hand, an excessively large parameter obscure the physical frequency dependence of the response function whilst on the other, too small a value will not replicate the correct, continuous density of states. In practice, this choice of parameter should be chosen based both on what is physically expected for the system and the sensitivity of the result to changes in both smearing parameter and number of state calculated.

Within this thesis, an alternative approach to either Gaussian or Lorentzian smearing has been followed by using finite triangle elements which lack the tails and wings of the former functions. Following from the discussion of reference [78] regarding the dc conductivity, whilst the limit of $\eta \to 0$ faster than the energy gaps of the system leads to unphysical frequency spikes in the conductivity, the integrated conductivity between 2 frequencies is a physically meaningful quantity that converges regardless of the order of limits. The replacement of the Lorentzian in Eqn. 3.22 by triangle functions amounts to constructing a histogram of the spectrum along a frequency grid determined by the width of the triangle element functions. The spectral weight associated with each bin may then be converged with respect to simulation parameter, whilst the bin-spacing/triangle-width, η, provide an associated error. Cru-

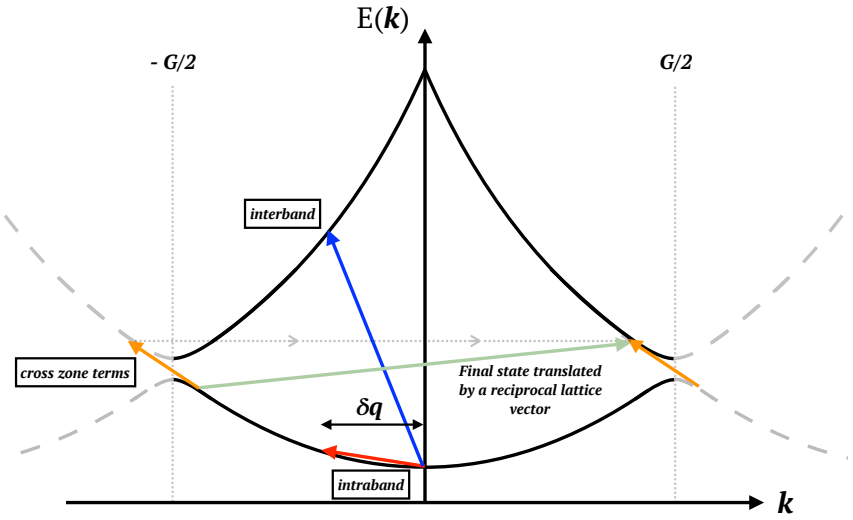

Figure 3.1: Illustrative diagram for the contributions to the response function of a free-electron like system subject to periodic boundary conditions. As well as standard intraband and interband terms, we must also take into account the possibility of cross-terms especially when considering super-cell simulations of low-temperature free-electron like materials, for which the Fermi surface may lie close to the conduction band interception with the boundary of the (super-cell) Brillouin zone.

cially, this does not contain the far off-resonant features that come with both Gaussian and Lorentzian smearing, meaning that we are free to consider response functions over frequency scale for which they vary by multiple orders of magnitude.

A final consequence when dealing with plasmas and metals is the possible presence of intra-band and cross-terms contributions to the dielectric function as shown in Fig. 3.1. Note that as the reduced Brillouin zone is technically constructed via band translations rather than band folding, inter-band transitions can only compensate for ignoring intra-band and cross-terms if the simulation cell is sufficiently large, and the nuclei structure factor sufficiently disordered, that the macroscopic current across the super-cell is negligible owing to Anderson localisation confining each electron state to within a super-cell. In the

author's simulations presented here, these contributions are accounted for by calculating the dielectric function at finite momentum transfer $\mathbf{q}$, for which the Abinit code automatically includes all of the above contributions, and extrapolating the plasma frequency to the $\mathbf{q} = 0$ limit. The low-frequency dielectric function is fitted to a plasmon-pole form:

$$\epsilon^{-1}(q,\omega) = 1 + \frac{(\omega_p^0)^2}{\omega(\omega + \mathrm{i}\nu^q) - (\omega_p^q)^2}, \tag{3.27}$$

Any discrepancy between the finite momentum $\mathbf{q}$ fit values for ω_p^0 and $\omega_p^{q\to 0}$, the latter via the Bohm-Gross relation, and the values obtained for $\mathbf{q} = 0$ was then inserted directly as an additional term for the $\mathbf{q} = 0$ response. In this manner we are able to satisfy the f-sum rule, whilst also treating the intraband conductivity not simply as a Dirac-delta pole term, as is technically the case for a perfect [super] lattice, but with a relaxation time parameter, ν consistent with those interband terms that *do* contribute to a finite dc conductivity owing to disorder within our simulation cell.

In the long-wavelength limit, these contribute to the pole at $\omega = 0$ as shown schematically in Fig. 3.1. A correct treatment of this limit is then essential for the determination of the plasma frequency and low-frequency response of a system. Here I have determined the strength of the pole at $\omega = 0$ by evaluating the dielectric function at finite q and numerically taking the $q \to 0$ limit. At long wavelengths and low frequencies below transitions involving bound states the imaginary part of the inverse dielectric function is well approximated by the single plasmon pole approximation:

$$\epsilon^{-1}(q,\omega) = 1 + \frac{(\omega_p^0)^2}{\omega(\omega + \mathrm{i}\nu^q) - (\omega_p^q)^2}, \tag{3.28}$$

The plasma frequency ω_p^q and broadening ν^q are in general q-dependent. I find the dielectric response at low frequencies to be well fitted by this functional

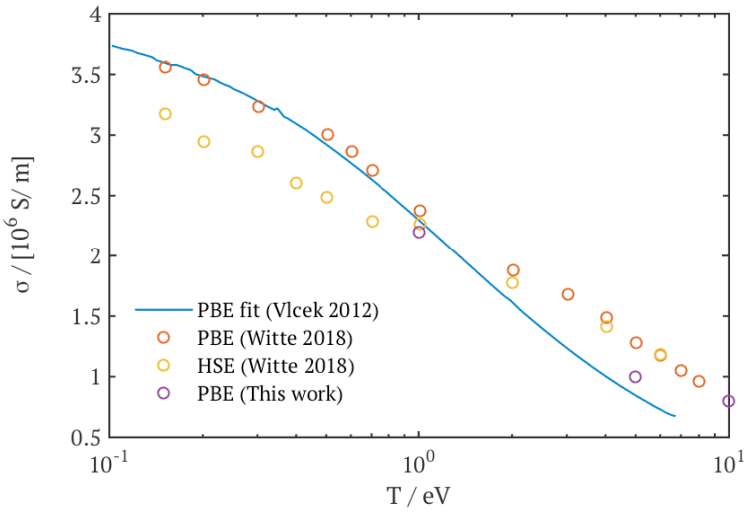

Figure 3.2: Calculated dc conductivity for warm dense Al at solid density compared to the work of references [79] and [80]. The dc conductivity was not the primary focus of the authors Al calculations, discussed more in the following chapter, rather convergence of simulation parameter was concerned with the frequency dependent opacity. The calculations performed by the author are nonetheless consistent with previous work.

form for all conditions studied. The $q \to 0$ plasma frequency, and thus the pole at $\omega = 0$, was then obtained by fitting for ω_p^0 as well as by extrapolating our calculated Bohm-Gross relation for ω_p^q to $q = 0$. The same values were obtained by both methods.

Using this approach, the dc conductivity for warm dense Al was calculated and compared to previous DFT calculations as shown in Fig. 3.2. Simulations using the PBE-GGA exchange-correlation functional for a 32-atom unit cell, with a 2 x 2 x 2 k-point grid sampling the Brillouin zone, are seen to lead to a dc conductivity consistent with the results of previous authors [79, 80].

3.5 The dynamic structure factor

The above method has yielded the response function of a system including the role of LFC. In doing so it has simultaneously computed other elements

of the response function other than the long-wavelength limit relevant for optical properties optical properties. As mentioned earlier in this chapter, these remaining elements are however directly relevant to XRTS measurements of the DSF [81], which can in turn be related to the dielectric function or density response function via the fluctuation-dissipation theorem (Eqn. 3.11). Thus far the calculated response function has not included nuclei motion. We can include this contribution by coupling the electron density response to nuclei motion in Eqn. 3.16:

$$\begin{aligned} \chi_{ee}^{total} &= \frac{\chi_{ee}}{1 - V_C Z \chi^{ii} V_C \chi_{ee}} \\ &= \chi_{ee} + \chi_{ee} V_C Z \chi_{ii} V_C \chi_{ee} + \chi_{ee} V_C Z \chi_{ii} V_C \chi_{ee} V_C Z \chi_{ii} V_C \chi_{ee} + ... \end{aligned} \tag{3.29}$$

The term $V_C Z \chi^{ii}$ acts as an effective vertex term, coupling the electronic response back and forth with the nuclei. Note that just as the electronic term χ_{ee} does not involve nuclei motion, neither should χ_{ii}include the relaxation of the electron density to nuclei motion. Instead, if the response function of a single nucleus without including the motion of others is χ^0_{nn}, then the response function for their collective motion is:

$$\chi_{nn} = \frac{\chi^0_{nn} S_{nn}}{1 + Z V_C \chi^0_{nn} S_{nn}} \tag{3.30}$$

Where χ^0_{nn} is the density response of a single nuclei (with starting position and velocity taken from an MD simulation) moving in the potential of a static electron density, and the instantaneous nuclei structure factor S_{nn} is given by:

$$S_{nn\ \mathbf{G}\mathbf{G}'} = \frac{1}{N} \sum_{i,j}^{N} e^{i\mathbf{G}.\mathbf{r}_i} e^{i\mathbf{G}'.\mathbf{r}_j} \delta(\mathbf{q}) \tag{3.31}$$

Rather than substitute Eqn. 3.29 into Eqn. 3.11, we can show a more general relationship if we now apply the Langreth rules [82] for correlation functions along a closed-time contour. For the triple product of correlation functions one has:

$$(ABC)^{<} = A^R B^R C^{<} + A^R B^{<} C^A + A^{<} B^A C^A \tag{3.32}$$

Applying this to the second term in the expansion of Eqn. 3.29 we have:

$$\begin{aligned} S_{ee}^{total} &= S_{ee} + \chi_{ee}^R V_C \chi_{nn}^R V_C S_{ee} \\ &+ \chi_{ee}^R V_C S_{nn} V_C \chi_{ee}^A + S_{ee} V_C \chi_{nn}^A V_C \chi_{ee}^A + ... \\ &= S_{ee} + (\epsilon_{ee}^{-1} - 1)^R (\epsilon_{nn}^{-1} - 1)^R S_{ee} \\ &+ (\epsilon_{ee}^{-1} - 1)^R S_{nn} (\epsilon_{ee}^{-1} - 1)^A + S_{ee} (\epsilon_{nn}^{-1} - 1)^A (\epsilon_{ee}^{-1} - 1)^A + ... \end{aligned} \tag{3.33}$$

The Langreth rules hold regardless of the details in the thermodynamic averaging. Eqn. 3.33 can, therefore, be applied even to generic non-equilibrium ensembles provided that suitable expressions for S_{nn} and χ are available. For a two-temperature system in which the nuclei motion and electron systems are not together in equilibrium, it a case of substituting in for χ and S their corresponding quantities calculated separately for the electron and nuclei systems at differing temperatures.

Eqn. 3.33 is a very general expression that can be applied to both equilibrium and non-equilibrium conditions. It is close to, but not quite the same as Chihara's decomposition for the dynamic structure factor [83]:

$$S^{ee}(q,\omega) = S^{ee\,0}(q,\omega) + \left[\frac{|\rho_b(q) + \rho_{sc}(q)|^2}{Z} S^{nn}(q,\omega) \right] \tag{3.34}$$

Here, $S^{ee\,0}(q,\omega)$ describes the dynamic fluctuations in density arising from

electron motion alone whilst the remaining term accounts for the combination of bound electrons ρ_b and a screening cloud, ρ_{sc} of free electrons that follow the nuclei motion, $S^{nn}(q,\omega)$. Eqn. 3.34 was derived by Chihara in a similar manner to the above by following linear response theory arguments. As an additional step, $S^{ee\,0}(q,\omega)$ is in practice typically split into two contributions describing correlations amongst free electron and bound electrons separately such that appropriate models may be used accordingly [84, 85]:

$$S^{ee}(q,\omega) = S^{ee\,0}_{free}(q,\omega) + S^{ee\,0}_{bf}(q,\omega) + \left[\frac{|\rho_b(q)+\rho_{sc}(q)|^2}{Z} S^{nn}(q,\omega)\right] \quad (3.35)$$

We can identify the first two terms of Eqn. 3.35 with the first term in the expansion of Eqn. 3.33. As has been stated multiple times in this thesis, DFT combined with efficient PAW potentials allows for a consistent approach to be applied to both free and bound electrons, and in fact without any strict distinction between the two (except of course those bound to the core of pseudopotential). As such the electronic only contribution to the dynamic structure factor can be calculated from a first principles perspective. This ability becomes increasingly important when dealing with strongly coupling effects for which ionisation potential depression and the occurrence of 'hopping states' blurs the distinction between bound and free [2, 86].

The remaining terms describing electron density correlations mediated by nuclei motion differ between Eqn. 3.33 and 3.35. Note that Eqn. 3.33 also contains frequency-dependent tensor products, whilst the electron density following nuclei motion is notably frequency independent in the Chihara decomposition. In reality, of course, the electron-nucleus coupling is a dynamic process and so to recover Eqn. 3.35 we examine the limit that electrons respond adiabatically to a change in ion positions - i.e. the Born-Oppenheimer ap-

proximation. Specifically, there are two important physical assumptions here, one is that ion motion can be treated as a slow perturbation on the timescale of electron response and the second, which does not necessarily follow from the first, is that the electron system is uncorrelated with ion velocities over this timescale as well. We can justify the latter if the specific pure state of the electronic system, as taken from a thermal ensemble of initial states, does not persist on the timescale of ion motion, that is to say, the electrons 're-equilibrate' on such a timescale. This then removes the terms in Eqn. 3.33 featuring both S_{ee} and χ_{nn}, i.e. those describing stochastic contributions to the nuclei motion due to dynamic electron collisions. Once these limits are taken the nuclei contribution in Eqn. 3.33 reduces to:

$$\begin{aligned} S_{ee}^{total} \approx S_{ee} + \chi_{ee}^{R} V_C S_{nn} V_C \chi_{ee}^{A} + \chi_{ee}^{R} V_C \chi_{nn}^{R} V_C \chi_{ee}^{R} V_C S_{nn} V_C \chi_{ee}^{A} \\ + \chi_{ee}^{R} V_C S_{nn} V_C \chi_{ee}^{A} V_C \chi_{nn}^{A} V_C \chi_{ee}^{A} + ... \end{aligned} \tag{3.36}$$

Rather than actually evaluate Eqn. 3.36 it is of course much simpler to use the fact that Born-Oppenheimer DFT-MD simulations automatically calculate changes in the electron density due to nuclei motion within the adiabatic approximation and we may, therefore, replace the nuclei contribution in Eqn. 3.36 with a simple Fourier transform of the mean electron density in time and space of the course of an MD simulation. Naturally, this is the manner in which the nuclei contribution to the dynamic structure factor is frequently calculated in practice.

One key practicality of the Chihara formula lies in the simplicity with which it is to change nuclei structure factors. This is because the nuclei contribution has been reduced to simple scalar products in Fourier space rather than the full tensor treatment above, in which case the bound density and screening

cloud become convolutions with the nuclei positions in real space. Whilst calculating the full dynamic structure factor via Eqn. 3.33 is expensive, we can, however, consider the effect of terms beyond the adiabatic Born-Oppenheimer approximation by performing a similar deconvolution approach. I will restrict the corrections to Eqn. 3.36 to the terms of order V_C^2 , the terms to consider are

$$\Rightarrow \quad \chi_{ee}^R V_C \chi_{nn}^R V_C S_{ee} + \chi_{ee}^R V_C S_{nn} V_C \chi_{ee}^A + S_{ee} V_C \chi_{nn}^A V_C \chi_{ee}^A \tag{3.37}$$

For each individual MD snapshot the nuclei structure factor S_{nn} is in general a tensor. However, when the thermodynamic limit is taken in both time and space, it stands to reason that no particular position in the plasma can be special and so S_{nn} reduces to a function of separation distance in real space. I will call these components of S_{nn} the homogeneous terms, as they are the only non-zero components when the thermodynamic averaging is translationally invariant.

$$\begin{aligned} S_{G-G}^{homog}(\mathbf{q},\omega) = \int \langle \Delta\rho(\mathbf{r},t)\Delta\rho(\mathbf{r}',t')\rangle \, e^{i\mathbf{q}.\mathbf{r}} e^{i\mathbf{G}.(\mathbf{r}-\mathbf{r}')} e^{i\omega(t-t')} \\ \mathrm{d}^3 r \; \mathrm{d}^3 r' \mathrm{d}(t-t') \\ = \langle \Delta\rho\Delta\rho \rangle^{<} (\mathbf{G},\omega)\, \delta(\mathbf{q}) \end{aligned} \tag{3.38}$$

From this we can see that the homogeneous terms are similar to diagonal elements but with the second G index multiplied by -1, the Dirac delta function meanwhile arises from our restriction to periodic boundary conditions. As we do need to take the thermodynamic limit eventually, it is the homogeneous terms of S_{ee}^{total} that correspond to the physically measured quantities in XRTS scattering experiments. However for any given MD snapshot the inhomogneous terms of the structure factors and response tensors in Eqn. 3.37

will be correlated between electrons and nuclei and thus they may provide a non-vanishing contribution to the measured, homogeneous, components of the total structure factor. In order to make a connection with the Chihara formula, in which only the homogeneous terms explicitly appear, we can define an effective, bound-plus-screening density by deconvolving the second term in Eqn. 3.37 with respect to the homogeneous nuclei-nuclei structure factor, or in Fourier space:

$$\rho^{b+s}(\mathbf{G},\omega,\mathbf{q}) = \frac{\chi^R_{ee} V_C S_{nn} V_C \chi^A_{ee}}{S^{homog}_{nn}(\mathbf{G},\omega)}\,\delta(\mathbf{q}) \tag{3.39}$$

Similar quantities can be defined for the remaining terms in equation 3.38 by deconvolving with either the electronic or nuclei structure factors. On the other hand, it is often sufficient in fitting experimental data to approximate the nuclei structure factor as a Dirac-delta in frequency space. For the calculations in this thesis I will limit myself to this approximation[3]. The first and third terms in Eqn. 3.33 may be identified with the Chihara formula's electronic and nuclei 'drag' terms respectively. One of the other great challenges of TDDFT calculations for the dynamic structure factor lies in applying it to sufficiently many snapshots from an MD simulation and in a sufficiently large box that an accurate nuclei structure factor S_{nn}can be obtained. For these reasons, future work may need to consider defining effective terms such as Eqn. 3.39 from first principles perspective for which changes in the homogenous terms of the nuclei structure factor can be easily accounted for.

[3]Of course a description of ion dynamics would be preferable, and so I will mention briefly here that an approximate description of χ^0_{nn} can be made by treating the nuclei as classical particles moving under a potential obtained by expanding the electron density about the nuclei.

3.6 Application to XRTS measurements in CH and Be plasma.

The previous section has detailed how ab initio calculations of the full tensor density response function may be utilised to simulate, and construct models for, inter-particle correlations and energy exchange including the role of LFC and strong electron-nuclei coupling. In practice, DFT is more widely used to obtain the elastic scattering component by Fourier transforming in space and time the electron density obtained via MD simulations within the Born-Oppenheimer approximation. The subsequent adiabatic change in the electron density with shifting nuclei positions is equivalent to the contribution of $\mathrm{Re}\epsilon_{ee}^{-1}(\omega \to 0)$ to the third term in Eqn. 3.33. As mentioned previously, this is a sufficient approximation when the nuclei motion occurs at frequencies $\sim \omega_n$ much lower than electron response; $\mathrm{Re}\epsilon_{ee}^{-1}(\omega_n) \approx \mathrm{Re}\epsilon_{ee}^{-1}(\omega \to 0)$; and below the collective excitation energies of the electron system; $\mathrm{Im}\epsilon_{ee}^{-1}(\omega_n) \approx 0$, $S^{ee}(\omega_n) \approx 0$.[4] Unlike the approach of the previous section, simply Fourier transforming the total electron density does not on its own provide for any easy distinction between bound electrons and the screening cloud contributing to the elastic feature. Of course, in terms of the reproducing the observed total dynamic structure factor such a decomposition is unnecessary and DFT may thus be considered to be advantageous in the sense that both contributions are treated on an equal footing. The benefits of a full response function decompo-

[4] A questionable difference however is the manner in which the long-wavelength limit is dealt with. In evolving the system with Born-Oppenheimer molecular dynamics, the electrons instantaneously equilibrate to the new nuclei positions such that there is no process for the nuclei system to dissipate energy into and heat up the electrons. The dissipative component of the electron response $\mathrm{Im}\epsilon_{ee}^{-1}$, for free electrons anyway, might be expected to vanish at $\omega = 0$ for finite momentum transfer however in the long-wavelength limit $q \to 0$ the absorption process could be identified with an acceleration of the electron system as a whole. Physically then, this contribution to Eqn. 3.33 could be identified by the dissipation of energy into the electron system if all nuclei were suddenly accelerated uniformly in a given direction.

sition, on the other hand, is in it being able to distinguish these contributions so that we might inform and guide theory when such an ecumenical approach to electron behaviour is less practical or otherwise unavailable.

More recently, DFT has also begun to be applied to calculating the electronic contribution to the dynamic structure factor via the fluctuation-dissipation theorem [80, 87–90]. Close to the time that the work of this chapter was being completed by the author, simulations using real-time TDDFT combined with Ehrenfest molecular dynamics[5] were published in which the dynamic structure factor of Beryllium plasma was calculated without the need to apply a decomposition into bound and free states as inputs for the Chihara formula by Baczewski et al. [51]. In their work, the density response function of the electron system is calculated in real-time whilst the nuclei simultaneously moved in response to the perturbed, non-equilibrium electron system, from the response function the dynamic electron structure factor is obtained via the fluctuation-dissipation theorem.

The procedure of reference [51] is similar to that followed in the previous section, with the exception that the extension to differing ion and electron temperatures is perhaps less clear. The fluctuation-dissipation theorem arises from considerations of detailed balance for a system in equilibrium, and whilst relations between the different definitions of the density-density correlation functions exist for non-equilibrium systems, they do not satisfy the same simple formula 3.11. Consequently Eqn. 3.11 may only be applied to the electron density response, even if it includes nuclei coupling via Ehrenfest dynamics, if the electron system remains in equilibrium during the time t of the corre-

[5]Within Ehrenfast dynamics, nuclei are treated classically and the forces on them calculated via the Hellmann-Feynman theorem just as with Born-Oppenheimer dynamics. However in this case, rather than solving the time-independent Shrödinger equation at each time step, the electronic system is instead evolved dynamically simultaneously with the nuclei motion. Within DFT simulations the electronic evolution is usually described within real-time, TDDFT [91].

lation $\langle\rho(t)\rho(0)\rangle$. Note that the Langreth rules used in deriving Eqn. 3.33 hold regardless of the averaging procedure, and thus regardless of whether the electron-nuclei systems are together in equilibrium.

In Fig. 3.4 the dynamic structure factor measured in warm dense Beryllium [92] is shown together with the simulations of reference [51] and those of this author following convolution with the XRTS source profile. The electronic-only contribution to the dynamic structure factor has been calculated following the procedures of the previous sections. Rather than computing the contribution due to nuclei motion using the full response function tensor as in the previous section, the Born-Oppenheimer approximation was made and the combined screening cloud plus bound electron density computed by simply shifting a single Beryllium nucleus and Fourier transforming the density change (Fig. 3.3). This approach is similar in essence to the deconvolution procedure used in reference [89] for extracting the screening charge and bound state density from molecular dynamics simulations. As the principal aim was to examine the codes ability to reproduce the electronic contribution, the nuclei-nuclei structure factor was not itself calculated but instead a value taken from the results of reference [89]. The same approach was used to obtain a predicted dynamic structure factor for dense CH plasma under the conditions of reference [23], with the nuclei-nuclei structure factor taken to be ~ 1 as befits the large k vector probed $k = 6.1\text{Å}^{-1}$. Most interestingly, this approach is also able to reproduce the observed measurements reasonably well (see Fig. 3.5).

The simulations presented here were part of a somewhat speculative test, in that they were to check the ability of the Abinit code to accurately predict the dielectric function at the short wavelengths probed by these experiments. To this end, the Berylium measurements were chosen as a dataset already shown to be reproducible with using other TDDFT codes. The CH measurements meanwhile, stand out in that the authors of reference [23] were only

able to reproduce their experimental data with a Carbon ionisation state of +5, a number inconsistent with any of the Stewart-Pyatt [93], Thomas-Fermi or modified Ecker-Kroll [94, 95] ionisation potential depression (IPD) models commonly applied to dense plasmas. Note, however, that subsequent IPD models have since been proposed in which the Hydrogen nuclei may have led to a thus far unaccounted for contribution to the screening length, resulting in +5 ionisation states.

Whilst it is interesting to note that reasonably good agreement with the CH data can be achieved using the author's DFT simulations, the calculations were too expensive to fully cover the not inconsiderable density and temperature gradients predicted to occur during the experiment. As such a full analysis is beyond the remit of this work, as is a complete study of the sensitivity of the simulations to variations in temperature, density, and the nuclei-nuclei structure factor. TDDFT calculations for the full response tensor are expensive and in practice, their application to interpreting XRTS data will likely need to be limited to cases where other approaches fail, or to the generation of model parameters for further simulations as suggested in the previous section. The alternative approach of using real-time TDDFT to perform calculations for a specific $\mathbf{k}$ vector does represent better scalability in terms of both system size and temperature, furthermore, any non-linear response is automatically taken into consideration. However, it should be noted that the linear response limit of real-time simulations needs to be taken with some care (see supplementary material of reference [51]) and whilst the non-linear response does provide access to higher-order density correlation functions, it does not contribute to the two-point dynamic structure factor of Eqn. 3.9.

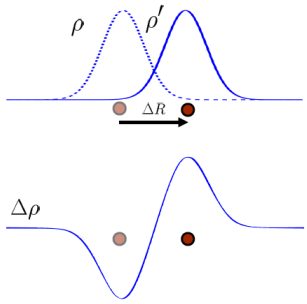

Figure 3.3: Illustration of the technique used to calculate the combined, bound-plus-screening term, $|\rho_b(q) + \rho_{sc}(q)|^2$ contribution in Eqn. 3.34. Two DFT calculations of the electron density ρ and ρ' are performed, differing by a shift ΔR in the position of a single nucleus. The resulting change in density $\Delta\rho$ is Fourier transformed to obtain the form factor $|\rho_b(q) + \rho_{sc}(q)|^2$ of the electron density correlated with that specific nucleus.

3.7 Discussion and conclusions

In this chapter, TDDFT has been applied to calculating response properties and density fluctuations in WDM systems. By considering linear response theory, the varying degrees to which practical TDDFT calculations may describe time-dependent exchange-correlation effects were discussed, with particular regard to metals, WDM and dense plasma systems. Furthermore, the work here moves beyond the commonly used Kubo-Greenwood formula by involving a calculation of the full dielectric tensor response and a correct description of macroscopic quantities via its inverse.

Additional complexities have been noted and tackled regarding the long-wavelength limit of the response function, namely intra-band transitions and the handling of the thermodynamic limit for ionised electron states that, unlike those bound to the core, can be expected to have a continuous density of states above a certain energy.

The approach described herein and implemented within the Abinit code has, in what is both an advantage and disadvantage, that multiple tensor elements are involved in the correct treatment of LFC effects. Consequently,

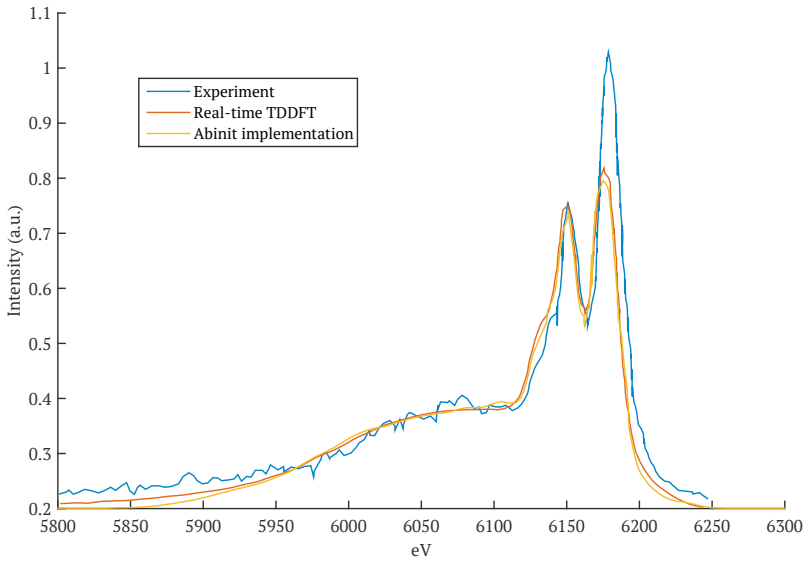

Figure 3.4: Dynamic structure factor calculations and measurements in the non-collective regime for Berylium plasma compressed to 3 times solid density. The authors' Abinit implementation is in good agreement with experiment [92] and previous, real-time TDDFT calculations [51] following convolution with the experimental source function.

the fluctuation-dissipation theorem was applied to extract equilibrium density fluctuations across multiple wavelengths. TDDFT a clear advantage in modelling the dynamic structure factor for XRTS experiments in that a calculation may be done from first principles without the usual decomposition into bound and free electrons. To establish this point, an expression for the total dynamic structure factor in terms of quantities taken from DFT MD snapshots was derived that is applicable to two temperature electron-ion systems and, in a more general form, non-equilibrium systems. Furthermore, in looking to regain the form of the Chihara expression, a natural criterion for decomposing the electronic-only response function and structure factor was found, with which an effective number of bound electrons may be defined and extracted from DFT MD simulations.

Finally, the author's modified version of the Abinit code has been applied here to calculating the dc conductivity in warm, dense Al as well as the dy-

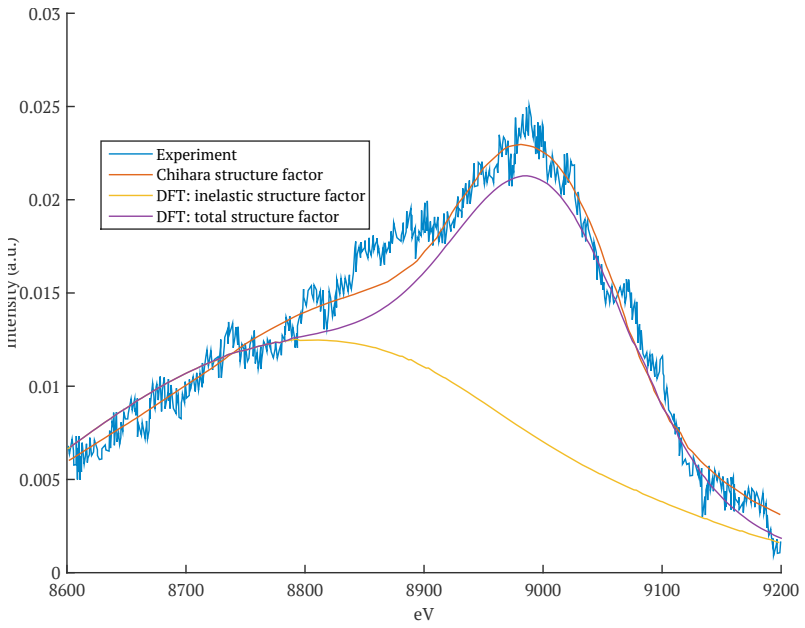

Figure 3.5: Dynamic structure factor of dense CH plasma at $k = 6.71$ for $\langle T \rangle = 110$eV, $\langle \rho \rangle = 6.74$ g cm^{-3} . The measured (blue) and predicted results using the Chihara formula (red)are plotted from reference [23] along with simulations by the author (yellow and purple).

namic structure factor for dense Be and CH plasma. Agreement between the results presented in this chapter, experiment, and theoretical predictions by other authors, supports the implementation here of a linear response code applicable to studying WDM and dense plasma conditions. In the following chapter, this will be further applied to studying the optical properties of warm, dense Al across a wide frequency range, for which the behaviour of both bound and ionised electrons must be taken into account consistently together.

4

Al free-free opacity: from room temperature to warm dense matter

4.1 Introduction

Perhaps no property of an object is more immediately apparent in our everyday life than its opacity - whether we can, in fact, *see it* or not is a question testing our fundamental understanding of the interaction of light with matter. From a practical perspective, it is central to modelling the interaction of a laser with, the transport of radiation within, and the subsequent evolution of, a system, as well as for diagnosing the conditions there-in through the interpretation of spectroscopic data. In measuring the opacity we are probing the dielectric function of the system which, following the content of the previous chapter, provides a description of a systems response properties more generally. As such, opacity investigations are a key method for constraining *ab-initio* models, together with the approximations therein, that seek to describe the complex response properties of correlated many-body systems [26, 51, 96–98].

Warm dense matter and solid density plasmas pose significant hurdles both experimental and theoretical to our understanding of opacity [99–104]. Creating and manipulating these systems under well-defined conditions of temperature and density, as well as their characterisation, is a challenging task for the experimentalist. The ubiquitous nature of light-matter interaction makes actually testing an opacity theory particularly challenging. Careful attention needs to be paid to any implicit use of models during the measurement process that may in fact conflict with the theory being tested, for example interpreting bremsstrahlung radiation as a diagnostic for the temperature of free electrons is implicitly reliant on models for the scattering time of free electrons [104]. Running this particular process backwards we can see that inverse bremsstrahlung describes the absorption of radiation by a free electron in the presence of a surrounding scattering potential [105, 106]. As such it is potentially inconsistent to, for example, use a bremsstrahlung model to diagnose temperature to be input into a *different* model for the calculation of the opacity.

The processes of brehmsstrahlung and inverse bremsstrahlung (IB) describe the emission and absorption of a photon respectively by a free charged particle, via scattering events with the surrounding system. In the plasmas environments considered here the primary mechanism for free electrons to absorb or emit photons is through scattering via ions, as illustrated in the following Feynman diagram:

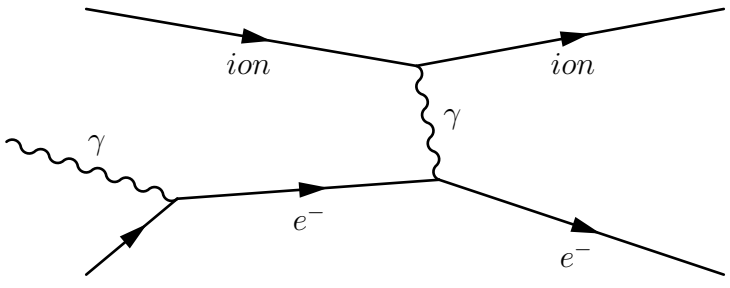

(4.1)

The ordering of photon absorption and scattering event is, of course, in-

vertible, and the time-reversed procedure describes that of bremsstrahlung emission. A quantum mechanical treatment for the absorption rate of Diag. 4.1 was provided by Ron and Tzoar [107], followed by corrections for multi-photon contributions [108], relativistic effects [109], electron degeneracy [110] and collective phenomena [111]. For the case of scattering from stationary ions one finds that the absorption coefficient α, defined as the fractional intensity loss per unit length, is given by [100]:

$$\begin{aligned}\alpha(\omega) =& \frac{ne^2}{3\pi^2 m^2 \omega^3 c} \int d^3\mathbf{p} \int_0^\infty dq\ q^4 \frac{V^2(q)}{|\epsilon(q,\omega)|^2} S(q) \\ & \left[f(E_{p-\frac{q}{2}}) - f(E_{p+\frac{q}{2}}) \right] \delta \left(\hbar\omega - \frac{\hbar^2}{m} \mathbf{p}.\mathbf{q} \right)\end{aligned} \tag{4.2}$$

The form of the above is greatly reminiscent of Fermi's golden rule: transitions occur when fluctuations in the plasma couple together two electron states at energies $E_{p-\frac{q}{2}}$ and $E_{p+\frac{q}{2}}$ where the momentum space $\int d^3\mathbf{p}$ populated uniformly by free electrons integrated over. The matrix element for the coupling is proportional to a fluctuating electric field arising from [dynamically screened] density fluctuations in the plasma. When squared this contribution becomes the last two terms on the first line of Eqn. 4.2, and the Dirac delta expresses the overall conservation of energy in the process.

If the effect of scattering is to produce only small deviations from free-electron behaviour then the system may be considered to be weakly coupled. In which case, the first-order Born approximation for scattering that Diag. 4.1 amounts to may be sufficient to describe the absorption process. Evaluating higher-order scattering diagrams would allow us to account for stronger coupling. Whilst processes like Diag. 4.1 would still feature as components of higher-order diagrams, the incoming and outgoing states of the process would no longer correspond to free-electrons, and instead be the product of multiple

'collision events' with the surrounding plasma. This can be illustrated in what for now will be a very schematic manner by replacing the electrons in Diag. 4.1 by 'dressed electrons' satisfying a Dyson equation:

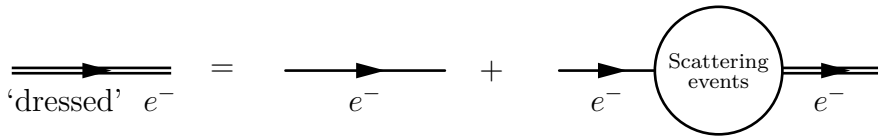

(4.3)

In which case the electron-ion scattering process in Diag. 4.1 can in fact be included amongst these scattering events, and the absorption process reduces to:

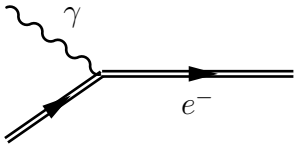

(4.4)

Note that Diag. 4.4 implies that the distribution function for incoming and outgoing states should be that of dressed particles not of free particles function as shown in Diag. 4.1 and Eqn. 4.2. With stronger electron-ion coupling it becomes increasingly non-physical to assume asymptotic free-electron states and instead we must look to describing these 'dressed' electrons consistently with the surrounding ion distribution, ultimately leading to the formation of bound and semi-bound electron-ion pairs.

Obtaining a self-consistent solution for the dressed 1-particle propagators in diagram 4.3 is, in general, a non-trivial task. The complete expression for the scattering contribution is a function of the dressed behaviour of 2-particle propagators, which are in turn found as solutions to their own Dyson equation with a scattering contribution in terms of the dressed motion of 3-particles [67, 68]. This chain of equations, referred to as the Martin-Shwinger hierarchy, extends

upwards to infinity forming a quantum mechanical analogue to the classical Bogoliubov–Born–Green–Kirkwood–Yvon (BBGKY) hierarchy of statistical physics. In practice, this is truncated by considering only a finite subset of Feynman diagrams within the scattering 'blob' of Diag. 4.3, such as only those up to a given order of e^2. Together with the rigorous mathematical machinery of Green's functions, this description of strongly interacting systems in terms of dressed n-particle states, collision events, and Dyson equations has long been widely applied to describing warm dense matter and dense plasmas [67, 68, 112–117]. The IB approach for calculating the opacity is quite a natural extension of the physical picture. IB models are certainly appealing within the 'ideal' plasma limit of high temperatures and low densities, where the separate and uncorrelated small-angle scattering of free electrons off of Debye screened (or some quasi-degenerate version thereof) ions, spatially distributed in agreement with model ion-structure factors, is the dominating absorption process. Contrast this, however, with the solid density limit. Multiple scattering between ions leads to a band structure, effective mass, and a dielectric response function possessing symmetries reflecting the quasi-periodic, strongly coupled ion distribution. The distinction between bound and free electrons becomes increasingly unclear in dense plasma conditions [118] and even in the condensed phase, the response of bound electrons is known to affect the absorption properties at free-free transition frequencies [97].

Multi-centred DFT-MD simulations have the advantage that the 'dressing' of electrons via scattering off multiple ions is accounted for to essentially infinite order (subject to periodic boundary conditions in this case) by the solution to the Kohn-Sham equation. The ion-ion structure factor is calculated and accounted for explicitly via quantum molecular dynamics within the Born-Oppenheimer approximation, providing us with an ensemble of spatial ion configurations. Projector Augmented Wave potentials introduced in chap-

ter 2 reduce the computational load of bound or semi-bound valence states in the bulk DFT calculation and allowing us to include their dynamic response on an equal computational footing with free electrons. Finally, many-body correlations and exchange interactions are computationally cheap to incorporate in the initial DFT calculation, if only approximately, via an exchange-correlation functional.

From the content of the previous chapter we now know that whilst DFT is powerful, there remain considerable issues with presently available exchange-correlation kernels when dealing with dynamic response properties such as, perhaps most crucially, the band-gap problem. It is with a certain amount of irony then, that for the next section, we move full circle back to the scattering picture fostered by the IB approach as we consider many-body theory corrections to DFT calculations using some of the available exchange-correlation functionals.

Before diving into the theoretical details of how to calculate the opacity using DFT plus many-body theory, and the potential advantages over other approaches, the experimentalist within us should note that whilst the free-free absorption process is difficult to investigate experimentally in dense plasmas the same process occurs constantly during our everyday lives in metals. As such simple metals are a valuable test-bed for electronic structure codes modelling dynamic properties of free electrons, and can generally be prepared in well-defined density and temperature conditions for experiments. The work and calculations I present in this chapter will be for solid density Al in both room temperature and warm dense matter conditions up to 15 eV. Being a simple metal with regular application as a spectral filter in the XUV range, it perhaps surprising that until recently there has been a noticeable discrepancy in the Al free-free absorption measurements between arguably the two most widely used opacity databases - those published by CXRO [123] and the

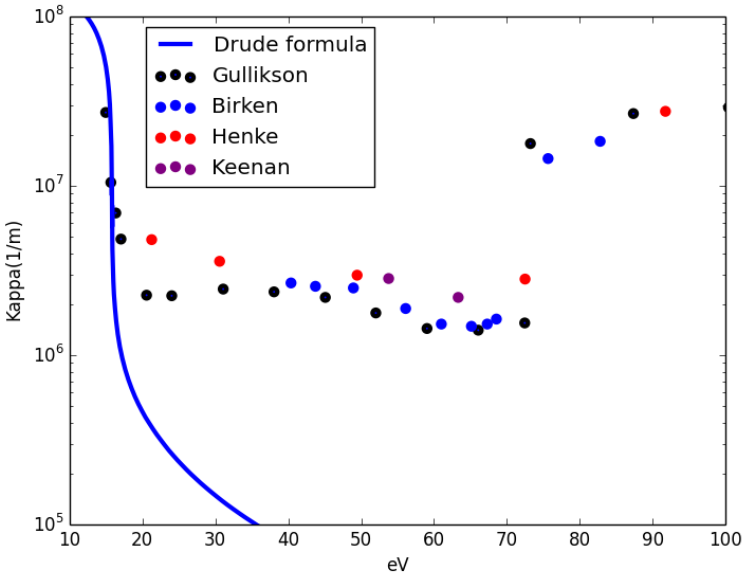

Figure 4.1: Comparison of previous experimental results by Gullikson et al. [119], Birken et al. [120], Henke et al. [121] and Keenan et al. [122] for the free-free opacity of ground state Al. Also plotted is the free-free opacity obtained using a relaxation time (Drude) model. Note that the latter completely fails to account for the absorption plateau between the plasma frequency at 15eV and the onset of L-edge absorption at 72eV.

Henke tables [121] (see Fig. 4.1. This discrepancy prompted new measurements, not performed by this author, using the Artemis laser facility [124] at the Rutherford Appleton Laboratory to measure the free-free opacity in Al (Fig. 4.2). High harmonics in the XUV range from 20 to 60 eV were generated and selected for incidence on stepped Al targets (Fig. 4.3). The use of stepped targets allowed for a clean measurement of the Al opacity through comparison of the measured transmission through targets of varying thickness. In this manner, the contribution due to oxide layers and other surface contaminants can be separately measured and accounted for as a systematic absorption contribution that we assume to be independent of target thickness.

These latest measurements will serve as the benchmark for my theoretical simulations here. As such the results of this chapter serve two purposes. First, they serve to demonstrate and provide detailed calculations for the opacity in

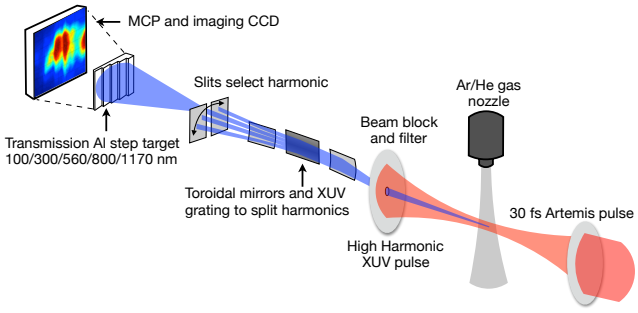

Figure 4.2: Setup for the Artemis experiment measuring free-free opacity in ground state Al, undertaken prior to the authors' DPhil (reproduced with permission from S. M. Vinko).

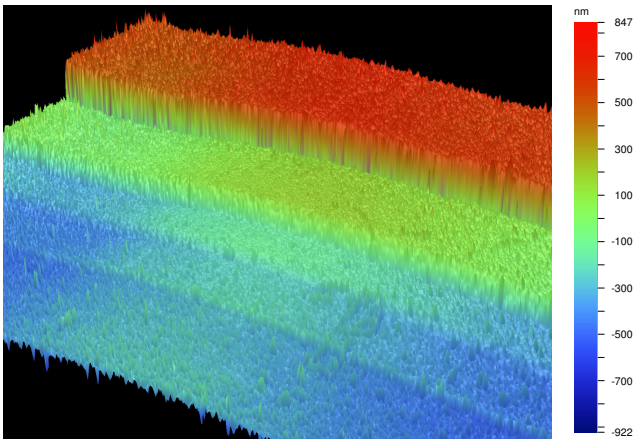

Figure 4.3: Microscopic picture of the novel step target design used in the Artemis experiment (reproduced with permission from S. M. Vinko).

WDM that are consistent with accurate absorption measurements in defined conditions. Second, as we will see they offer new insight into the opacity of ground state metals illustrating the importance of so-called local field corrections (LFC) to the dielectric function and quasi-particle corrections to bound state energies. These corrections will be shown to be necessary to reproduce the Artemis results, previous work on Al that aimed to reproduce the CXRO database in the cold limit may have provided a misleading impression that detailed multi-centred DFT calculations including LFC and quasi-particle corrections such as the ones presented here were not necessary to describe the opacity in ground state metals.

It is in within this context that I present in this chapter the opacity of solid

density Al from the ground state through to WDM conditions modelled from first principles using a combined DFT plus many-body theory approach.

4.2 Self-energy G_0W_0 corrections

Just as actual DFT exchange-correlation functionals hinge on approximating the complex, quantum mechanical, processes in many-body systems by comparison to simpler cases (such as the uniform electron gas); practical many-body theory calculations require their own approximations in order to truncate the previously mentioned Martin-Shwinger hierarchy of equations describing correlations between increasing numbers of particles within a statistical system.[1] Within condensed matter physics it is the GW approximation, discussed in more detail later, that is the typical go-to approximation for correcting DFT band-gap energies. These many-body approaches replace the DFT exchange-correlation functional with an equivalent self-energy term Σ analogous to the scattering event 'blob' of Diag. 4.3 that arises in the context of IB calculations. Whether the DFT calculation is used as a seed for a self-consistent many-body calculation or the latter is treated as a first-order correction to DFT is indicated by appropriate subscripts. For example, the calculations of this chapter are of the G_0W_0 variety where the subscripts indicate that the DFT-calculated (i.e. zeroth order in our corrections) single-particle Greens function G and screened Coulomb potential, to be introduced later, W is used to compute the many-body self-energy.

Advanced numerical schemes implementing the DFT + G_0W_0 approach are already available and have been widely applied to condensed matter systems. On the other hand, very few DFT + G_0W_0 have been performed using

[1] As an aside, this hierarchy can also be expressed in terms of a single, closed functional-differential equation for the 1-particle Green function [68], though this is not particularly useful for the calculations in this thesis.

finite temperature many-body theory [125], as a result, it has been necessary for the author to implement such a capability within a plane-wave DFT code for which Abinit [47] was chosen. Many-body theory has however been extensively applied to describe both the equilibrium and non-equilibrium evolution of finite-temperature interacting systems, including under WDM conditions. The key object we require is the Kadanoff-Baym contour, also referred to as the extended Keldysh contour, as shown in Fig. 4.4. This allows for an elegant expression of the time-dependent expectation value of an operator $\hat{O}(t)$ in terms of the complex time evolution operator: $\hat{U}(t,t')$:

$$\begin{aligned} O(t_1) &= \mathrm{Tr}\left[\hat{\rho}(t_1)\hat{O}\right] \\ &= \mathrm{Tr}\left[\hat{\rho}(t_0)\ \hat{U}(t_1,t_0)\ \hat{O}\ \hat{U}(t_0,t_1)\right] \end{aligned} \tag{4.5}$$

Where t_1 is after t_0 such that $\hat{U}(t_0,t_1)$ and $\hat{U}(t_1,t_0)$ evolve a ket forwards and backwards in time respectively. As per the usual in Green's function based quantum mechanics, it is convenient to extend the time evolution operators to complex arguments; the forward operator being analytically continuable to the upper half plane and the backwards operator to the lower half. Adding an infinitesimal imaginary component to these operators the expectation value of $\hat{O}(t)$ becomes:

$$\begin{aligned} O(t_1) &= \mathrm{Tr}\ \left[\rho(t_0)\ \hat{U}(t_1-i0,t_0-i0)\ \hat{O}\ \hat{U}(t_0+i0,t_1+i0)\right] \\ &= \frac{1}{Z(\beta)}\mathrm{Tr}\ \left[\hat{U}(t_0-i\beta,t_0)\ \hat{U}(t_1-i0,t_0-i0)\ \hat{O}\ \hat{U}(t_0+i0,t_1+i0)\right] \end{aligned} \tag{4.6}$$

Where in the final line, the density matrix at t_0 has been assumed to be that of thermal equilibrium at a temperature $T = 1/(\beta k_B)$ thereby possessing the partition function $Z(\beta)$. Defining a Kadanoff-Baym contour ordering operator T_{KB} we then have:

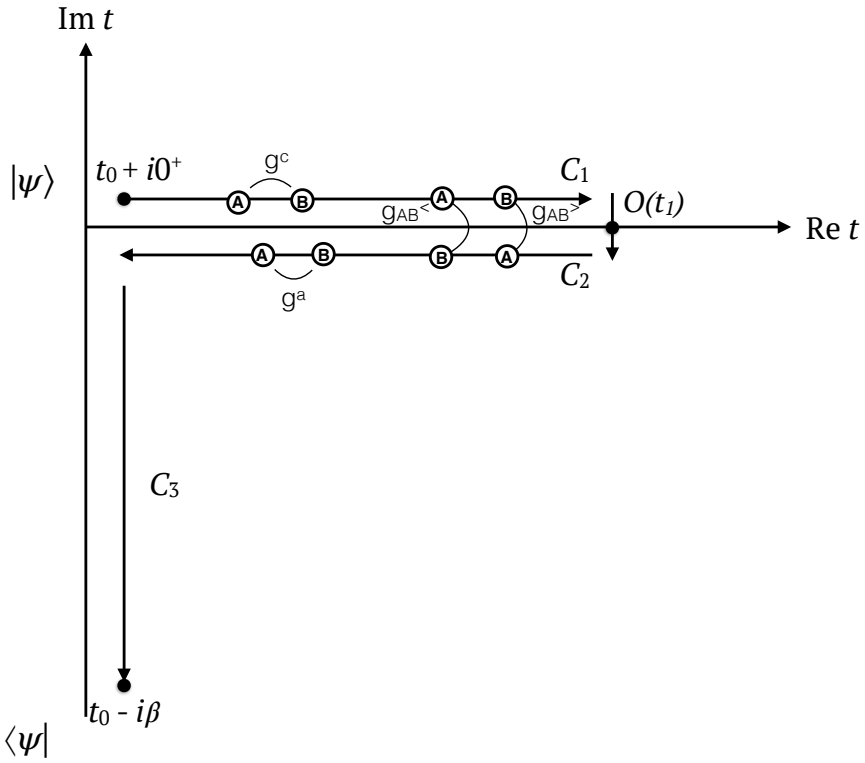

Figure 4.4: Contour illustrating the time evolution of the wavefunction in equation 4.7. Branches C_1 and C_2 describe causal and anti-causal evolution, or alternatively can be viewed as the evolution of the ket and bra respectively from time t_0 to t_1. Branch C_3 provides the initial thermal ensemble of states at t_0. Under equilibrium starting conditions and for system Hamiltonians that are not explicitly time-dependent, i.e. the conditions relevant to this work, both $g^>$ and $g^<$ are related via detailed balance considerations.

$$O(t_1) = \frac{1}{Z(\beta)} \mathrm{Tr}\ T_{KB} \left[\hat{U}(t_0 - i\beta, t_0) \hat{O}(t_1) \right] \tag{4.7}$$

In a similar manner we may express the single particle Kadanoff-Baym Greens function as:

$$G(r_1, t_1; r_2, t_2) = \frac{1}{Z(\beta)} \mathrm{Tr}\ T_{KB} \left[\hat{U}(t_0 - i\beta, t_0) \hat{\psi}^\dagger(r_2, t_2) \hat{\psi}(r_1, t_1) \right] \tag{4.8}$$

Note that for real times the single particle Green's function, as well as n-point correlation functions in general, will differ in their analytic behaviour and

physical interpretation depending on the precise ordering along the Kadanoff-Baym contour as shown in Fig. 4.4. For real times, 4 different Green's functions can be defined:

$$\begin{aligned} G_c &= \frac{1}{Z}\mathrm{Tr}\ e^{-\beta H_0} T_c \left[S(t_0 - i\beta, t_0)\hat{\psi}_+\hat{\psi}_+ \right] \\ G_{\bar{c}} &= \frac{1}{Z}\mathrm{Tr}\ e^{-\beta H_0} T_c \left[S(t_0 - i\beta, t_0)\hat{\psi}_-\hat{\psi}_- \right] \\ G_< &= \frac{1}{Z}\mathrm{Tr}\ e^{-\beta H_0} T_c \left[S(t_0 - i\beta, t_0)\hat{\psi}_+\hat{\psi}_- \right] \\ G_> &= \frac{1}{Z}\mathrm{Tr}\ e^{-\beta H_0} T_c \left[S(t_0 - i\beta, t_0)\hat{\psi}_-\hat{\psi}_+ \right] \end{aligned} \tag{4.9}$$

The utility of Fig. 4.4 and Eqn. 4.9 is their combined ability to express time ordered, retarded and advanced Green's functions in a manner suitable for perturbation theory.

The above expressions are quite general and suitable for describing the evolution of a system in thermal equilibrium at t_0. At this point, we look for a means to perturbatively expand the time evolution operator in terms of the non-Hartree electron-electron interaction that is responsible for the exchange-correlation term in DFT. Unfortunately, the partition function in the denominator complicates the calculation unless we are prepared to calculate a quotient of Feynman diagrams. There are two ways around this problem. One is to introduce the electron-electron interaction adiabatically and set $t_0 \to -\infty$, the initial partition function can then be taken as that for the non-interacting system.[2] The other is to calculate correlation functions for points t_1 and t_2 along the imaginary time contour C_3 following Matsubara's method, and then to analytically continue the result to the real axis. In this chapter, I have followed the latter approach which avoids directly dealing with the various Green

[2]The more general case of a non-adiabatic perturbation is dealt with using the full Kadanoff-Baym equations and their extension to the inclusion of initial correlations by Semkat et al [126].

function orderings shown in Fig. 4.4 and their complex analytic behaviours.

The intention is to use DFT Kohn-Sham eigenstates to build a starting Green's function $G_0(\mathbf{x}, \mathbf{x'}; \epsilon)$, we then turn to many-body theory to provide us with some approximate expression for $\Sigma(\mathbf{x}, \mathbf{x''}; \epsilon)$ in terms of $G_0(\mathbf{x}, \mathbf{x'}; \epsilon)$ and solve for the new Green's function $G_1(\mathbf{x}, \mathbf{x'}; \epsilon)$. This procedure can then be iterated to self consistency determine to correct interaction Green's function $G(\mathbf{x}, \mathbf{x'}; \epsilon)$.

Formally speaking the exact expression for $\Sigma(\mathbf{x}, \mathbf{x''}; \epsilon)$ is coupled to the 3-point Green's function, and so on ad-infinitum leading to a hierarchy of equations analogous to the classical BBGKY hierarchy. In practice we curtail this chain of equations by proposing an approximate equation for the motion for an n-point function, or alternatively restricting the the Coulomb interaction to finite order of e^2. In this thesis I will be working within the so-called DFT + G_0W_0 approximation:

$$\Sigma(\mathbf{r}, t; \mathbf{r'}, t') \approx iG_0(\mathbf{r}, t; \mathbf{r'}, t')W_0(\mathbf{r}, t; \mathbf{r'}, t'). \tag{4.10}$$

$$W_0(\mathbf{r}, t; \mathbf{r'}, t') = \epsilon^{-1}(\mathbf{r}, t; \mathbf{r'}, t')V_C(\mathbf{r} - \mathbf{r'}). \tag{4.11}$$

Where W is a dynamically screened Coulomb potential.

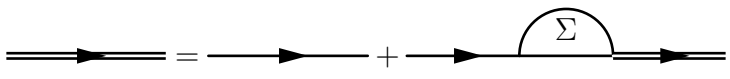

(4.12)

In addition, this will be a non-self consistent approximation. The screened Coulomb interaction W_0 is to be taken from an initial TDDFT calculation and used to calculate the interacting Green's function $G(\mathbf{x}, \mathbf{x'}; \epsilon)$, but we do not follow up with additional iterative calculations of W, Σ and G.

Physically we may interpret this with the aid of the Feynman diagrams shown in Fig. 4.5. The self-energy term describes the dynamic potential felt

by an electron moving from point to point, as due to the plasma response to said motion. Additionally, the electron experiences the potential due to static and dynamic charge density correlations in the plasma as a correction to the mean-field Hartree approximation.

The importance of vertex corrections to the self-energy operator will not be investigated in this thesis, in part due to the computational expense of solving the Bethe-Salpeter equation and limited ability of current exchange-correlation kernels to accurately account for electron-hole interaction. Fortunately, the G_0W_0 approximation already provides a very good prediction for energy gaps in condensed matter systems compared to Kohn-Sham eigenvalues. Vertex corrections using the LDA exchange-correlation kernel do not generally provide much better results than G_0W_0 calculations, whilst in the warm dense matter regime multiple recent studies have found either the RPA or LDA kernel provides calculations for the dielectric function in good agreement with experimental results - band gap problems notwithstanding.

The advantages of fully self-consistent calculation in the absence of vertex corrections have been discussed and criticised at length in the condensed matter regime [54]. Regardless, G_0W_0 already provides a substantial improvement over the Kohn-Sham eigenvalues and it should be stressed that for the purpose of this work we are interested in correcting binding energies differing by up to 10 eV from their experimental values. At the time of writing, very few finite temperature DFT + GW calculations have been published at any level of approximation. The effects of quasi-particle self-consistency, as well as vertex corrections, are of course topics worthy of further study and consideration in warm dense matter systems. However, the several orders of magnitude more precise sub-eV G_0W_0 calculations commonplace with condensed matter systems are perhaps overkill in a regime where density/temperature gradients, breakdowns of the Born-Oppenheimer approximation, and non-equilibrium

conditions are all possibilities as well.

When calculating the self energy it is convenient to separate contributions due to exchange and correlation: $\Sigma = \Sigma^X + \Sigma^C$. Where Σ^X is the finite temperature exchange energy term. For single shot G_0W_0 corrections we only require the diagonal elements of the self energy. In the Matusbara formalism we can express $\Sigma^C(z)$ for points $z = (2n+1)\pi i$ along the imaginary axis in terms of the dielectric function at frequencies $\omega_m = 2m\pi i$ [68]:

$$\Sigma^C_{nn}(i\nu_{n'}) = \frac{iT}{2\pi} \sum_{GG',m,i\omega_n} \frac{[M^{mn}_G(\mathbf{k})]^* M^{mn}_{G'}(\mathbf{k}) W^C_{GG'}(\omega)}{i\nu_{n'} + i\omega_n - \epsilon^{KS}_m(\mathbf{k})}, \tag{4.13}$$

where the Kohn-Sham matrix elements are $M^{mn}_G = \left\langle \psi^{KS}_m(\mathbf{k}) \middle| e^{iGr} \middle| \psi^{KS}_n(\mathbf{k}) \right\rangle$, the screened Coulomb interaction is given by $W^C_{GG'}(\omega) = (\epsilon^{-1}_{GG'}(\omega) - 1)V^C_{GG'}$, and where we have set the chemical potential $\mu = 0$ for convenience. The retarded self-energy $\Sigma(\omega + i0^+)$ is then obtained by analytical continuation from the upper-half plane to the real axis as shown in Fig. 4.5. Here, this is achieved numerically by fitting to a Padé approximant. In condensed matter systems this method of numerical analytic continuation is normally considered to be a less accurate, but quicker, alternative to the contour deformation method [127]. We find it to be sufficient for its primary purpose here, that of correcting the position of the L-edge.

4.3 Results

The ab-initio calculations for each regime consist of three steps. First, a multi-centred Kohn-Sham DFT [5, 6, 27] simulation is performed using Projector Augmented Wave (PAW) [53, 129] pseudopotentials with 1s electrons frozen in the core. Up to 1500 bands are calculated in 32 atom unit cells with a $2 \times 2 \times 2$ k-point grid Brillouin zone sampling and a plane-wave cutoff of

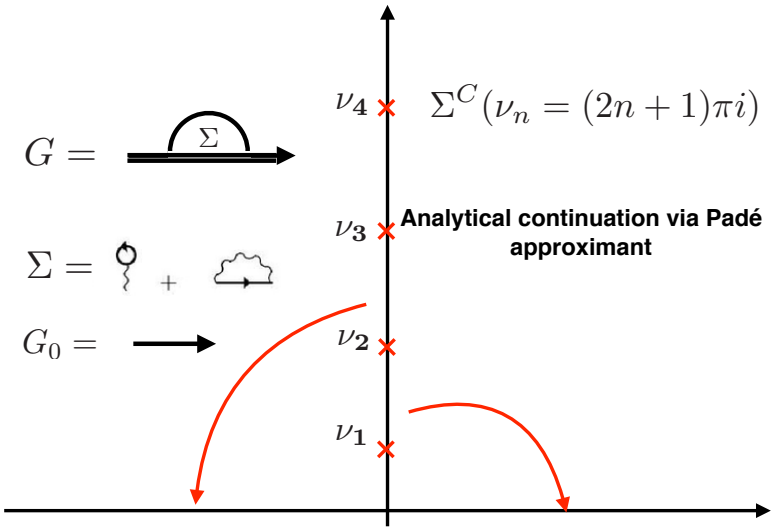

Figure 4.5: Illustrative diagram for the method used to calculate G_0W_0 corrections to the Kohn-Sham eigenvalues. Diagrams for the self energy Σ are shown in terms of the Kohn-Sham Green's function G_0. The corrected energy eigenvalues are obtained by considering the spectral function $A(\omega)$ (see Fig. 4.6), for which the self energy (Eqn. 4.13) is first analytically continued from the fermionic Matusbara frequencies ν_n to the real axis using a Padé approximant.

400 eV. An ensemble of ion positions is obtained by evolving the system in time for 3 ps in the Born-Oppenheimer approximation whilst coupled to a Nosé-Hoover thermostat. Second, Time-Dependent DFT (TDDFT) [71, 90] is used to calculate the first-order density response function within the RPA, and thus the dielectric function of the system [41] for selected ion spatial configurations from the last 1 ps of evolution. Finally, the calculated dielectric function is used to compute the first order, finite temperature G_0W_0 corrections to the Kohn-Sham energy levels for bound L-shell states and low lying continuum states, thereby addressing the infamous band-gap problem [54]. Here, this step corrects the position of the L-edge. The G_0W_0 corrected quasi-particle energies are then used to compute the final dielectric function. Whilst GW is frequently used in the ground state to correct band gaps to sub-eV accuracy, a detailed study of finite temperature many-body effects on the structure within

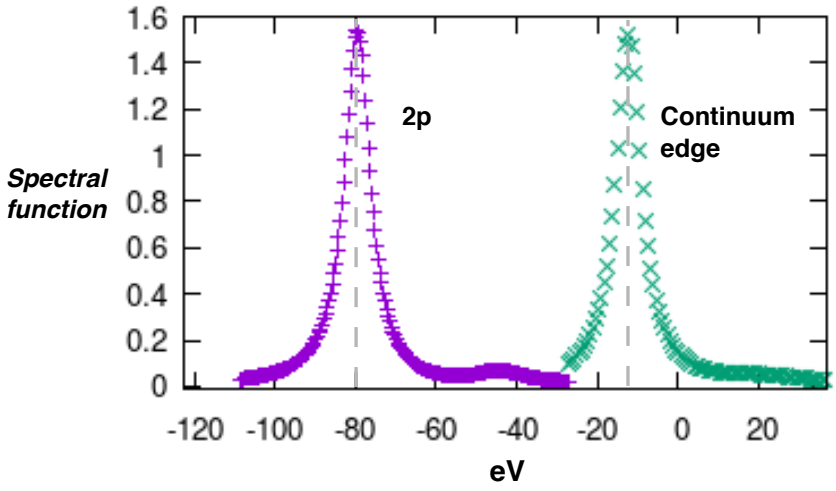

Figure 4.6: Plot showing contributions to the $T = 15$ eV spectral function from L-shell and lowest energy continuum state. By fitting the main peaks to a Lorentzian both the energy and lifetime of each quasi-particle may in principle be calculated. However, the suitability of both the Padé approximant [128] and the GW approximation itself [117] to accurately describe complex satellite features in the spectral function has been questioned. With this in mind, and given that it is primarily the eigenvalues rather than lifetimes of quasi-particles that G_0W_0 approximation has been successfully applied to, only the energy corresponding to the peaks of the spectral functions is used.

the continuum is beyond the scope of this thesis.

In Fig. 4.7 the calculated opacity for cold Aluminium is plotted alongside previous theoretical calculations, whilst in Fig. 4.8 the calculated opacity is compared to the Artemis data and past experimental results [119–122]. Ab initio calculations agree reasonably well with the Artemis data as well as being consistent with measurements by Henke et al. and Birken et al. The contribution of both LFC and GW corrections are significant at frequencies above the plasma frequency. LFC increases the opacity in the intermediate region (15 eV $< \omega <$ L-edge) whilst decreasing absorption above the L-edge. Notably, the Cooper minimum feature present in both the Gullikson data and average-atom simulations [103] at $\omega \approx 20$ eV does not appear in these calculations or the supporting experimental data. It should be noted that experimental error bars were not quoted alongside the measurements of Henke

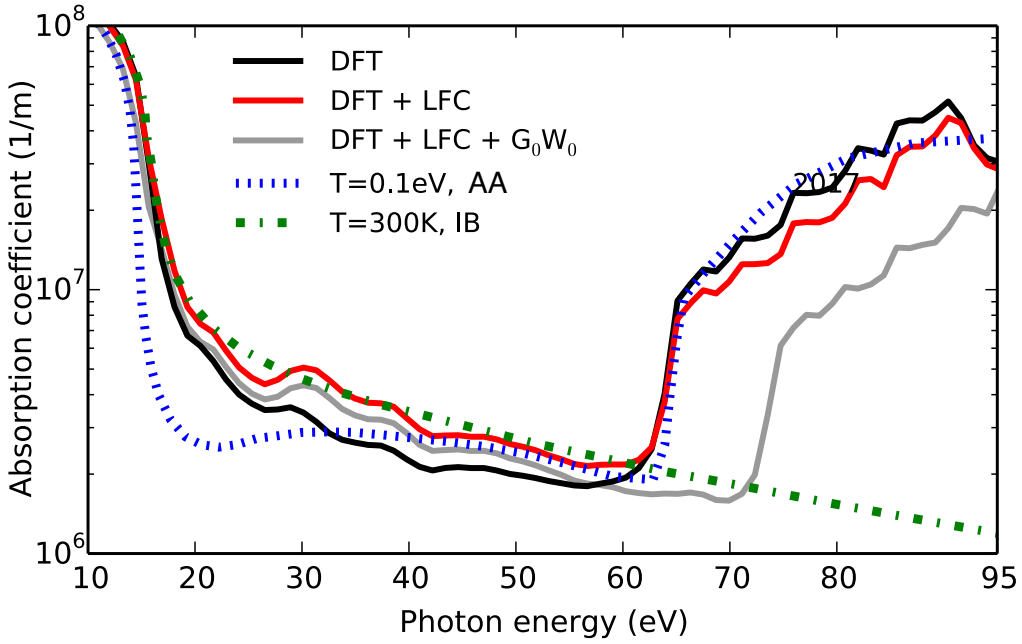

Figure 4.7: Opacity for room temperature Al calculated using DFT at different levels of approximation, as compared to the low temperature limit of previous average-atom simulations [103] and IB models [100].

et al., Gullikson et al., or Birken et al. and so the extent of deviation for these data sets from our model cannot be absolutely determined.

Above the L-edge, the ab initio calculations appear to underestimate the opacity by about a factor of 2. The exact reason for this is not immediately clear, though it appears to be a consequence of the G_0W_0 corrections. Whether this discrepancy is removed following self-consistent quasiparticle calculations or with the inclusion of electron-hole interactions is beyond the scope of this work. In the free-free regime the inclusion of LFC and applying G_0W_0 corrections are necessary to reproduce the experimental data, the influence of both of which is shown in Fig. 4.8 b. The importance of including both of these effects should not be underestimated as indeed the neglect of these actually leads our model to (presumably coincidentally) better fit the Gullikson et al. data. Here lies find a clear warning for the consequences of approximations made on

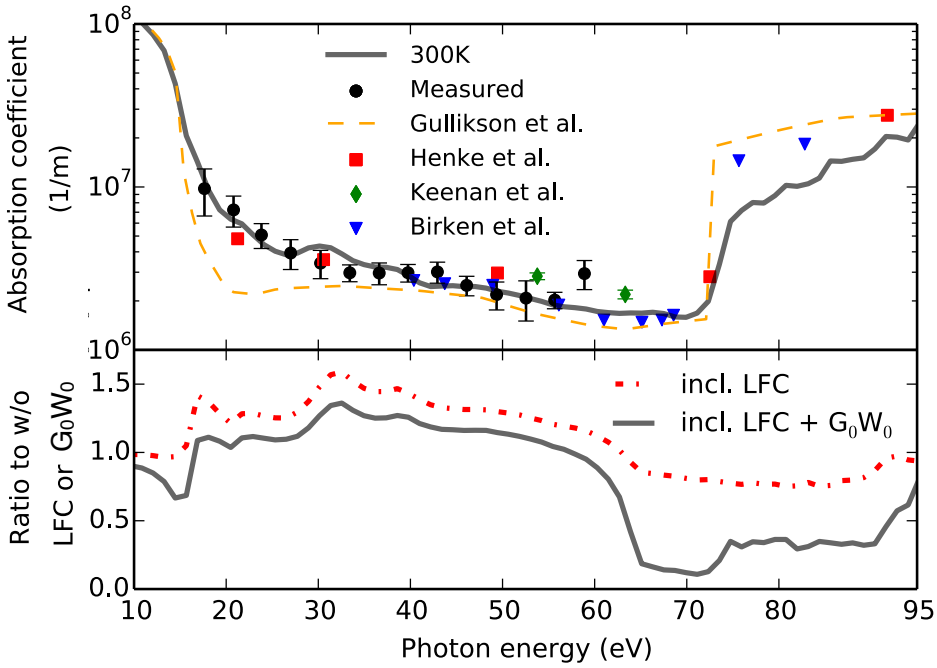

Figure 4.8: Opacity for room temperature Al compared to the new Artemis measurements and previously published experimental results. The inclusion of LFC and G_0W_0 corrections (also see Fig. 4.7) brings our calculations closer in line with both the Artemis data and the measurements of Henke et al. [121]

premature conclusions of the accuracy of both models and measurements. As a result whilst the model thus far appears to match the latest free-free opacity measurements favourably, future work should include self-consistent quasiparticle calculations as well as the inclusion of exciton effects - the influence of both of which may turn out to be important.

In Fig. 4.9 the calculations are extended into the warm dense matter regime, showing the predicted opacity for equilibrium, solid density Al at T =1, 5, 10 and 15 eV. In moving from room temperature to T = 1 eV the free-free opacity increases considerably. This is in contrast to previous average-atom [103] and IB calculations [100], as shown in Fig. 4.10 and 4.11 respectively. In addition, the recently published (at the time of writing) measurements by Kettle et al. [102] are included. For the latter, experimental conditions were estimated to be $T_e \approx 1$ eV based on their modelling, how-

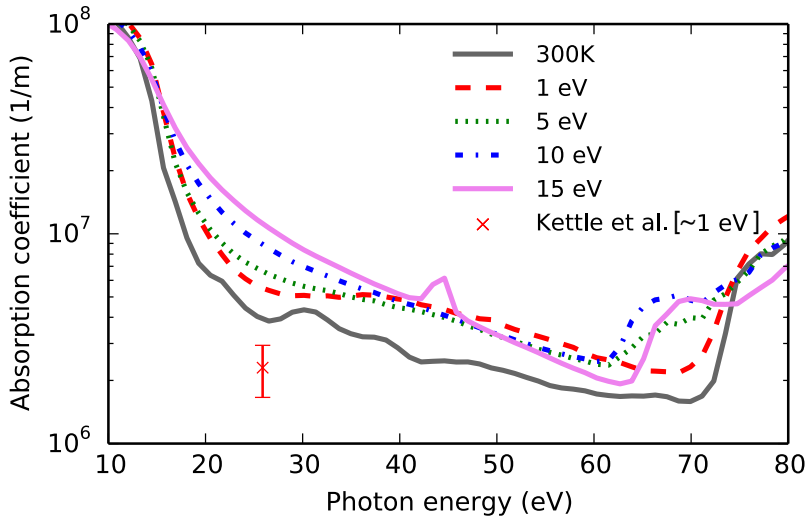

Figure 4.9: Calculated opacity for equilibrated warm dense Al up to $T = 15$ eV along with the single data point of Kettle et al. [102]. The free-free opacity increases considerably upon melting in part due to LFC for the $T = 1$ eV case.

ever a separate experimental determination was not available. Kettle et al. observed no significant change in opacity compared to ambient conditions, though it should be noted that their cold measurements do differ significantly from both the simulation and Artemis measurements presented here.

Calculations performed using room temperature ion configurations, but with the electrons heated to 1eV, suggest a breakdown of the lattice structure to be responsible for the sudden increase in free-free absorption at $T = 1$ eV. This may explain why such an increase was not predicted by the previous IB theory (in which the role of ion-ion correlations was only estimated) or average-atom calculations. A key difference between the latter and the author's calculations is the use here of periodic supercells; well suited to representing the periodic Al fcc lattice in the cold limit, and capable of dealing with non-spherically symmetric ion distributions. The discrepancies between these three models suggest the ion distribution, boundary conditions and symmetries of the system may have a significant impact on the absorption in WDM

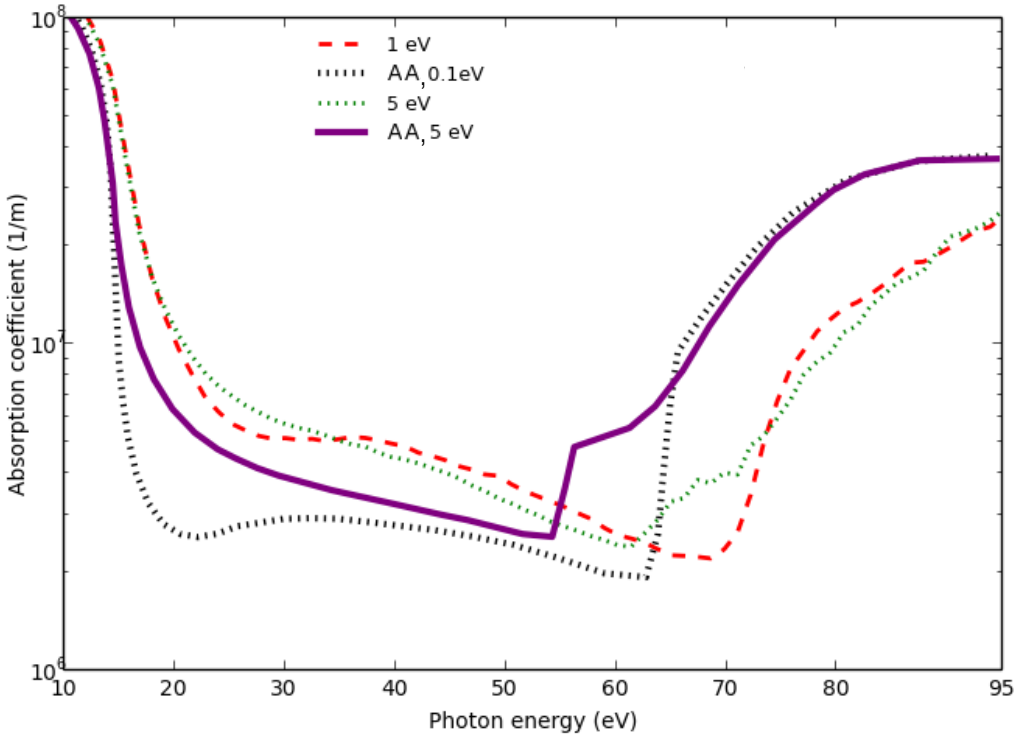

Figure 4.10: Comparison of the calculated opacity for warm dense Al with the average-atom (AA) calculations of Shaffer et al. [103]. Note that the calculations of reference [103] do not predict any substantial changes in the opacity until a temperature of 5 eV is reached, with the opacity at $T = 1$ eV essentially unchanged from that of $T = 0.1$ eV.

at low temperatures.

For $\omega < 35$ eV the temperature dependence of the opacity is consistent with plasmon broadening. For $35 < \omega < 60$ eV only a relatively weak temperature dependence is predicted with the exception of the 2s-2p resonance ($\omega \approx 42$ eV) owing to thermal ionisation of the L shell at the highest temperatures. Closer to the L-edge, significant pre-edge features develop as low lying continuum states are thermally depopulated. This should be distinguished from changes in the continuum lowering which remains relatively constant - only changing by ≈ 4 eV for the highest temperature of $T = 15$ eV.

Large-scale DFT, and in particular G_0W_0, calculations are expensive, especially at higher temperatures. As such, there is a clear incentive to establish in what conditions simpler models, such as IB calculations, may be safely used.

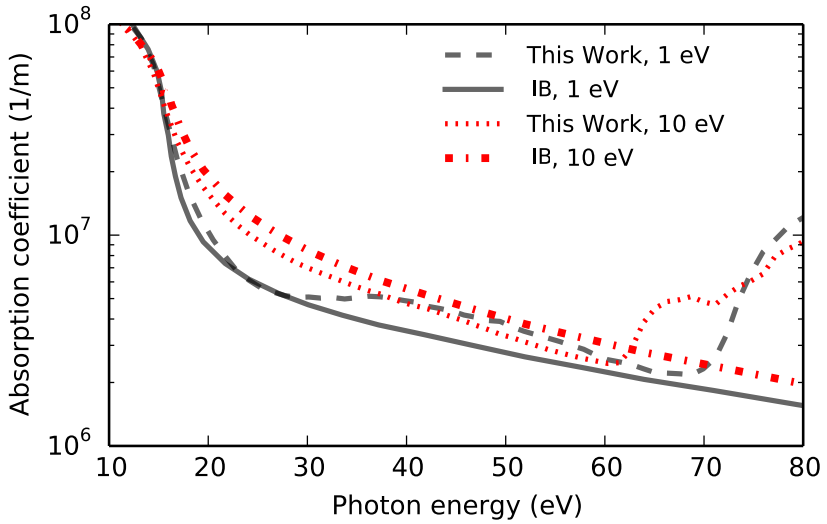

Figure 4.11: Comparison of our calculated opacity with the Inverse Bremsstrahlung (IB) model of reference [100] at high temperatures. Our results appear to be approaching the general form of the IB model, and match it particularly well below the 2s-2p resonant transition.

In Fig. 4.11 we plot our finite temperature calculations along with the IB model of [100]. The latter used a frozen core pseudopotential and therefore cannot be expected to replicate the 2s-2p bound-bound transition or L-edge features present in the work here. Nonetheless, the IB calculations closely agree with the results for $\omega < 25$ eV at $T = 1$ eV where the opacity is dominated by the plasmon feature, and at higher temperatures our calculations do indeed appear to be approaching an IB like opacity - particularly below the 2s-2p feature. Incidentally, in that frequency range the results for $T = 15$ eV very closely follow the IB opacity for $T = 10$ eV.

4.4 Conclusions

This chapter presents calculations for the opacity in Al from the plasma frequency up to the L-edge, under conditions of solid density and temperatures from room temperature up to $T = 15$ eV. Room temperature calculations indi-

cate significantly higher free-free opacity than the measurements of Gullikson et al. [119] used in the CXRO database [123], but remain consistent with the results of references [121, 122] and unpublished measurements at the Artemis facility. The simulations presented here are unique in that they combine DFT with finite-temperature many-body theory calculations under WDM conditions, exhibiting clear deviation from previous average-atom and IB models at finite temperatures. The influence of LFC and corrections to the L shell binding energy on the resulting opacity has been shown with both having significant effects, especially at lower temperatures. The author has implemented a finite-temperature G_0W_0 code within Abinit, with the potential to model continuum lowering effects in WDM and dense plasma conditions from first principles. Whilst changes in continuum lowering for the relatively low temperatures and charge states considered here are expected to be small, the fact that we nonetheless appear to be obtaining sensible L-edge positions bodes well for potential future applications of finite temperature G_0W_0 in dense plasmas.

5

Conclusions and future work

Within this thesis, I have described how and why DFT can be used to guide our understanding of the properties of warm dense matter and dense plasma. The advantage of DFT lies is its ability to reduce the complex behaviour of an interacting many-body wavefunction to a description of the density, and possibly current, alone. For these reasons, both Kohn-Sham and orbital-free density functional theory are now widely applied to study dense plasmas and warm dense matter conditions. However, the complete application of DFT in its time-dependent form has recently seen rapid growth in the field of warm dense matter and dense plasmas. In this thesis, I have therefore sought to explore and inform on how DFT techniques might be tailored for specific application to warm dense matter systems.

Chapters two to four of this thesis may loosely be associated with the study of bound electrons, free electrons, and unified treatment of both. Specifically, whilst DFT contains no a priori distinction between bound and free electrons, nor does such a distinction have any bearing on the immediate goal of obtaining the correct mean electron density, each of the three main chapter topics find their most obvious application in dealing with properties of the corresponding sub-population of states in the system. Here I will briefly summarise each

chapter in this context and provide discussion for future research directions.

In chapter 2, the merits of excited core pseudopotentials as a method of explicitly modelling the distribution of ion charge states in plasma was discussed. Standard finite temperature, all-electron DFT calculations do not provide easy access to properties arising from individual charge state configurations - although the Hohenberg-Kohn theorems establish the information is there.

The nature of Kohn-Sham orbitals makes imposing arbitrary occupation numbers as a means to enforce a given charge state distribution, to be of unclear immediate physical meaning. However, in chapter 2 I have taken steps to justify the excited frozen-core pseudopotentials as a way to obtain meaningful results for arbitrary occupation numbers. This was done first by establishing that the frozen-core approximation continues to hold for thermally excited core states by comparing the resulting density of states with those from an all-electron calculation. Second, it was argued from a many-body theory that the interaction between core and valence states is sufficiently well described through the Hartree interaction, along with wavefunction orthogonality, alone. Following this line of thought, we can then decompose our treatment of exchange-correlation effects to the core and valence electron systems separately. This would mean that a self-consistent combined treatment of the two systems, which need not be in equilibrium with each other but at this point in the argument must separately be in equilibrium if we are to use DFT to describe both, is determined via their mutual Hartree interaction and orthogonality conditions.

The density of states comparison demonstrates core-valence exchange-correlation interactions to be negligible for thermal occupations, and the linear nature of the Hartree interaction with respect to occupation number suggests, but does not prove, this also holds when the core and valence systems are not in equi-

librium. The final step towards arguing for arbitrary, non-equilibrium core configurations comes via the success the delta self-consistent field method has had in describing excitations in finite size systems, of which the frozen ion core is an example of, using equilibrium DFT exchange-correlation functionals.

Excited PAW potentials offer a computationally simple method to study how the presence of a full distribution of ion charge states impacts physical properties when a clear distinction between core and valence states can be made. In allowing one to explicitly model the distribution of charge, excited PAW potentials can aid us in examining what role the local micro-field plays in influencing measurements, such as spectral lines and ionisation energies, that probe a plasma system on the length scale of individual ions and their immediate surroundings. Furthermore, being able to explicitly model charge distributions also opens up a means to study how microscopic charge state disorder couples to macroscopic transport properties. There exists extensive research regarding the localisation of wavefunctions and the occurrence metal-to-insulator Anderson phase transitions within disordered condensed matter systems. Using excited core potentials, we can address whether similar phenomena can occur driven by on-site charge state disorder in XFEL or laser-produced plasmas, and on an ultrafast timescale before significant ion motion leads to additional, structural disorder by breaking lattice symmetry.

In chapter 3, time-dependent DFT was extensively discussed as a means to obtain general response properties of plasmas and metals. Unlike bound states, free electrons exhibit complex collective behaviour in addition to single-particle excitations. As such, generating excited configurations by simply imposing occupation numbers in the manner of excited pseudopotential construction is of less immediate physical meaning. The extension of DFT to time-dependent linear response theory allows for physical quantities such as excitation energies and density fluctuations to be calculated without assigning a physical meaning

to the Kohn-Sham states themselves, allowing for direct access to the dynamic properties of strongly correlated electron systems. By applying the Langreth rules in conjunction with the fluctuation-dissipation theorem and standard linear response theory manipulation, an expression for the electron-density dynamic structure factor was derived including contributions from both electronic and nuclei motion. In particular, the tensor nature of both response functions and structure factors was seen to be important in producing the Chihara decomposition. The work of this section suggests a decomposition into homogenous and inhomogeneous terms may aid in separating the contributions from electronic and nuclei motion respectively.

From a technical point of view, special attention was paid to the handling of the continuum limit when modelling free-electron like systems using a finite number of states. The common methodology of inserting DFT states into the Kubo-Greenwood formula along with replacing a Dirac delta pole with a finite width Gaussian was discussed and critiqued. In chapter 3, I have presented results that move beyond some of these approximations, accounting for local field corrections to macroscopic properties and handling the continuum limit using a method that avoids artificial structure arising from the wings of Gaussian or Lorentzian functions. Technical details regarding the interband and intraband contributions have been explained, together with the associated consequences for the plasma frequency, and a method of extrapolating to the correct plasma frequency using the Bohm-Gross formula is also suggested.

In chapter 4 the free-free opacity in ground-state and warm, solid density, Al was modelled by combining the response function formalism of chapter 3 with a Green's function many-body theory treatment of exchange-correlation effects. The latter provides an ab-initio means with which to correct the well-known band-gap problem in DFT using the finite temperature G_0W_0 approximation for the self-energy. Such a calculation, whilst commonplace in

the ground-state condensed matter limit, has not previously been applied to correcting DFT results in warm dense matter conditions and the work of this chapter represents a significant contribution to the theoretical prediction of bound-state energies in dense plasmas and under warm dense matter conditions. Consequently, it was necessary to write and implement a finite temperature many-body theory code within the Abinit DFT code, a version of which will in the future be made available to other Abinit users.

Future work may concern either alternative computational approaches to the Padé method and/or approximations to the self-energy beyond the GW approximation. The author's many-body theory code has been sufficient for calculating continuum lowering effects in the cold limit and in WDM condition, however, the description of the spectral function in general such as satellite states and finite-lifetimes remains incomplete. Though DFT+G_0W_0 calculations will likely remain computationally expensive, calculations for a single ion situated with suitable periodic boundary conditions may prove useful for simulating solid density, XFEL produced plasmas probed over timescales too short for significant ion motion to take place.

The theoretical results of chapter 4 were compared favourably to experimental measurements of the free-free opacity in ground state Aluminium conducted using the Artemis facility at the Rutherford Appleton Lab. Crucially both bound state behaviour, via many-body corrections to the binding energy, and a proper account of the tensor nature of free-free linear response properties, via local field corrections, had a significant impact on the calculations at lower temperatures. A short paper describing the experimental and theoretical details is available on arxiv, with a more in-depth and extended manuscript having been accepted to a peer-reviewed journal, and will be published in due course.

Bibliography

[1] Freeman J. Dyson. Ground-state energy of a finite system of charged particles. *Journal of Mathematical Physics*, 8(8):1538–1545, 1967.

[2] B. J. B. Crowley. Continuum lowering - A new perspective. *High Energy Density Physics*, 13(1):84–102, 2014.

[3] Thomas R. Preston, Sam M. Vinko, Orlando Ciricosta, Hyun-Kyung Chung, Richard W. Lee, and Justin S. Wark. The effects of ionization potential depression on the spectra emitted by hot dense aluminium plasmas. *High Energy Density Physics*, 9(2):258–263, jun 2013.

[4] M. W. C. Dharmawardana. A Review of Studies on Strongly-Coupled Coulomb Systems Since the Rise of DFT and SCCS-1977. *Contributions to Plasma Physics*, 55(2-3):85–101, 2015.

[5] P. Hohenberg and W. Kohn. Inhomogeneous Electron Gas. *Physical Review*, 136(3B):B864–B871, 1964.

[6] W. Kohn and L. J. Sham. Self-Consistent Equations Including Exchange and Correlation Effects. *Physical Review*, 140(4A):1133, 1965.

[7] John Lindl. Development of the indirect-drive approach to inertial confinement fusion and the target physics basis for ignition and gain. *Physics of Plasmas*, 2(11):3933–4024, 1995.

[8] R. S. Craxton, K. S. Anderson, T. R. Boehly, V. N. Goncharov, D. R. Harding, J. P. Knauer, R. L. McCrory, P. W. McKenty, D. D. Meyerhofer, J. F. Myatt, A. J. Schmitt, J. D. Sethian, R. W. Short, S. Skupsky, W. Theobald, W. L. Kruer, K. Tanaka, R. Betti, T. J.B. Collins, J. A. Delettrez, S. X. Hu, J. A. Marozas, A. V. Maximov, D. T. Michel, P. B. Radha, S. P. Regan, T. C. Sangster, W. Seka, A. A. Solodov, J. M. Soures, C. Stoeckl, and J. D. Zuegel. Direct-drive inertial confinement fusion: A review. *Physics of Plasmas*, 22(11):110501, 2015.

[9] R. Betti and O. A. Hurricane. Inertial-confinement fusion with lasers. *Nature Physics*, 12(5):435–448, 2016.

[10] S. X. Hu, L. A. Collins, T. R. Boehly, Y. H. Ding, P. B. Radha, V. N. Goncharov, V. V. Karasiev, G. W. Collins, S. P. Regan, and E. M. Campbell. A review on ab initio studies of static, transport, and optical properties of polystyrene under extreme conditions for inertial confinement fusion applications. *Physics of Plasmas*, 25(5):056306, 2018.

[11] A. K. Verma, P. Modak, R. S. Rao, and B. K. Godwal. Role of ab initio calculations in high pressure-high temperature studies and material properties. *Journal of Physics and Chemistry of Solids*, 67:2222–2229, 2006.

[12] Lorin X. Benedict, Kevin P. Driver, Sebastien Hamel, Burkhard Militzer, Tingting Qi, Alfredo A. Correa, A. Saul, and Eric Schwegler. Multiphase equation of state for carbon addressing high pressures and temperatures. *Physical Review B - Condensed Matter and Materials Physics*, 89(22):224109, 2014.

[13] Nadine Nettelmann, Bastian Holst, André Kietzmann, Martin French, Ronald Redmer, and David Blaschke. Ab initio Equation of State data

for hydrogen, helium, and water and the internal structure of Jupiter. *The Astrophysical Journal*, 683(2):1217–1228, dec 2008.

[14] Winfried Lorenzen, Bastian Holst, and Ronald Redmer. Demixing of Hydrogen and Helium at Megabar Pressures. *Physical Review Letters*, 102(11):115701, 2009.

[15] Martin French, Andreas Becker, Winfried Lorenzen, Nadine Nettelmann, Mandy Bethkenhagen, Johannes Wicht, and Ronald Redmer. Ab Initio Simulations for Material Properties Along the Jupiter Adiabat. *The Astrophysical Journal Supplement Series*, 202(5):1–11, 2012.

[16] L. Caillabet, S. Mazevet, and P. Loubeyre. Multiphase equation of state of hydrogen from ab initio calculations in the range 0.2 to 5 g/cc up to 10 eV. *Physical Review B - Condensed Matter and Materials Physics*, 83(9):094101, 2011.

[17] M. D. Knudson, M. P. Desjarlais, R. W. Lemke, T. R. Mattsson, M. French, N. Nettelmann, and R. Redmer. Probing the Interiors of the Ice Giants: Shock Compression of Water to 700 GPa and 3.8 g/cm^{3}. *Physical Review Letters*, 108(9):091102, feb 2012.

[18] D. S. Rackstraw, S. M. Vinko, O. Ciricosta, B. I. Cho, K. Engelhorn, H.-K. Chung, C. R. D. Brown, T. Burian, J. Chalupský, R. W. Falcone, C. Graves, V. Hájková, A. Higginbotham, L. Juha, J. Krzywinski, H. J. Lee, M. Messerschmidt, C. Murphy, Y. Ping, A. Scherz, W. Schlotter, S. Toleikis, J. J. Turner, L. Vysin, T. Wang, B. Wu, U. Zastrau, D. Zhu, B. Nagler, R. W. Lee, P. A. Heimann, and J.S. Wark. Opacity effects in a solid-density aluminium plasma created by photo-excitation with an X-ray laser. *High Energy Density Physics*, 11:59–69, jun 2014.

[19] D.S. Rackstraw, O. Ciricosta, S.M. Vinko, B. Barbrel, T. Burian, J. Chalupský, B.I. Cho, H.-K. Chung, G.L. Dakovski, K. Engelhorn, V. Hájková, P. Heimann, M. Holmes, L. Juha, J. Krzywinski, R.W. Lee, S. Toleikis, J.J. Turner, U. Zastrau, and J.S. Wark. Saturable Absorption of an X-Ray Free-Electron-Laser Heated Solid-Density Aluminum Plasma. *Physical Review Letters*, 114(1):015003, jan 2015.

[20] S. M. Vinko, O. Ciricosta, B. I. Cho, K. Engelhorn, H.-K. Chung, C. R. D. Brown, T. Burian, J. Chalupský, R. W. Falcone, C. Graves, V. Hájková, A. Higginbotham, L. Juha, J. Krzywinski, H. J. Lee, M. Messerschmidt, C. D. Murphy, Y. Ping, A. Scherz, W. Schlotter, S. Toleikis, J. J. Turner, L. Vysin, T. Wang, B. Wu, U. Zastrau, D. Zhu, R. W. Lee, P. A. Heimann, B. Nagler, and J. S. Wark. Creation and diagnosis of a solid-density plasma with an X-ray free-electron laser. *Nature*, 482:59–62, feb 2012.

[21] O. Ciricosta, S. M. Vinko, B. Barbrel, D. S. Rackstraw, T. R. Preston, T. Burian, J. Chalupský, B. I. Cho, H. K. Chung, G. L. Dakovski, K. Engelhorn, V. Hájková, P. Heimann, M. Holmes, L. Juha, J. Krzywinski, R. W. Lee, S. Toleikis, J. J. Turner, U. Zastrau, and J. S. Wark. Measurements of continuum lowering in solid-density plasmas created from elements and compounds. *Nature Communications*, 7:11713, 2016.

[22] T. R. Preston, S. M. Vinko, O. Ciricosta, P. Hollebon, H. K. Chung, G. L. Dakovski, J. Krzywinski, M. Minitti, T. Burian, J. Chalupský, V. Hájková, L. Juha, V. Vozda, U. Zastrau, R. W. Lee, and J. S. Wark. Measurements of the K -Shell Opacity of a Solid-Density Magnesium Plasma Heated by an X-Ray Free-Electron Laser. *Physical Review Letters*, 119(8):085001, 2017.

[23] D. Kraus, D. A. Chapman, A. L. Kritcher, R. A. Baggott, B. Bachmann, G. W. Collins, S. H. Glenzer, J. A. Hawreliak, D. H. Kalantar, O. L. Landen, T. Ma, S. Le Pape, J. Nilsen, D. C. Swift, P. Neumayer, R. W. Falcone, D. O. Gericke, and T. Döppner. X-ray scattering measurements on imploding CH spheres at the National Ignition Facility. *Physical Review E - Statistical, Nonlinear, and Soft Matter Physics*, 94(1):011202, 2016.

[24] T. G. White, J. Vorberger, C. R. D. Brown, B. J. B. Crowley, P. Davis, S. H. Glenzer, J. W. O. Harris, D. C. Hochhaus, S. Le Pape, T. Ma, C. D. Murphy, P. Neumayer, L. K. Pattison, S. Richardson, D. O. Gericke, and G. Gregori. Observation of inhibited electron-ion coupling in strongly heated graphite. *Scientific Reports*, 2:889, 2012.

[25] G. Gregori, S. H. Glenzer, K. B. Fournier, K. M. Campbell, E. L. Dewald, O. S. Jones, J. H. Hammer, S. B. Hansen, R. J. Wallace, and O. L. Landen. X-Ray Scattering Measurements of Radiative Heating and Cooling Dynamics. *Physical Review Letters*, 101(4):045003, 2008.

[26] A. B. Zylstra, J. A. Frenje, P. E. Grabowski, C. K. Li, G. W. Collins, P. Fitzsimmons, S. Glenzer, F. Graziani, S. B. Hansen, S. X. Hu, M. Gatu Johnson, P. Keiter, H. Reynolds, J. R. Rygg, F. H. Séguin, and R. D. Petrasso. Measurement of Charged-Particle Stopping in Warm Dense Plasma. *Physical Review Letters*, 114(21):215002, 2015.

[27] N. David Mermin. Thermal Properties of the Inhomogeneous Electron Gas. *Physical Review*, 137(5A):1441–1443, 1965.

[28] M. Petersilka, U. J. Gossmann, and E. K. U. Gross. Excitation Energies from Time-Dependent Density-Functional Theory. *Physical Review Letters*, 76(8):1212–1215, 1996.

[29] François Perrot and M. W. C. Dharma-wardana. Exchange and correlation potentials for electron-ion systems at finite temperatures. *Physical Review A - Atomic, Molecular, and Optical Physics*, 30(5):2619–2626, 1984.

[30] Travis Sjostrom and Jérôme Daligault. Gradient corrections to the exchange-correlation free energy. *Physical Review B - Condensed Matter and Materials Physics*, 90(15):155109, 2014.

[31] M. W. C. Dharma-wardana and Roger Taylor. Exchange and correlation potentials for finite temperature quantum calculations at intermediate degeneracies. *Journal of Physics C: Solid State Physics*, 14:629–646, 1981.

[32] M. Dharma-wardana. Current Issues in Finite-T Density-Functional Theory and Warm-Correlated Matter †. *Computation*, 4(2):16, 2016.

[33] A. K. Gupta and K. S. Singwi. Gradient corrections to the exchange-correlation energy of electrons at metal surfaces. *Physical Review B - Condensed Matter and Materials Physics*, 15(4):1801–1810, 1977.

[34] T. G. White, S. Richardson, B. J. B. Crowley, L. K. Pattison, J. W. O. Harris, and G. Gregori. Orbital-Free Density-Functional Theory Dimulations of the Dynamic Structure Factor of Warm Dense Aluminum. *Physical Review Letters*, 111(17):175002, 2013.

[35] Yael Cytter, Eran Rabani, Daniel Neuhauser, and Roi Baer. Stochastic Density Functional Theory at Finite Temperatures. *Physical Review B - Condensed Matter and Materials Physics*, 97(11):115207, 2018.

[36] F. Lambert, J. Clérouin, S. Mazevet, and D. Gilles. Properties of Hot Dense Plasmas by Orbital-Free Molecular Dynamics. *Contributions to Plasma Physics*, 47(4-5):272–280, 2007.

[37] J.-F. Danel, L. Kazandjian, and G. Zérah. Equation of state of dense plasmas by ab initio simulations: Bridging the gap between quantum molecular dynamics and orbital-free molecular dynamics at high temperature. *Physics of Plasmas*, 19(12):122712, 2012.

[38] F. Lambert, J. Clérouin, and S. Mazevet. Structural and dynamical properties of hot dense matter by a Thomas-Fermi-Dirac molecular dynamics. *Europhysics Letters*, 75(5):681–687, 2006.

[39] John P. Perdew and Yue Wang. Accurate and Simple Analytic Representation of the Electron-Gas Correlation Energy. *Physical Review B - Condensed Matter and Materials Physics*, 45(23):13244–13249, 1992.

[40] John P. Perdew, Kieron Burke, and Matthias Ernzerhof. Generalized Gradient Approximation Made Simple. *Physical Review Letters*, 77(18):3865–3868, oct 1996.

[41] Richard M. Martin. *Electronic Structure Basic Theory and Practical Methods*. Cambridge University Press, 2010.

[42] François Perrot and M. W. C. Dharma-wardana. Spin-polarized electron liquid at arbitrary temperatures: Exchange-correlation energies, electron-distribution functions, and the static response functions. *Physical Review B - Condensed Matter and Materials Physics*, 62(24):16536–16548, 2000.

[43] Gérald Faussurier, Pier Luigi Silvestrelli, and Christophe Blancard. Finite-temperature exchange-correlation functional in an ab initio molecular dynamics code. *High Energy Density Physics*, 5:74–79, 2009.

[44] John J. Rehr and Joshua J. Kas. Exchange and correlation in finite-temperature TDDFT. *European Physical Journal B*, 91:153, 2018.

[45] Valentin V. Karasiev, Lázaro Calderín, and S. B. Trickey. Importance of finite-temperature exchange correlation for warm dense matter calculations. *Physical Review E - Statistical, Nonlinear, and Soft Matter Physics*, 93(6):063207, 2016.

[46] S. Pittalis, C. R. Proetto, A. Floris, A. Sanna, C. Bersier, K. Burke, and E. K. U. Gross. Exact Conditions in Finite-Temperature Density-Functional Theory. *Physical Review Letters*, 107(16):163001, 2011.

[47] Abinit Website. http://www.abinit.org.

[48] N. A. W. Holzwarth, A. R. Tackett, and G. E. Matthews. A Projector Augmented Wave (PAW) code for electronic structure calculations, Part I: atompaw for generating atom-centered functions. *Computer Physics Communications*, 135:329–347, apr 2001.

[49] Q. Y. van den Berg, E. V. Fernandez-Tello, T. Burian, J. Chalupský, H. K. Chung, O. Ciricosta, G. L. Dakovski, V. Hájková, P. Hollebon, L. Juha, J. Krzywinski, R. W. Lee, M. P. Minitti, T. R. Preston, A. G. De La Varga, V. Vozda, U. Zastrau, J. S. Wark, P. Velarde, and S. M. Vinko. Clocking Femtosecond Collisional Dynamics via Resonant X-Ray Spectroscopy. *Physical Review Letters*, 120(5):055002, 2018.

[50] P. Mabey, S. Richardson, T. G. White, L. B. Fletcher, S. H. Glenzer, N. J. Hartley, J. Vorberger, D. O. Gericke, and G. Gregori. A strong dif-

fusive ion mode in dense ionized matter predicted by Langevin dynamics. *Nature Communications*, 8:14125, 2017.

[51] A. D. Baczewski, L. Shulenburger, M. P. Desjarlais, S. B. Hansen, and R. J. Magyar. X-ray Thomson Scattering in Warm Dense Matter without the Chihara Decomposition. *Physical Review Letters*, 116(11):115004, 2016.

[52] Peter E Blöchl, Johannes Kästner, and Clemens J Först. Electronic Structure Methods: Augmented Waves, Pseudopotentials and The Projector Augmented Wave Method. In *Handbook of Materials Modeling*, pages 93–119. jul 2005.

[53] P. E. Blöchl. Projector augmented-wave method. *Physical Review B - Condensed Matter and Materials Physics*, 50(24):17953–17979, 1994.

[54] Giovanni Onida, Lucia Reining, and Angel Rubio. Electronic excitations: Density-functional versus many-body Green's-function approaches. *Reviews of Modern Physics*, 74(2):601–659, 2002.

[55] R. D. Cowan. *The Theory of Atomic Structure and Spectra*. University of California Press, 1981.

[56] S. M. Vinko, O Ciricosta, and J. S. Wark. Density functional theory calculations of continuum lowering in strongly coupled plasmas. *Nature Communications*, 5:3533, jan 2014.

[57] X. Gonze, B. Amadon, P.-M. Anglade, J.-M. Beuken, F. Bottin, P. Boulanger, F. Bruneval, D. Caliste, R. Caracas, M. Côté, T. Deutsch, L. Genovese, Ph. Ghosez, M. Giantomassi, S. Goedecker, D. R. Hamann, P. Hermet, F. Jollet, G. Jomard, S. Leroux, M. Mancini, S. Mazevet, M. J. T. Oliveira, G. Onida, Y. Pouillon, T. Rangel, G.-M. Rignanese,

D. Sangalli, R. Shaltaf, M. Torrent, M. J. Verstraete, G. Zerah, and J. W. Zwanziger. ABINIT: First-principles approach to material and nanosystem properties. *Computer Physics Communications*, 180:2582–2615, dec 2009.

[58] Hendrik J. Monkhorst and James D. Pack. Special points for Brillonin-zone integrations. *Physical Review B - Condensed Matter and Materials Physics*, 13(12):5188–5192, 1976.

[59] Ryogo Kubo. Statistical-Mechanical Theory of Irreversible Processes. I. General Theory and Simple Applications to Magnetic and Conduction Problems, 1957.

[60] Carlos A. Iglesias and Philip A. Sterne. Fluctuations and the ionization potential in dense plasmas. *High Energy Density Physics*, 9:103–107, 2013.

[61] Setsuo Ichimaru. Theory of Fluctuations in a Plasma. *Annals of Physics*, 20:78–118, 1962.

[62] B. J. B. Crowley. Density fluctuations and temperature relaxation in multicomponent plasmas. *arXiv:1508.06530 [physics.plasm-ph]*, 2015.

[63] J. E. Cross, P. Mabey, D. O. Gericke, and G. Gregori. Theory of density fluctuations in strongly radiative plasmas. *Physical Review E - Statistical, Nonlinear, and Soft Matter Physics*, 93(3):033201, 2016.

[64] Philippe Nozières and David Pines. Electron Interaction in Solids. General Formulation. *Physical Review*, 109(3):741–761, 1958.

[65] N.W. Ashcroft and N.D. Mermin. Solid State Physics. Cengage Learning, 2011.

[66] Y. T. Lee and R. M. More. An electron conductivity model for dense plasmas. *The Physics of Fluids*, 27(5):1273–1286, 1984.

[67] W.-D. Kraeft, D. Kremp, W. Ebeling, and G. Röpke. *Quantum Statistics of Charged Particle Systems*. Akademie-Verlag, Berlin, and Plenum Press, London/New York, 1986.

[68] D. Kremp, M. Schlanges, W.-D. Kraeft, and T. Bornath. *Quantum Statistics of Nonideal Plasmas*. Springer-Verlag, Berlin/Heidelberg, 2005.

[69] Davide Sangalli, J. A. Berger, Claudio Attaccalite, Myrta Grüning, and Pina Romaniello. Optical properties of periodic systems within the current-current response framework: Pitfalls and remedies. *Physical Review B - Condensed Matter and Materials Physics*, 95(15):155203, 2017.

[70] William Bernard and Herbert B. Callen. Irreversible Thermodynamics of Nonlinear Processes and Noise in Driven Systems. *Reviews of Modern Physics*, 31(4):1017–1044, 1959.

[71] Erich Runge and E. K. U. Gross. Density-Functional Theory for Time-Dependent Systems. *Physical Review Letters*, 52(12):997–1000, 1984.

[72] Robert van Leeuwen. Mapping from Densities to Potentials in Time-Dependent Density-Functional Theory. *Physical Review Letters*, 82(19):3863–3866, 1999.

[73] Maria Hellgren and Ulf Von Barth. Linear density response function within the time-dependent exact-exchange approximation. *Physical Review B - Condensed Matter and Materials Physics*, 78(11):115107, 2008.

[74] Jochen Heyd, Gustavo E. Scuseria, and Matthias Ernzerhof. Hybrid functionals based on a screened Coulomb potential. *The Journal of Chemical Physics*, 118(18):8207–8215, 2003.

[75] Jochen Heyd, Gustavo E. Scuseria, and Matthias Ernzerhof. Erratum: Hybrid functionals based on a screened Coulomb potential (Journal of Chemical Physics (2003) 118 (8207)). *The Journal of Chemical Physics*, 124(21):219906, 2006.

[76] John P. Perdew, Matthias Ernzerhof, and Kieron Burke. Rationale for mixing exact exchange with density functional approximations. *The Journal of Chemical Physics*, 105(22):9982–9985, 1996.

[77] M. P. Desjarlais, J. D. Kress, and L. A. Collins. Electrical conductivity for warm, dense aluminum plasmas and liquids. *Physical Review E - Statistical, Nonlinear, and Soft Matter Physics*, 66(2):025401, aug 2002.

[78] Uwe Brandt and Michael Moraweck. Rigorous results on the DC Kubo-Greenwood conductivity of disordered systems. *Journal of Physics C: Solid State Physics*, 15:5255–5268, 1982.

[79] Vojtěch Vlček, Nico De Koker, and Gerd Steinle-Neumann. Electrical and thermal conductivity of Al liquid at high pressures and temperatures from ab initio computations. *Physical Review B - Condensed Matter and Materials Physics*, 85(18):184201, 2012.

[80] B. B. L. Witte, P. Sperling, M. French, V. Recoules, S. H. Glenzer, and R. Redmer. Observations of non-linear plasmon damping in dense plasmas. *Physics of Plasmas*, 25(5):056901, 2018.

[81] Siegfried H. Glenzer and Ronald Redmer. X-ray Thomson scattering in high energy density plasmas. *Reviews of Modern Physics*, 81(4):1625–1663, 2009.

[82] David C. Langreth and John W. Wilkins. Theory of Spin Resonance in Dilute Magnetic Alloys. *Physical Review B - Condensed Matter and Materials Physics*, 6(9):3189–3227, 1972.

[83] Junzo Chihara. Difference in X-ray scattering between metallic and non-metallic liquids due to conduction electrons. *Journal of Physics F: Metal Physics*, 17:295–304, 1987.

[84] A. Höll, Th. Bornath, L. Cao, T. Döppner, S. Düsterer, E. Förster, C. Fortmann, S. H. Glenzer, G. Gregori, T. Laarmann, K. H. Meiwes-Broer, A. Przystawik, P. Radcliffe, R. Redmer, H. Reinholz, G. Röpke, R. Thiele, J. Tiggesbäumker, S. Toleikis, N. X. Truong, T. Tschentscher, I. Uschmann, and U. Zastrau. Thomson scattering from near-solid density plasmas using soft X-ray free electron lasers. *High Energy Density Physics*, 3:120–130, 2007.

[85] B. J. B. Crowley and G. Gregori. Quantum theory of Thomson scattering. *High Energy Density Physics*, 13:55–83, 2014.

[86] G. Röpke, H. Reinholz, C. Neißner, B. Omar, and a. Sengebusch. Bound State Formation and Optical Properties of Partially Ionized Dense Plasmas. *Contributions to Plasma Physics*, 45(5-6):414–423, 2005.

[87] M. W. C. Dharma-wardana. Static and dynamic conductivity of warm dense matter within a density-functional approach: Application to aluminum and gold. *Physical Review E - Statistical, Nonlinear, and Soft Matter Physics*, 73(3):036401, 2006.

[88] Marco Cazzaniga, Hans-Christian Weissker, Simo Huotari, Tuomas Pylkkänen, Paolo Salvestrini, Giulio Monaco, Giovanni Onida, and Lucia Reining. Dynamical response function in sodium and aluminum from time-dependent density-functional theory. *Physical Review B - Condensed Matter and Materials Physics*, 84(7):075109, 2011.

[89] K-U. Plagemann, P. Sperling, R. Thiele, M. P. Desjarlais, C. Fortmann, T. Döppner, H. J. Lee, S. H. Glenzer, and R. Redmer. Dynamic structure factor in warm dense beryllium. *New Journal of Physics*, 14(5):055020, 2012.

[90] Aurora Pribram-Jones, Paul E. Grabowski, and Kieron Burke. Thermal Density Functional Theory: Time-Dependent Linear Response and Approximate Functionals from the Fluctuation-Dissipation Theorem. *Physical Review Letters*, 116(23):233001, 2016.

[91] Ari Ojanperä, Ville Havu, Lauri Lehtovaara, and Martti Puska. Nonadiabatic Ehrenfest molecular dynamics within the projector augmented-wave method. *The Journal of Chemical Physics*, 136(144103), 2012.

[92] H. J. Lee, P. Neumayer, J. Castor, T. Döppner, R. W. Falcone, C. Fortmann, B. A. Hammel, A. L. Kritcher, O. L. Landen, R. W. Lee, D. D. Meyerhofer, D. H. Munro, R. Redmer, S. P. Regan, S. Weber, and S. H. Glenzer. X-ray Thomson-Scattering Measurements of Density and Temperature in Shock-Compressed Beryllium. *Physical Review Letters*, 102(11):115001, 2009.

[93] John C. Stewart and Kedar D. Pyatt Jr. Lowering of Ionization Potentials in Plasmas. *The Astrophysical Journal*, 144:1203–1211, 1966.

[94] G. Ecker and W. Kröll. Lowering of the Ionization Energy for a Plasma in Thermodynamic Equilibrium. *The Physics of Fluids*, 6(1):62–69, 1963.

[95] O. Ciricosta, S. M. Vinko, H.-K. Chung, C. Jackson, R. W. Lee, T. R. Preston, D. S. Rackstraw, and J. S. Wark. Detailed model for hot-dense aluminum plasmas generated by an x-ray free electron laser. *Physics of Plasmas*, 23(2):022707, 2016.

[96] K. Sturm. Electron energy loss in simple metals and semiconductors. *Advances In Physics*, 31(1):1–64, 1982.

[97] K. Sturm, E. Zaremba, and K. Nuroh. Core polarization and the dielectric response of simple metals. *Physical Review B - Condensed Matter and Materials Physics*, 42(11):6973–6992, 1990.

[98] D. Roth, B. Bruckner, M. V. Moro, S. Gruber, D. Goebl, J. I. Juaristi, M. Alducin, R. Steinberger, J. Duchoslav, D. Primetzhofer, and P. Bauer. Electronic Stopping of Slow Protons in Transition and Rare Earth Metals: Breakdown of the Free Electron Gas Concept. *Physical Review Letters*, 118(10):103401, 2017.

[99] Sam M. Vinko, Gianluca Gregori, Michael P. Desjarlais, Bob Nagler, Thomas J. Whitcher, Richard W. Lee, Patrick Audebert, and Justin S. Wark. Free-free opacity in warm dense aluminum. *High Energy Density Physics*, 5:124–131, 2009.

[100] Carlos A. Iglesias. XUV absorption by solid-density aluminum. *High Energy Density Physics*, 6:311–317, 2010.

[101] G. O. Williams, H.-K. Chung, S. M. Vinko, S. Künzel, A. B. Sardinha, Ph. Zeitoun, and M. Fajardo. Method of time resolved refractive index measurements of x-ray laser heated solids. *Physics of Plasmas*, 20(4):042701, 2013.

[102] B. Kettle, T. Dzelzainis, S. White, L. Li, B. Dromey, M. Zepf, C. L. S. Lewis, G. Williams, S. Künzel, M. Fajardo, H. Dacasa, Ph. Zeitoun, A. Rigby, G. Gregori, C. Spindloe, R. Heathcote, and D. Riley. Experimental measurements of the collisional absorption of XUV radiation in warm dense aluminium. *Physical Review E - Statistical, Nonlinear, and Soft Matter Physics*, 94(2):023203, 2016.

[103] N.R. Shaffer, N. G. Ferris, J. Colgan, D. P. Kilcrease, and C. E. Starrett. Free-free opacity in dense plasmas with an average atom model. *High Energy Density Physics*, 23:31–37, 2017.

[104] Gareth O. Williams, S. Künzel, S. Daboussi, B. Iwan, A. I. Gonzalez, W. Boutu, V. Hilbert, U. Zastrau, H. J. Lee, B. Nagler, E. Granados, E. Galtier, P. Heimann, B. Barbrel, G. Dovillaire, R. W. Lee, J. Dunn, V. Recoules, C. Blancard, P. Renaudin, A. G. De La Varga, P. Velarde, P. Audebert, H. Merdji, Ph. Zeitoun, and M. Fajardo. Tracking the ultrafast XUV optical properties of x-ray free-electron-laser heated matter with high-order harmonics. *Physical Review A*, 97(2):023414, 2018.

[105] H. A. Kramers. On the theory of X-ray absorption and of the continuous X-ray spectrum. *The London, Edinburgh, and Dublin Philosophical Magazine and Journal of Science*, 46(275):836–871, 1923.

[106] John Dawson and Carl Oberman. High-Frequency Conductivity and the Emission and Absorption Coefficients of a Fully Ionized Plasma. *The Physics of Fluids*, 5(5):517–524, 1962.

[107] Amiram Ron and Narkis Tzoar. Interaction of Electromagnetic Waves with Quantum and Classical Plasmas. *Physical Review*, 131(1):12–20, 1963.

[108] John F. Seely and Edward G. Harris. Heating of a Plasma by Multiphoton Inverse Bremsstrahlung. *Physical Review A - Atomic, Molecular, and Optical Physics*, 7(3):1064–1067, 1973.

[109] V. N. Tsytovich, R. Bingham, U. de Angelis, and A. Forlani. Relativistic corrections to inverse bremsstrahlung in the solar interior. *Physics Letters A*, 205:199–202, 1995.

[110] Hiroo Totsuji. Bremsstrahlung in high-density plasmas. *Physical Review A - Atomic, Molecular, and Optical Physics*, 32(5):3005–3010, 1985.

[111] G Bekefi. *Radiation Processes in Plasmas*. Wiley, 1966.

[112] R. Zimmermann, K. Kilimann, W. D. Kraeft, D. Kremp, and G. Röpke. Dynamical Screening and Self-Energy of Excitons in the Electron-Hole Plasma. *Physica Status Solidi (B)*, 90:175–187, 1978.

[113] G. Röpke, K. Kilimann, D. Kremp, W. D. Kraeft, and R. Zimmermann. The Influence of Dynamical Effects on the Two-Particle States (Excitons) in the Electron-Hole Plasma. *Physica Status Solidi (B)*, 88:K59–K63, 1978.

[114] S. Günter, L. Hitzschke, and G. Röpke. Hydrogen spectral lines with the inclusion of dense-plasma effects. *Physical Review A - Atomic, Molecular, and Optical Physics*, 44(10):6834–6844, 1991.

[115] J Seidel, S Arndt, and W. D. Kraeft. Energy spectrum of hydrogen atoms in dense plasmas. *Physical Review E - Statistical, Nonlinear, and Soft Matter Physics*, 52(5):5387–5400, 1995.

[116] Chengliang Lin, Gerd Röpke, Wolf-Dietrich Kraeft, and Heidi Reinholz. Ionization-potential depression and dynamical structure factor in dense

plasmas. *Physical Review E - Statistical, Nonlinear, and Soft Matter Physics*, 96(1):013202, 2017.

[117] J. J. Kas and J. J. Rehr. Finite Temperature Green's Function Approach for Excited State and Thermodynamic Properties of Cool to Warm Dense Matter. *Physical Review Letters*, 119(17):176403, 2017.

[118] Ronald Redmer, Gerd Röpke, Sandra Kuhlbrodt, and Heidi Reinholz. Hopping conductivity in dense hydrogen fluid. *Physical Review B - Condensed Matter and Materials Physics*, 63(23):233104, 2001.

[119] E. M. Gullikson, P. Denham, S. Mrowka, and J. H. Underwood. Absolute photoabsorption measurements of Mg, Al, and Si in the soft-x-ray region below the L_{2,3) edges. *Physical Review B - Condensed Matter and Materials Physics*, 49(23):16283–16289, 1994.

[120] H.-G. Birken, W. Jark, C. Kunz, and R. Wolf. Angular dependent photoelectric yield and optical constants of Al between 40 and 600 eV. *Nuclear Instruments and Methods in Physics Research*, 253:166–170, 1986.

[121] B. L. Henke, E. M. Gullikson, and J. C. Davis. X-Ray Interactions: Photoabsorption, Scattering, Transmission, and Reflection at E = 50-30,000 eV, Z = 1-92. *Atomic Data and Nuclear Data Tables*, 54(2):181–342, 1993.

[122] R. Keenan, C. L. S. Lewis, J. S. Wark, and E. Wolfrum. Measurements of the XUV transmission of aluminium with a soft x-ray laser. *Journal of Physics B: Atomic, Molecular and Optical Physics*, 35:L447–L451, 2002.

[123] CXRO Database. http://henke.lbl.gov/optical constants/.

[124] Fabio Frassetto, Cephise Cacho, Chris A. Froud, I.C. Edmund Turcu, Paolo Villoresi, Will A. Bryan, Emma Springate, and Luca Poletto.

Single-grating monochromator for extreme-ultraviolet ultrashort pulses. *Optics Express*, 19(20):19169–19181, 2011.

[125] Sergey V. Faleev, Mark van Schilfgaarde, Takao Kotani, François Léonard, and Michael P. Desjarlais. Finite-temperature quasiparticle self-consistent GW approximation. *Physical Review B - Condensed Matter and Materials Physics*, 74(3):033101, 2006.

[126] D. Semkat, D. Kremp, and M. Bonitz. Kadanoff-Baym equations with initial correlations. *Physical Review E - Statistical, Nonlinear, and Soft Matter Physics*, 59(2):1557–1562, 1999.

[127] S. Lebègue, B. Arnaud, M. Alouani, and P. E. Bloechl. Implementation of an all-electron GW approximation based on the projector augmented wave method without plasmon pole approximation: Application to Si, SiC, AlAs, InAs, NaH, and KH. *Physical Review B - Condensed Matter and Materials Physics*, 67(15):155208, 2003.

[128] Y. Pavlyukh. Padé resummation of many-body perturbation theories. *Scientific Reports*, 7(1):1–11, 2017.

[129] Marc Torrent, François Jollet, François Bottin, Gilles Zérah, and Xavier Gonze. Implementation of the projector augmented-wave method in the ABINIT code: Application to the study of iron under pressure. *Computational Materials Science*, 42:337–351, 2008.